Timing and spectral evolution of transient X-ray binaries

Master's Thesis of Matthias Kühnel
April 2011

FRIEDRICH-ALEXANDER
UNIVERSITÄT
ERLANGEN-NÜRNBERG

NATURWISSENSCHAFTLICHE
FAKULTÄT

ERLANGEN CENTRE
FOR ASTROPARTICLE
PHYSICS

DECLARATION

Hereby I declare that I wrote this Master's Thesis independently and that I have not used other resources than those quoted in this work.

ERKLÄRUNG

Hiermit erkläre ich, dass ich die Master-Thesis selbstständig angefertigt und keine Hilfsmittel außer den in der Arbeit angegebenen benutzt habe.

Bamberg, 08. April 2011 _____

(Matthias Kühnel)

Contents

Abstract

Transient X-ray binaries consist of a star and an object of high density, called a compact object. The compact objects studied in this thesis are neutron stars, which are the remnants of supernova explosions. Mass transfer from the companion star onto the neutron star's surface results in emission of X-rays, which are only observable by X-ray satellites. If the orbit of the neutron star is elliptical, mass transfer is only possible close to the periastron, where both stars are closest to each other. This means these systems are usually only observable once per orbit for a short time. That is why they are called transients.

The luminosity over time, called lightcurve, of a neutron star can show pulsations if the magnetic field strength is high. The pulse period corresponds to the rotation period of the neutron star. Due to orbital motion of the neutron star the observed pulse period is Doppler shifted. By analyzing the time dependency of the Doppler shift the orbital parameters of the binary can be obtained. In transient sources this determination is challenging since the binary is only visible during an outburst around its periastron. In addition, the angular momentum transfer by mass accretion onto the neutron changes the rotational period. In consequence, the observed pulse period evolution is a superposition of the orbital motion and the angular momentum transfer.

A detailed description of the formation and properties of neutron star X-ray binaries is given in Chapter 1. The X-ray detectors which observed the X-ray binaries discussed in this thesis and the handling of X-ray data is described in Chapter 2.

To disentangle the observed evolution of the pulse period into the two effects mentioned above, an accurate analysis method is needed. Such a method is the modelling of so-called pulse arrival times, i.e., the times measured when the pulses in an X-ray lightcurve are observed. The required algorithms to determine and analyze the arrival times of a given lightcurve were implemented within this thesis. The details about the physics and implementation of these algorithms is presented in Chapter 3.

The arrival times method was used to analyze data from the transient X-ray binary GRO J1008–57. This system underwent bright outbursts in 2005 and 2007. The orbital period and, therefore, the separation of observed outbursts is about 248 days (Coe et al., 2007). During this thesis it turned out that the orbital parameters given in the literature cannot describe the observed pulse arrival times. The implemented algorithms were used to successfully update these parameters as discussed in Chapter 4.

Mass accretion onto neutron stars is a complex physical process. By analyzing the spectra of neutron stars this process is studied and theoretical predictions can be checked. Of special interest are the so-called cyclotron resonant scattering features, also known as cyclotron lines. They allow for the only direct measurement of the magnetic field strength of neutron stars. The theory of these features is yet not fully understood. A cyclotron line at 88 keV is claimed for GRO J1008–57, which would imply that this neutron star has one of the highest magnetic field strengths known (Shrader et al., 1999). In Chapter 4, the spectra of the outbursts in 2005 and 2007 are analyzed on cyclotron lines. Evidence for an absorption line at 23 keV is found, which would lower the magnetic field strength of GRO J1008–57 if interpreted as cyclotron line.

Chapter 1
Physical Background

Stellar evolution is essential for understanding the nature and physical properties of transient X-ray binaries. In this chapter, in Section 1.1, a short outline of this topic is given. Inspired by Kippenhahn & Weigert (1990) the evolution of a star is described chronologically beginning with the birth and resulting in the formation of a neutron star. Accordingly, the following Section 1.2 treats X-ray binaries with focus on neutron stars as the compact object. Further details about this topic are given by Frank et al. (1992).

1.1 Stellar Evolution

The evolution of a star commences when an interstellar gas cloud begins to collapse under self-gravity due to a local density fluctuation inside itself. The density and temperature of the core increase until finally hydrogen burning becomes possible: the collapsed cloud has been turned into an object, within whose core energy is produced by nuclear reactions. The surface of the object, which has a certain temperature due to the collapse itself and is heated by the nuclear reactions, emits black body radiation. The object is a *star* now. If the collapse and the radiation pressure resulting from hydrogen core burning are in hydrostatic equilibrium, the star is stable and called a *main sequence star*.

1.1.1 Main Sequence

On the *main sequence*, where stars spent most of their lifetime, they are stable and hydrogen burning takes place in their core. Thereby the net reaction is the fusion of hydrogen atoms to helium:

$$4\mathrm{p} \rightarrow {}^{4}\mathrm{He} + 2\mathrm{e}^{+} + 2\nu_{\mathrm{e}} + \gamma \tag{1.1}$$

The detailed reaction is possbile in basically two different series:

- *proton-proton chain* (*pp* chain)
  Starting at the fusion of two protons to a deuterium nucleus via the weak interaction, a further fusion with another proton leads to ^{3}He:

  $$2\mathrm{p} \xrightarrow{\beta^{+}} {}^{2}\mathrm{H} \xrightarrow{+\mathrm{p}} {}^{3}\mathrm{He} \tag{1.2}$$

  Secondary products, as for example neutrinos, are not shown for clarity. Further on, there are three possible steps to end up with ^{4}He, which are not discussed here in any details. The energy production rate of the pp chain is restricted to the probability of the involved beta decay during the fusion of two protons.
- *CNO cycle*
  This series requires certain isotopes of carbon, nitrogen and oxygen. They are used as

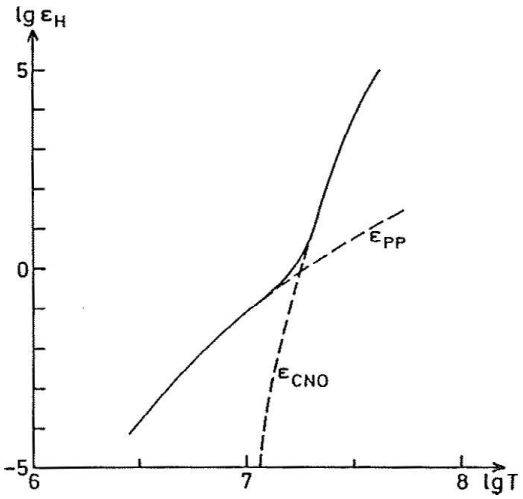

Figure 1.1: Temperature dependence of the pp chain and the CNO cycle (Kippenhahn & Weigert, 1990, Fig. 18.8). The energy production rate of the CNO cycle ϵ_{CNO} is much steeper than of the pp chain ϵ_{pp}, leading to a higher efficiency for temperatures above $T \approx 3 \times 10^7\,\mathrm{K}$.

catalysts to fuse hydrogen to helium, that means they come out unchanged. The main reactions are:

$$^{12}\mathrm{C} \xrightarrow{+\mathrm{p}} {}^{13}\mathrm{N} \xrightarrow{\beta^+} {}^{13}\mathrm{C} \xrightarrow{+\mathrm{p}} {}^{14}\mathrm{N} \xrightarrow{+\mathrm{p}} {}^{15}\mathrm{O} \xrightarrow{\beta^+} {}^{15}\mathrm{N} \xrightarrow{+\mathrm{p}} {}^{12}\mathrm{C} + {}^{4}\mathrm{He} \tag{1.3}$$

As before, secondary products as well as another, less probable connected cycle using ^{16}O are not included. The energy production rate of the CNO cycle is restricted to the slowest involved reaction, which is $^{14}\mathrm{N} + \mathrm{p}$ due to the high Coulomb barrier of nitrogen. However, the reaction $^{15}\mathrm{N} + \mathrm{p}$ is much faster because of a resonance, which is caused by the completely filled energy shells of the products ^{12}C and ^{4}He. Although the above reaction series looks complicated, the net reaction is the same as for the pp chain and given by Equation 1.1.

Comparing the energy production rates of the pp chain and the CNO cycle leads to an important result: hydrogen is more rapdily exhausted in massive stars with high temperatures and densities in their core. This behavior is based on the energy dependence of the physical effects. While the probability to tunnel scales with temperature, the beta decay rate, which is basic for the pp chain, is nearly independent of the temperature. Hence the CNO cycle is much more effective for core temperatures above $3 \times 10^7\,\mathrm{K}$ as shown in Figure 1.1.

1.1.2 Higher Burning Stages

If the nuclear fuel in the core of a star is exhausted, the star is no longer on the main sequence. The radiation pressure, which counters the gravitation, can no longer be maintained. Accordingly, the star collapses and the temperature and density increase further. If temperature and pressure reach certain critical values, the next burning stage will ignite. In that case the products of the former main reaction fuse to higher elements and the released energy stabilizes the star again. In addition further burning areas exist above the core, where the temperature is high enough to fuse lighter elements. Such phases are called *shell burning*, which also leads to a higher radiation pressure in the outer layers of the star. Therefore the star expands and is in the so-called *red giant phase*.

There are several subsequent burning stages during the lifetime of a star, which are summarized in Table 1.1. Due to the exhausting nuclear fuel the core of the star contracts at the end of each stage. The temperature increases and so do the reaction rates of the core and the shell burning. The lifetimes of the different burning stages decrease consequently. One should note that depending on the initial mass of the star, the necessary conditions to ignite the next burning stage might not be fulfilled.

Table 1.1: Nuclear burning stages, core density ρ_c, core temperature T_c and lifetime τ for stars with a mass of $20\,M_\odot$ (Thielemann et al., 2011).

Fuel	Product	ρ_c ($g\,cm^{-3}$)	T_c (10^9 K)	τ (yr)
H	He	5.6	0.04	1.0×10^7
He	C, O	9.4×10^2	0.19	9.5×10^5
C	Ne, Mg	2.7×10^5	0.81	300
Ne	O, Mg	4.0×10^6	1.70	0.38
O	Si	6.0×10^6	2.10	0.50
Si	Fe	4.9×10^7	3.70	0.006

The last nuclear burning stage with a net energy generation is Silicon burning. Its main product is iron, the nucleus with the highest binding energy.[1] Further fusion would result in an energy consumption instead of energy production needed to stabilize the core. Finally, the star collapses, when Silicon is exhausted in the core.

1.1.3 Neutron Star Formation

If the nuclear fuel in the core of a star is exhausted, no further energy, which counters the gravitation, is generated. In consequence, the core will collapse. The further evolution and the star's remnant, a *compact object*, depends strongly on the initial mass of the star.

For stars with an initial mass smaller than $8\,M_\odot$ the temperature and density in the core are too low to ignite carbon burning (Verbunt & van den Heuvel, 1995). At this stage the star basically consists of carbon and oxygen in its core and hydrogen and helium in the outer layers. When the core contracts, the released gravitational energy ejects the outer layers into space. The density inside the remaining core increases until the electrons, which can be described as a Fermi gas, become degenerate. The resulting electron pressure is able to stabilize the dying star, which is now called a *white dwarf*. Due to its high surface temperature in the order of 10^4 K the white dwarf emits black body radiation with a maximum in the UV and therefore appears white in the visible light. The radiation illuminates the ejected layers, which become visible as emission nebulae and are, missleadingly, called *planetary nebula*. The mass limit mentioned above depends, however, on the applied complex model of stellar evolution. Furthermore a star could evolve into a He- or Ne/Mg-white dwarf. Basically, the remaining mass has to be below than the *Chandrasekhar limit* of about $1.4\,M_\odot$ (Chandrasekhar, 1931). Above this limit the electron pressure is no longer able to stabilize the star.

If the star was massive enough to allow for higher burning stages up to silicon burning, the iron core collapses if its mass exceeds the Chandrasekhar limit. At this phase the internal structure of the star is onion-like and consists of different burning shells around the core (compare Figure 1.2). During the collapse of the core the density and temperature increase by severals orders of magnitude within fractions of a second. The Fermi energy of the electrons increases to the range of nuclear energies. This induces electron capture by the nuclei (Equation 1.4), which is in equlibrium with the β^--decay (Equation 1.5), which takes place if the nuclei become too rich on neutrons:

$$e^- + (N, Z) \rightarrow (N + 1, Z - 1) + \nu_e \quad (1.4)$$

$$(N, Z) \rightarrow (N - 1, Z + 1) + e^- + \bar{\nu}_e \quad (1.5)$$

[1] Note that ^{63}Ni has a higher binding energy than ^{56}Fe, however, ^{63}Ni is not commonly reached in stellar fusion cycles (Fewell, 1995).

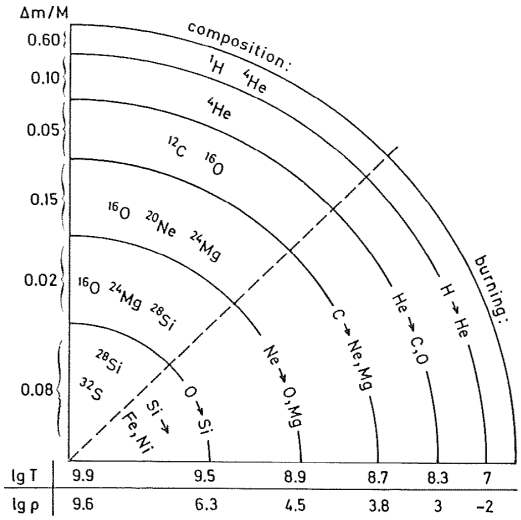

Figure 1.2: Onion-like structure of an evolved star after silicon burning (Kippenhahn & Weigert, 1990, Fig. 33.1). Regions of shell burning are shown as well as the composition of elements inside the star, both in units of mass fraction.

However, the proceeding collapse even increases the Fermi energy of the electrons further. Once it exceeds the energy of the released electron of the β^--decay, this process gets Pauli blocked, i.e., the electron capture is favored and most of the protons inside the core are converted into neutrons. At this point the density of the collapsing core reaches nuclear values in the order of $10^{15}\,\mathrm{g\,cm^{-3}}$, which leaves an almost incompressible neutron core stabilized by the pressure of degenerate neutrons. At its surface the infalling matter is reflected and a shock wave in outwards direction is formed. The density in the shock front is high enough to absorb the neutrinos produced by electron capture, which powers the shock which finally disrupts the star (Wilson, 1985). The explosion is observed as a supernova of type II with a total energy output in the order of $10^{53}\,\mathrm{erg\,s^{-1}}$, mostly in form of neutrinos. The detailed supernova mechanism, however, is subject of actual research, since the role of multi-dimensional effects and magnetic fields is still poorly understood (Janka et al., 2007, and references therein). The remaining object, which is stabilized by the degenerate neutrons, is called a *neutron star*. Its mass ranges from 0.9 to $2.6\,\mathrm{M_\odot}$ (see also Strobel & Weigel, 2001; Srinivasan, 2002) and depends on the progenitor mass and on accretion during the collapse. The outer layers of the progenitor star, which constituted most of its total mass, were ejected into the interstellar medium.

The rotation periods of a neutron star range from several minutes down to milliseconds. This range is the consequence of conservation of angular momentum during the supernova explosion of the progenitor. If the core radius and angular velocity right before the collapse are R_c and ω_c, respectively, the angular velocity ω of the resulting neutron star is given by

$$\frac{\mathrm{d}}{\mathrm{d}t}R_\mathrm{c}^2\omega_\mathrm{c} = 0 \quad \Rightarrow \quad \omega = \omega_\mathrm{c}\frac{R_\mathrm{c}^2}{R^2} \tag{1.6}$$

where R is the radius of the neutron star. Because $R \ll R_\mathrm{c}$ the neutron star is rotating much faster than its progenitor.
The magnetic field strength B_c of the collapsing core is enhanced as well. Here the conservation of the magnetic flux leads to

$$\frac{\mathrm{d}}{\mathrm{d}t}B_\mathrm{c}R_\mathrm{c}^2 = 0 \quad \Rightarrow \quad B = B_\mathrm{c}\frac{R_\mathrm{c}^2}{R^2} \tag{1.7}$$

where B is the magnetic field strength of the neutron star. The strengths of magnetic fields of neutron stars are in the order of $10^{12}\,G$.

If the initial mass of the star is above $40\,\mathrm{M_\odot}$ (Verbunt & van den Heuvel, 1995) the mass of the remaining neutron star extends the so-called *Tolman-Oppenheimer-Volkoff limit* and the neutron pressure is no longer able to stabilize the neutron matter. The exact

mass limit depends on the internal structure and the equation of state of the neutron star, which are still unknown, since they cannot be observed directly. Modern models predict a maximum mass of about $3\,M_\odot$ (Bombaci, 1996). It is assumed in general that no further mechanism exists, which would be able to prevent the collapse of a more massive object: the matter collapses to a point of infinite density, a *black hole*. Gaining information from this object is not possible, since the escape velocity is infinite in its center. The effects of black holes, however, are still observable, e.g., when they appear as the compact object in X-ray binaries.

1.2 X-ray binaries

During the collapse of an interstellar gas cloud not only one star is born (see Section 1.1). In fact such clouds can be several lightyears across, leading to a cosmic star forming site. Therefore it is not unlikely that two stars are formed nearby. Due to gravity the newborn stars might be bound together and orbit around a common center of mass. In *binary* systems the members evolve nearly independently. In fact about half of the visible stars on the sky are binaries (Abt, 1983). They can be identified as such for instance using the following methods (see Hilditch, 2001):

- in *visual binaries* the components can be clearly distinguished with a telescope. This, however, is only possible if the separation of both stars is larger than the angular resolution of the used instrument. The smallest angular separation of the stars which can be resolved today is about 0.2 arcsec.
- a binary can also be identified indirectly through spectral features. In these *spectroscopic binaries* the Doppler shift of the orbital motion causes a periodic modulation of characteristic absorption lines. The detection limit here is limited by the ability of the spectrometer to detect the modulation of the spectrum.
- in a few cases the orbital plane of a binary is perpendicular to the tangential plane of the sky and the *lightcurve*, the luminosity over time, of the system shows dips caused by the eclipse of one component by the other. The detection of this *eclipsing binaries* depend on the timing ability and the noise level of the detector.

If the initial mass of one component of a binary is much larger than of the other one, the nuclear full is exhausted earlier in the less massive star due to the higher energy production rate (see Section 1.1.1). Thus it happens that the heavier component either becomes a white dwarf or undergoes a supernova explosion, leaving a neutron star or black hole, while the companion star of the remaining compact object is still on the main sequence.

Because the compact objects in the binaries analyzed in this thesis are neutron stars, white dwarfs and black holes binaries will not be discussed further.

If, for some reason, mass is transfered from the optical companion onto the neutron star, X-rays are emitted with luminosities L_x in the order of $10^{37}\,\mathrm{erg\,s^{-1}}$. This mechanism is called *mass accretion* and was suggested by Zel'dovich & Guseynov (1966) to explain the observations of extrasolar X-ray sources. The first source was found in 1962 by rocket experiments and was named Sco X-1 (Giacconi et al., 1962) after its location in the scorpius constellation. X-ray emission by mass accretion is based on the released gravitational energy (Frank et al., 1992): a test particle m, which moves from infinity to the surface of the compact object, gains the energy

$$\Delta E = \frac{GMm}{R} \tag{1.8}$$

where G is the gravitional constant and M and R are the mass and radius of the compact object. In case of a neutron star with $M = 1\,\mathrm{M}_\odot$ and $R = 10\,\mathrm{km}$ and assuming that the energy is completely converted into radiation, this yields $\Delta E/m = 1.3 \times 10^{20}\,\mathrm{erg\,g^{-1}}$. To reach the measured luminosity a mass accretion rate of $\dot{M} = L_\mathrm{x} m/E\,t = 1.2 \times 10^{-9}\,\mathrm{M}_\odot$ yr^{-1} is required.

1.2.1 Accretion mechanisms

The mass transfer from the companion onto the neutron star is a complex physical process whose details are still not fully understood yet. Besides plasma physics, concepts from general relativity, electrodynamics and quantum physics play a role due to the steep gravitational potential and strong magnetic fields of neutron stars. Generally, accretion is only possible, however, if material gets unbound from the companion and moves into the area where it becomes gravitationally bound to the compact object. After loss of its angular momentum the matter is finally accreted. The three main accretion scenarios are (see also Frank et al., 1992, for details):

1. If one of the stars expands or the binary separation decreases, matter from the atmosphere of the companion can move into the gravitational potential of the compact object. This is called *Roche lobe overflow*.
2. In *wind accretion* the compact object accretes a fraction of the dense stellar wind of its companion, which is usually a hot and giant star of several solar radii.
3. Due to an elliptical orbit the compact object passes the circumstellar disc of a fast rotating star. This *transient-* or *Be-mechanism* leads to regular outburst in X-rays.

The different mechanisms are discussed in more detail in the following.

Roche Lobe Overflow

In order to describe the accretion flow from the outer layers of the companion onto the compact object, the gravitational potential of the binary has to be known. The gravitational forces on a test particle located at $\vec{r}$ depend on the time dependent positions $\vec{r}_1(t)$ and $\vec{r}_2(t)$ of both stars. If one assumes that the test particle mass m is negligible compared to the stellar masses M_1 and M_2 and that the stars move on circular orbits, the effective potential is given by

$$\Phi(\vec{r}) = -\frac{M_1 G}{|\vec{r} - \vec{r}_1|} - \frac{M_2 G}{|\vec{r} - \vec{r}_2|} - \frac{1}{2}(\vec{\Omega} \times \vec{r})^2 \tag{1.9}$$

This so-called *Roche potential* is expressed in the co-rotating frame of reference, where the position vectors of the stars $\vec{r}_1$ and $\vec{r}_2$ as well as the angular momentum vector $\vec{\Omega}$ are fixed. The first two terms of the potential are the individual gravitational potentials of the orbiting stars, while the last one is the centrifugal force. The volume, wherein the test mass m is gravitationally bound to one of the components, i.e., the according gravitional term dominates the potential, is called *Roche lobe* or *critical potential*. The equipotential surfaces of $\Phi(\vec{r})$ shown in Figure 1.3 reveal five points, where the different forces counterbalance: between both stars the gravitational forces vanish at the first Lagrange point L_1 (with a small contribution of the centrifugal force). The potential at this point marks the critical potential, which defines the equipotential surface of the Roche lobe. The potential $\Phi(\vec{r})$ is higher at the Lagrange points L_2 and L_3 than at L_1. Here the centrifugal force is equal to the summed up gravitation of the components of the binary. At the remaining Lagrange points L_4 and L_5 the test particle is gravitational affected by an effective mass, which results of the sum of both stars. The centrifugal force

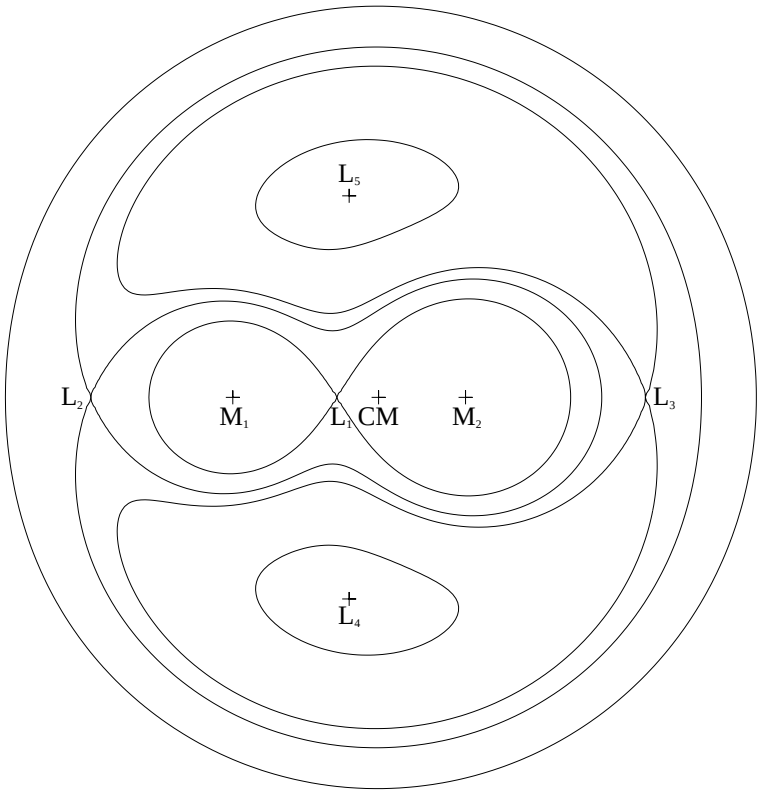

Figure 1.3: The equipotential surfaces of the Roche potential as generated by a mass ratio $q = M_1/M_2 = 0.6$. Labelled are the local maxima L_1 to L_5 of the potential and the center of mass CM. The inner most equipotential line marks the Roche lobes of both stars, which are connected by L_1.

here again counters the gravitation. These points are global maxima of the potential. If a test mass is placed in rest at one of the points L_2 to L_5, the position of the mass will destabilize under a any perturbation. The position at the first Lagrange point, which is a saddle point, is stable perpendicular to the connection line of the stars.

If the companion of the compact object expands and fills its Roche lobe, plasma from its atmosphere passes through L_1 into the Roche lobe of the compact object. This is known as *Roche lobe overflow*. The matter is then gravitationally bound to the compact object and may form an accretion disc around the compact object, which is discussed further in Section 1.2.2.

Wind Accretion

If the atmosphere of the the companion does not extend to the critical potential, accretion via Roche lobe overflow is not possible. The companion star may, however, still lose matter through its stellar wind. For O- and B-type stars with surface temperatures above 20.000 K (Kippenhahn & Weigert, 1990) the mass loss rate due to the wind can be in the order of $\dot{M}_\mathrm{w} = 10^{-6}$-$10^{-4}\,\mathrm{M}_\odot\ \mathrm{yr}^{-1}$. Hence, even if only a small fraction of the wind is accreted by the compact object the meassured X-ray luminosities L_x can be reached. This mechanism is called *wind accretion* and was first suggested by Bondi & Hoyle (1944).

In general, the angular momentum of the stellar wind can be neglected. The wind velocity is approximately the escape velocity from the surface of the star (Frank et al., 1992) and the wind can be described by a constant gas flow. If the gas passes within a certain radius r_acc from the compact object, it is affected by the gravitational field of the compact object and can be accreted. The kinetic energy of the gas is equal to the

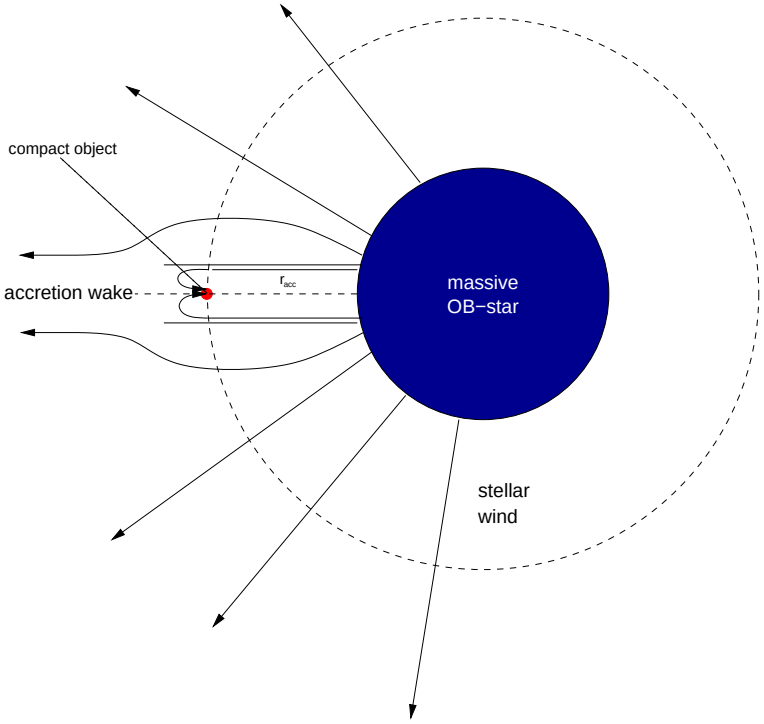

Figure 1.4: The wind accretion geometry depends on the accretion column, which is defined by the radius r_{acc} (Kreykenbohm, 2004, Fig. 2.8, according to Bondi & Hoyle, 1944). Within this radius the wind material is accreted by the compact object. Behind the compact object an accretion wake forms. The size of the compact object is not to scale.

gravitational potential at this radius and it follows

$$r_{\mathrm{acc}} = \frac{2GM_{\mathrm{x}}}{v_{\mathrm{w}}^2} \tag{1.10}$$

with the mass M_{x} of the compact object and the wind velocity v_{w}. Here the velocity of the neutron star is neglected. Therefore the total amount of accreted matter can be calculated as the content of a cylindric volume with radius r_{acc} and height a, which is the distance from the star to the compact object (compare Figure 1.4). The continuation of this volume behind the compact object, where the wind density is low due to accretion, is the *accretion wake*. If the wind geometry is spherical, the accretion rate $\dot{M}_{\mathrm{acc}}$ is given by

$$\dot{M}_{\mathrm{acc}} = \dot{M}_{\mathrm{w}} \frac{r_{\mathrm{acc}}^2}{4a^2} \tag{1.11}$$

Usually the accretion radius r_{acc} is much smaller than the binary separation a. As a consequence, wind accretion is inefficient since most of the wind matter is lost to the interstellar medium. The formation of an accretion disc is possible, but unlikely (for details see Boerner et al., 1987).

Transient Mechanism

The following accretion mechanism is the most important one in this thesis, since it is the mechanism of the binary GRO J1008–57 discussed in Chapter 4. In these binaries the optical companion is a Be type star, where “e” stands for Hydrogen emission lines observed in its spectrum. The lines originate in the circumstellar disc, which forms at the equator of the Be star due to its fast rotation. The matter is ionized by the radiation of the star itself and emission lines appear in its spectrum. The highly eccentric orbit of the

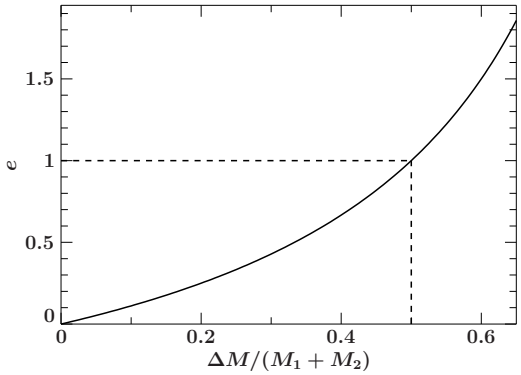

Figure 1.5: Change of the eccentricity e of the binary orbit by mass loss according to Equation 1.12. The relative mass $\Delta M/(M_1+M_2)$, where M_1 and M_2 are the components masses, is ejected into the interstellar medium during the supernova explosion.

compact object around the optical companion is a result of the prior supernova explosion. The mass ΔM ejected into the interstellar medium during the supernova is lost from the binary system and the eccentricity e of the orbit of both stars, which is assumed to be circular ($e = 0$) before the explosion, changes to (Verbunt & van den Heuvel, 1995):

$$e = \frac{\Delta M}{M_1 + M_2 - \Delta M} \tag{1.12}$$

Here M_1 and M_2 are the masses of the components of the binary. If ΔM is larger than 50% of the total mass of the system, the eccentricity will be larger than one, leading to an unbound system (see Figure 1.5). Therefore a binary would have to lose less than a half of its mass during the supernova explosion, which is highly unlikely (see Section 1.1.3). A more sophisticated explanation is a mass transfer from one component to the other before the first undergoes a supernova explosion. In that case less mass can be ejected into space. Because of angular momentum transfer onto the later optical companion it will spin up, leading to high velocities at its equator and the formation of a circumstellar disc. Be type stars, however, are also observed as isolated stars. Hence mass transfer alone cannot explain their existence.

Mass accretion is possible if the compact object passes the circumstellar disc. Due to the eccentric orbit of the compact object this happens during the periastron passage, when the distance of the compact object to the companion is at its minimum. Outside the periastron, where the disc density drops significantly, the X-ray luminosity decreases usually below the detection limit. This means that these systems show regular outbursts separated by one orbital period (see Figure 1.6). Therefore those X-ray binaries are called *transient systems*. In some cases, e.g., XTE J1946+274 (see Section 3.4), a second outburst may arise at the apastron. This behavior is not fully understood yet. One scenario is based on an accretion stream, which is dragged by the gravitation of the compact object. At the apastron, where the velocity of the compact object is at its minimum, it gets overtaken by the stream and matter can be accreted.

The detailed accretion mechanism in Be transients is, however, still unknown. It is possible that, although the compact object is near the periastron, no X-ray outburst occurs. This can be explained by the absence of the circumstellar disc, confirmed by lack of emission lines, for example as observed in A0535+262 (Camero-Arranz et al., 2010) or GRO J1008-57 (Coe et al., 2007, see Section 4). There are basically two possbile ways how the disc is lost: in the first, all disc material is accreted by the compact object. Evidence for this is found in the sources mentioned before. In the second, the disc is blown into space by a strong stellar wind. To distinguish between the models simultaneous observations in X-rays and optical bands are necesssary as they allow to monitor the interaction of circumstellar disc with the compact object.

The transient accretion mechanism is further complicated if Roche lobe overflow and wind accretion are taken into account as well. Due to the elliptical orbit the distance

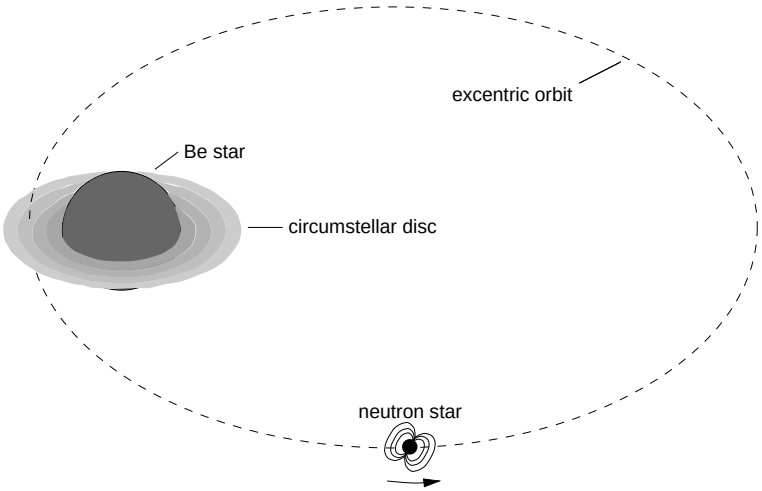

Figure 1.6: Schematic orbit of a compact object (here: a neutron star) in a transient X-ray binary (Kretschmar, 1996, Fig. 2.6). Due to the high eccentricity the compact object passes the circumstellar disc of the Be type companion around the periastron. This leads to an X-ray outburst.

between both components is periodically changing, leading to a time dependent Roche lobe potential (see Equation 1.9). Thus, besides accretion from the circumstellar disc, matter from the stellar atmosphere of the optical companion might be accreted as well. Outside of the periastron, wind accretion might is also possible. There the compact object is far away from the circumstellar disc and the mass density can be approximated by the wind density. As a consequence, if the Be star has a strong stellar wind the transient source is still visible in X-rays, even when it is not at periastron.

1.2.2 Accretion Discs

Once matter is gravitationally bound to the compact object it will move on Kepler orbits if its angular momentum is not zero. The angular momentum results, e.g., from the rotation of the donor star. If the mass density around the compact object increases, friction becomes important. The exerted angular momentum transfer broadens the Kepler orbits and an *accretion disc* forms. For inner orbits the released gravitational energy increases the temperature of this part of the disc. Hence, an angular momentum and a temperature gradient exist. The hot accretion disc is visible by its black body radiation. In black hole binaries the black body of the disc near the event horizon radiates in X-rays, while for white dwarfs or neutron stars as compact object the disc is visible in UV.

The strong magnetic field of neutron stars has a large impact on the accretion disc. For orbits around the neutron star below a certain radius, called *Alfvén radius*, the matter will follow the magnetic field lines. It can be calculated by considering the torque on the disc caused by magnetic pressure and the viscosity of the disc, which is connected to the mass accretion rate. The detailed calculation and the resulting formula can be found in Frank et al. (1992), Section 6.3.

Angular momentum transfer causes the outer layers of the accretion disc to be parallel to the equatorial plane of the companion star. In general the magnetic axis of the neutron star is inclined to the disc plane. Hence, the magnetic interaction forces the inner regions to follow the magnetic field lines as shown in the left panel of Figure 1.7. As a consequence of the different boundary conditions the disc is distorted. If the rotation axis of the donor star is not perpendicular to the orbital plane, the disc is in addition inclined with respect to the orbit. Warped and inclined accretion discs as, for example, found in the

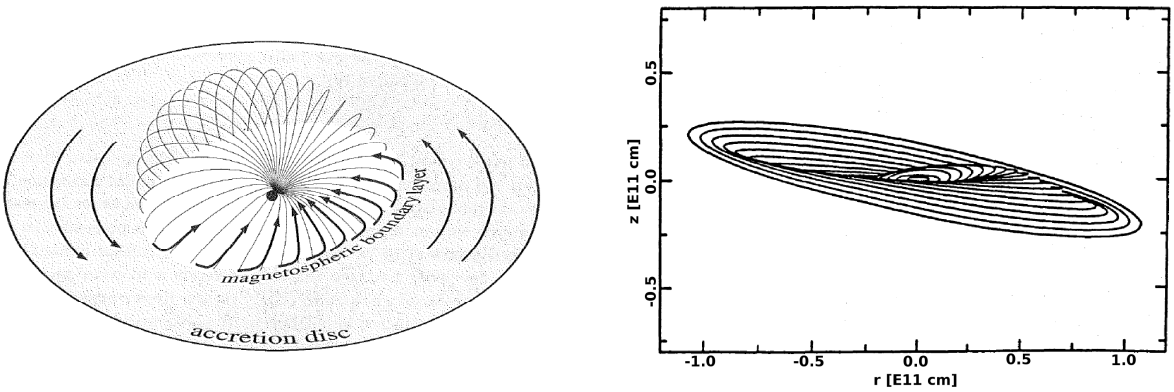

Figure 1.7: The strong magnetic field of the neutron star redirectes the matter of the accretion disc onto its magnetic poles. The magnetic axis is usually inclined to the disc plane (left panel, Frank et al., 1992, Fig. 6.3), which leads to a warped accretion disc as for example found in Hercules X-1 (right panel, Schandl & Meyer, 1994, Fig. 13)

.

X-ray binary Hercules X-1 are helpful to study magnetic plasma interactions (see right panel of Figure 1.7). However, detailed models to explain the observations are still under discussion.

1.2.3 Pulsars

The final step of mass accretion onto the surface of neutron stars is one of the most complex problems in accretion physics. The strong gravitational field requires relativistic calculations and the plasma is in addition influenced by high magetic fields. This conditions cannot be simulated in laboratory and therefore theoretical models are just approximations. The following description is based on the model by Becker & Wolff (2005), which treats many aspects of accretion physics.

Once the plasma follows the magnetic field lines below the Alfvén radius, an accretion flows to each magnetic pole forms (see left panel of Figure 1.8). Close to the neutron star the flows are concentrated in an accretion column by the higher density of magnetic field lines. Once the matter hits the surface with supersonic velocity, the total kinetic energy is used to heat the accretion area due to the nearly incompressible neutron star crust. For this reason these areas are called *hot-spots*. The resulting black body radiation between 1 and 10 keV can be seen in spectra of several accreting neutron stars. However, a black body does not explain the observed hard X-ray flux up to 100 keV. As explanation inverse Compton scattering is assumed: the soft X-ray photons originating from the hot-spot are upscattered to higher energies by relativistic electrons of the accretion flow (see right panel of Figure 1.8). Calculations suggest a powerlaw as resulting spectrum in addition to the black body radiation.

The interaction of the photons with the infalling plasma results in a shock front, whose height above the neutron star surface depends on the mass accretion rate $\dot{M}$. The matter hitting the shock front is heated up and slowly sinks down to the surface. The hot plasma is also visible by black body radiation, resulting in an effectivly larger hot-spot area. Because the density below the shock front is high, the hard X-rays created by inverse Compton scattering are more absorbed in infalling direction. Therefore most of the radiation is released sideways to the accretion column. Accordingly this emission geometry is called *fan beam*. For lower mass accretion rates a shock front does not form. The hard X-ray photons are less absorbed in direction to the accretion column, which is then called *pencil beam*.

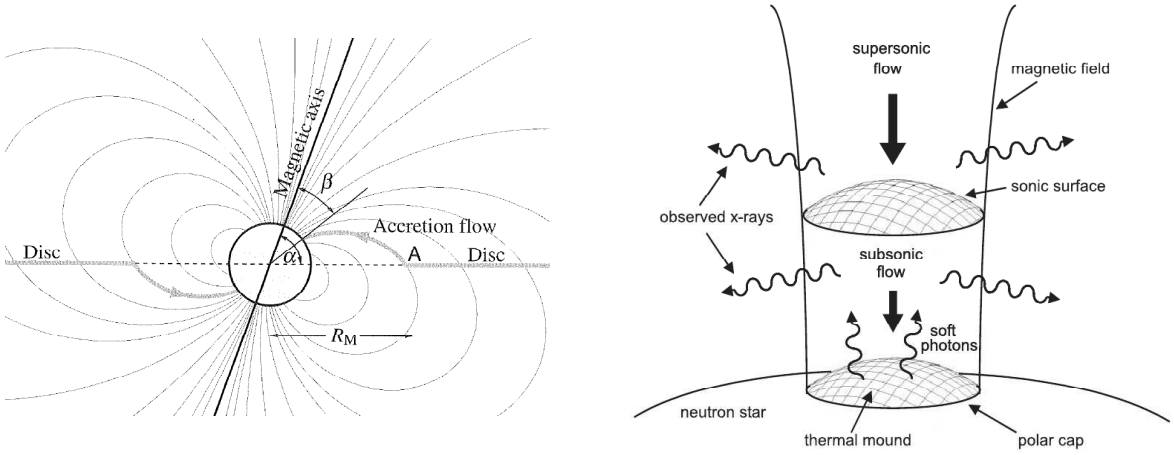

Figure 1.8: Left: below the Alfvén radius R_M the plasma of the disc follows the magnetic field lines onto the neutron star (Frank et al., 1992, Fig. 6.4). The accretion regions at the magnetic poles can be described by the angle β between the magnetic axis and the trajectory of the plasma flow. The magnetic axis itself is inclined by the angle α with respect to the disc plane. Right: The black body radiation of the hot-spot on the surface is inverse Compton scattered by the accretion flow (Becker & Wolff, 2005, Fig. 1). This leads to observable X-rays.

With increasing mass accretion rate $\dot{M}$ the corresponding luminosity L_x generates an even higher radiation pressure. At some point the pressure counterbalances the infalling material, which would lead to a lower luminosity and hence to less pressure. Therefore a natural luminosity limit exists, which is named *Eddington limit* and depends on the mass M of the compact object (Frank et al., 1992):

$$L_\mathrm{Edd} = 1.3 \times 10^{38} (M/M_\odot)\,\mathrm{erg\,s^{-1}} \tag{1.13}$$

The maximum mass accretion rate then can be found by comparing this limit with the theoretical luminosity of an accreting neutron star, which is given by (Frank et al., 1992)

$$L_\mathrm{acc} = 1.3 \times 10^{36} \dot{M}_{16} (M/M_\odot)(10\,\mathrm{km}/R)\,\mathrm{erg\,s^{-1}} \tag{1.14}$$

where R is the radius of the neutron star and $\dot{M}_{16} = \dot{M} \times 10^{16}\,\mathrm{g\,s^{-1}}$ the mass accretion rate. The typical values of a neutron of $R = 10\,\mathrm{km}$ and $M = 1\,\mathrm{M}_\odot$ lead to a maximum mass accretion rate $\dot{M}_\mathrm{max}$ in the order of $10^{-7}\,\mathrm{M}_\odot\ \mathrm{yr}^{-1}$. The above equations, however, assume a spherical and steady mass accretion, which is in general not applicable to X-ray binaries.

The X-ray lightcurve of a large number of accreting neutron stars show periodic and well defined pulsations. Thus the binary is called an *X-ray pulsar*. As in the case of the Earth the magnetic axis of the neutron star is not aligned to the rotation axis. As a result the observing geometry of the accretion regions on the magnetic poles changes with time. Further on this geometry periodically recurs with the rotation period of the neutron star. The pulse period P is, therefore, equal to the rotation period. The X-ray beam, whether a fan- or pencil-beam, is observed similar to a lighthouse. Pulsations, however, are not observed if the magnetic field of the neutron star is too weak to redirect the matter to its poles.

The pulse period P of a neutron star is not constant over time. The angular momentum of the accreted matter has to be conserved, hence the compact object spins up or down, depending on the accretion geometry. The strength of the spin change $\dot{P}$ depends on the amount of accreted matter, which can be described by $\dot{M}$. This is connected to the luminosity L by Equation 1.14 and theoretical calculations leads to (for details see, e.g.,

Table 1.2: Classification of X-ray binaries consisting a neutron star (according to Stelzer, 1997, based on Ghosh et al., 1977 and 1979a)

	HMXB		LMXB
Companion	O- or B-type star	Be-star	
	$\geq 10\,M_\odot$		$\leq 1\,M_\odot$
Accretion mechanism	wind	transient	Roche lobe overflow
Pulsations	yes	yes	no
Orbit	circular	elliptical	circular
Orbital period	$\leq 10\,d$	$\geq 20\,d$	

Frank et al., 1992):

$$\dot{P} \propto L^{6/7} \approx L \tag{1.15}$$

The linear approximation is motivated by observations and can be explained by the complexity of the accretion process. The assumptions made during the calculations are, as already mentioned before, spherical mass accretion, which is not the case if the matter is redirected onto the magnetic poles. The steadiness of the accretion flow can be easily distorted if the donor star is variable or clumps form in the accretion disc, for example. To account for the approximations and describe the observed pulse period $P(t)$, it is expressed as a Taylor expansion at an arbitrary time t_0:

$$P(t) = \sum_{k=0}^{\infty} \underbrace{\left.\frac{\partial^k P}{\partial t^k}\right|_{t=t_0}}_{P^{(k)}} \frac{t^k}{k!} \tag{1.16}$$

The coefficients $P^{(k)}$ of each order are known as the *pulse ephemeris*. In practice they are named $(P_0, \dot{P}, \ddot{P}, ...)$, but this notation might be misleading since these values are bound to the expansion point t_0.

1.2.4 Classification

As discussed in the previous sections the properties of X-ray binaries can be very different. The most important factor is the mass of the companion star. In so-called *High Mass X-ray Binaries* (HMXB) the compact object mainly accretes the strong stellar wind of the massive donor star or the circumstellar disc. Contrary, efficient mass accretion in *Low Mass X-ray Binaries* (LMXB) is only possible via Roche lobe overflow. This leads to further observable characteristics, which are summarized in the Table 1.2. The lack of pulsations in LMXBs is based on the weak magnetic field of the neutron star, because the matter is not redirected onto the magnetic poles. Due to the low mass the optical companion evolves very slowly compared to high mass systems (see Section 1.1.1). Therefore, LMXBs are in general old binaries. At this long time scales a decay of the magnetic field of the neutron star might take place, which would explain the observations. The physical reasons, however, are subject of current research (see Urpin & Geppert, 1995, and references therein).

1.2.5 Spectral Continuum Models

Mass accretion onto neutron stars is a complex physical process. However, broad band X-ray spectra in the range of 1 to 100 keV can be described by relatively simple models.

Since the detector is counting individual photons (see Section 2.1), the models are given as photon flux density $S_{\mathrm{E}}(E)$, depending on the photon energy E:

$$S_{\mathrm{E}}(E) = \frac{\mathrm{d}N}{\mathrm{d}t\,\mathrm{d}A\,\mathrm{d}E} \tag{1.17}$$

where $\mathrm{d}N$ is the number of photons detected during the time interval $\mathrm{d}t$ per area $\mathrm{d}A$ and in the photon energy interval $[E, E + \mathrm{d}E]$.

As described in the previous sections, the accretion disc and the hot spots on the neutron star surface are visible by black body radiation. The corresponding blackbody flux can be modelled by

$$\texttt{bbody}(E) = 8.0525\, N\, \frac{E^2}{(kT)^4\,(e^{E/kT} - 1)} \tag{1.18}$$

Here kT is the temperature of the black body and N the normalization, which corresponds to the source's flux and is given in $10^{39}\,\mathrm{erg\,s^{-1}}\,(10\,\mathrm{kpc})^{-2}$.

The inverse Compton scattering of the soft X-ray photons leads to a powerlaw as discussed in Section 1.2.3:

$$\texttt{powerlaw}(E) = NE^{-\Gamma} \tag{1.19}$$

The dimensionless exponent Γ is named the photon index and the normalization represents the flux in photons per second, area and energy at 1 keV. Typical neutron star spectra, however, show an exponential cutoff for energies above 20 to 40 keV. This behavior can be explained by Comptonization or Bremsstrahlung radiation, which results from the movement of electrons in a thin thermal plasma (Becker & Wolff, 2007). The calculated spectra are in agreement with a cutoff powerlaw, which has been used in the past to empirically model X-ray spectra:

$$\texttt{cutoffpl}(E) = \texttt{powerlaw}(E) \cdot e^{-E/E_{\mathrm{cut}}} \tag{1.20}$$

Here the spectrum above the cutoff energy E_{cut} is dominated by an exponential decay.

The inverse Compton scattering also predicts a contribution of bremsstrahlung radiation to the spectrum Becker & Wolff (2007). Unfortunately the corresponding model `bremss` cannot be calculated analytically. Rather it consists of polynomial fits to numerical values (Kellogg et al., 1975; Karzas & Latter, 1961). The parameters of the model are a characteristic plasma temperature kT and a norm N based on the distance to the source and the ion and electron densities.

In 1995 Mihara invented a model, which consists of two cutoff powerlaws with different signs in their photon indices. Therefore, it was named `NPEX` (Negativ Positive EXponential):

$$\texttt{NPEX}(E) = (N_1 E^{-\Gamma_1} + N_2 E^{+\Gamma_2})\, e^{-E/kT} \tag{1.21}$$

The first powerlaw is the usual high energy component produced by inverse Compton scattering. In combination with the exponential decay a cutoff powerlaw results, according to Equation 1.20. However, the cutoff energy E_{cut} is replaced by the plasma temperature kT in that case. The second powerlaw describes the black body radiation, if its photon index Γ_2 is near 2 as required by Equation 1.18. Due to that it is often fixed to this value. The physical motivation for this model is the coupling between the accretion hot spot and the upscattered X-ray photons in the accretion column, which results in a cutoff powerlaw.

Photoelectric Absorption

The flux of all continuum models is absorbed by the interstellar medium (ISM) before it is detected by a satellite. The measured flux $S_{\rm obs}(E)$ is then given by (see, e.g., Wilms et al., 2000):

$$S_{\rm obs}(E) = \underbrace{e^{-\sigma_{\rm ISM}(E)\,N_{\rm H}}}_{\texttt{tbnew(E)}}\, S_{\rm E}(E) \tag{1.22}$$

The absorption cross section $\sigma_{\rm ISM}(E)$ is, of course, energy dependent and cannot be measured directly. Therefore theoretical estimations and assumptions have to be made, combined with cross-sections measured in laboratories. X-ray photons interact with neutral atoms, such as H, O, Ne or Fe, by photoionization. The most abundant atom in the ISM is hydrogen, hence the cross-section is normalized by the hydrogen column density $N_{\rm H}$. It is given in atoms cm^{-2}, as common in X-ray astronomy.

The interstellar cross section $\sigma_{\rm ISM}(E)$ used for spectra modelling in this thesis (see Section 4.3) is set to Wilms et al. (2000). Their model takes several cross sections into account:

$$\sigma_{\rm ISM}(E) = \sigma_{\rm gas}(E) + \sigma_{\rm molecules}(E) + \sigma_{\rm grains}(E) \tag{1.23}$$

where $\sigma_{\rm gas}(E)$ is the cross section for neutral atoms, $\sigma_{\rm molecules}(E)$ for hydrogen molecules, the main composition of interstellar molecules, and $\sigma_{\rm grains}(E)$ for dust grains. The details about each cross-section are not discussed here any further. The X-ray photons also interact with electrons of the ISM by Thomson scattering, which is neglected in this model because the effect is low for column densities below $N_{\rm H} \sim 10^{22}\,\mathrm{cm}^{-2}$. The same holds true for Compton scattering on bound electrons in molecules. Further on, the cross-sections also depend on the abundances in the ISM, which are assumed to be constant between the source and the observer. As already mentioned laboratory based cross-sections for individual atoms have to be known. The cross-section table in this thesis is set to Verner et al. (1996). Calculations show that the cross-section dropps significantly for photon energies above $\sim 10\,\mathrm{keV}$. Hence interstellar absorption plays a role for lower energies only.

1.2.6 Spectral Line Features

Photoionization also leads to line features in X-ray spectra. Such emission lines form, e.g., after a high energy X-ray photon has kicked an electron of an atom's K-shell. The vacancy is replaced subsequently by an electron of a higher shell, most likely of the L-shell. Here an X-ray photon of the energy $\Delta E = E_{\rm L} - E_{\rm K}$ gets emitted, visible as a fluorescence line, which is named *Kα-line*. It is possible to grab an electron of even higher shells as well, resulting in Kβ-, Kγ-lines and so on. The probability of higher transitions, however, decreases exponentially with ΔE. The resulting emission lines are often modelled by a Gaussian at the mean energy E_0 with the width σ and area A:

$$\texttt{gauss}(E) = \frac{A}{\sigma\sqrt{2\pi}} \exp\left(-\frac{(E-E_0)^2}{2\sigma^2}\right) \tag{1.24}$$

The most prominent fluorescence line in neutron star spectra arises from ironA fraction of the material is still bound to the binary and figuratively forms an iron cloud. The energy of the emitted photon is 6.4 keV and can be measured well in the laboratory. This energy might be shifted if the material producing the line moves relativistically as found, e.g., in black hole binaries. For neutron stars the iron cloud usually is not relativistic, hence the energy is commonly fixed to its rest frame energy. The fraction of the iron line on the overall flux depends strongly on the observed source. For example, the relative flux between 2 and 10 keV of GRO J1008–57 (see Section 4) is around 0.2%, while in GX 302–1 the iron line dominates the spectrum with a fraction of 12% (F. Fürst, priv. comm.).

Cyclotron Resonant Scattering Features

The following calculation is based on Schönherr (2007).

Due to the Lorentz force the motion of an electron perpendicular to the magnetic field lines is circular. Combined with the unaffected parallel motion the trajectory of the electron describes a helix along the magnetic field. In classical physics the radius of the circular motion, named *gyration radius*, is given by

$$r_{\mathrm{gyr}} = \frac{m v_{\perp}}{eB} \tag{1.25}$$

where B is the magnetic field strength and $v_{\perp}$ is the velocity perpendicular to the magnetic field lines. With increasing B the radius shrinks, and if it gets near the *de Broglie* wavelength

$$\lambda_{\mathrm{dB}} = \frac{\hbar}{m v_{\perp}} \tag{1.26}$$

quantum effects become important. Hence the perpendicular motion, expressed in kinetic energy, is quantized in so-called *Landau levels* (e.g., Schwarm, 2010):

$$E_{\mathrm{n}} = m_{\mathrm{e}} c^2 \sqrt{1 + \left(\frac{p_{\parallel}}{m_{\mathrm{e}} c}\right) + 2n \frac{B}{B_{\mathrm{crit}}}} \tag{1.27}$$

Here n is the Landau level number and B_{crit} the critical magnetic field strength, where the cyclotron energy will be in the order of the electron rest energy. In that case relativistic effects have to be considered in Equation 1.27. If $B_{\mathrm{crit}} \ll B$, however, a Taylor expansion of Equation 1.27 leads to

$$E_{\mathrm{n}} = E_0 + mc^2 n \frac{B}{B_{\mathrm{crit}}} \tag{1.28}$$

where $E_0 \equiv E_{\mathrm{cyc}}$ is the *fundamental energy*. Thus the difference between two energy levels is approximately given by the so-called *12-B-12 rule*:

$$E_{\mathrm{cyc}} = 11.6\,\mathrm{keV} \times B_{12} \tag{1.29}$$

where B_{12} is the magnetic field strength in units of $10^{12}\,\mathrm{G}$

It is possible to excite an electron at the Landau level n to a higher level $n+1$ by absorption of an X-ray photon, whose energy $h\nu$ is equal to the fundamental energy E_{cyc}. Hence, an absorption line is expected at this energy, called *fundamental line*. The excited electron will decay to a lower level by re-emitting a photon after a certain lifetime. Latal (1986) showed, however, that this lifetime is extremly short (in the order of $10^{-15}\,\mathrm{s}$). The photon is nearly instantly re-emitted, hence the process is more a scattering than an absorption and therefore called *cyclotron resonant scattering feature* (CRSF). In principle there are two possibilities how an excited state at level n can decay: directly to the ground level or consecutively to the next lower level until the ground level is reached. The latter results in the emission of n photons of the fundamental energy E_{cyc}. Based on this *photon spawning*, Yahel (1979) conclude that despite from an absorption lines an emission line at E_{cyc} should form. In the same year, however, Herold (1979) calculated the mean free path of photons with the energy E_{cyc} in the accretion column. Due to the scattering of those photons with the Landau levels of the electrons, the photons are nearly trapped in the accretion plasma. As a conclusion they cannot be observed unless the energy changes by inelastic scattering processes like the inverse Compton effect. Hence the fundamental line at E_{cyc} rather occurs as an absorption instead of an emission line. The lines at multiples $k \times E_{\mathrm{cyc}}$ of the fundamental energy are called first *harmonic* (k=2), second harmonic

(k=3), and so on (Nagel, 1981). However, some authors define the line at $k = 2$ to be the second harmonic. Cyclotron absorption lines in X-ray spectra are usually modelled using a simple absorption model without taking complex structures like emission wings into account:

$$\texttt{cyclabs}(E) = \exp\left(-\tau \frac{(WE/E_{\mathrm{line}})^2}{(E - E_{\mathrm{line}})^2 + W^2}\right) \tag{1.30}$$

Here τ is the depth of the cyclotron line, W its width and E_{line} the centroid energy, which is either set to multiples $k \times E_{\mathrm{cyc}}$ of the fundamental energy or fitted separately.

Knowing the fundamental energy is the only way to directly measure the magnetic field strength of a neutron star (compare Equation 1.29). More precisely one gets the field strength at the regions, where the cyclotron scattering takes places. Because high magnetic fields are required, these regions are expected to be near the surface of the neutron star. Due to the strong gravitational field the observed line energies are in addition redshifted:

$$E_{\mathrm{cyc}}^{\mathrm{obs}} = \frac{E_{\mathrm{cyc}}}{1 + z} \tag{1.31}$$

Here z is the gravitational redshift, which can be assumed to be around 0.3 for common values of neutron stars (see, e.g, Kreykenbohm, 2004). Further on, the accretion- and emission geometry of the photons influence the cyclotron energy and the line shapes. A relativistic approach reveals that the Landau levels are not equally spaced anymore and depend on the angle θ between the photon path and the magnetic field lines. The only way to predict the line shapes is to perform Monte Carlo simulations, which also handle photon spawning. Such simulations have been first performed by Araya & Harding (1999) and Araya-Góchez & Harding (2000). The modelled spectra show cyclotron absorption lines of complex shapes: in some cases *emission wings* occur around the fundamental line, caused by photon spawning. In extreme cases the latter might also lead to a filled up fundamental line or even in an emission feature. However, the physics of CRSFs is far from well-understood and is subject of actual research (Schönherr et al. 2007; Schwarm et al., in prep.).

So far 17 sources showing CRSFs or more have been discovered. The fundamental energy covers a wide range, starting at 10 keV for Swift J1626.6−5156 (DeCesar et al., 2009) to 88 keV for GRO J1008–57 (Shrader et al., 1999), which is also discussed within this thesis in Section 4. Also the number of observed harmonics is variable. At the moment, the HMXB 4U 0115+63 is the line leader with five confirmed cyclotron features, which can be seen in Figure 1.9 (see also Heindl et al., 1999; Santangelo et al., 1999, and references therein).

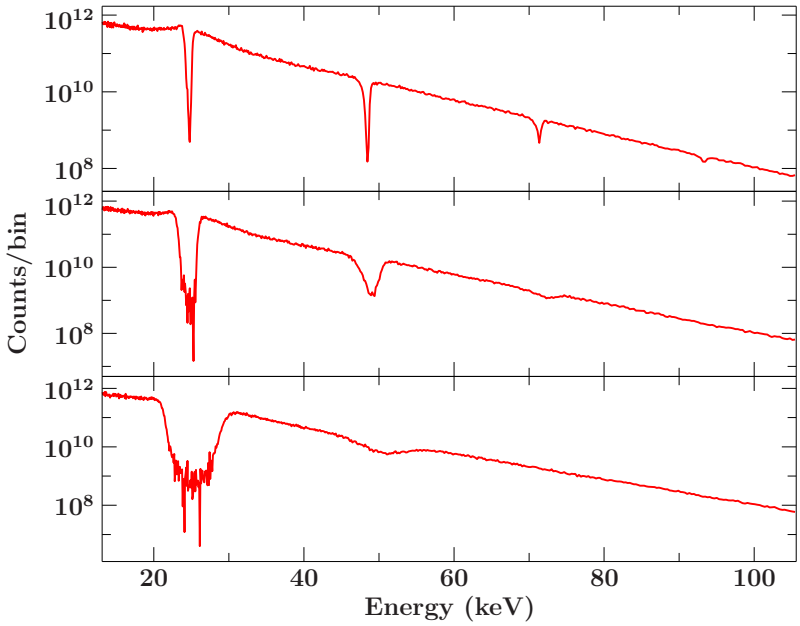

Figure 1.9: Simulation of Cyclotron Resonant Scattering Features including geometry and relativistic effects (F. Schwarm, priv. comm.). The angle between the observed photon and the accretion column decreases from top to bottom. Emission wings around the fundamental line are most prominent if the observer sees the accretion column from the side.

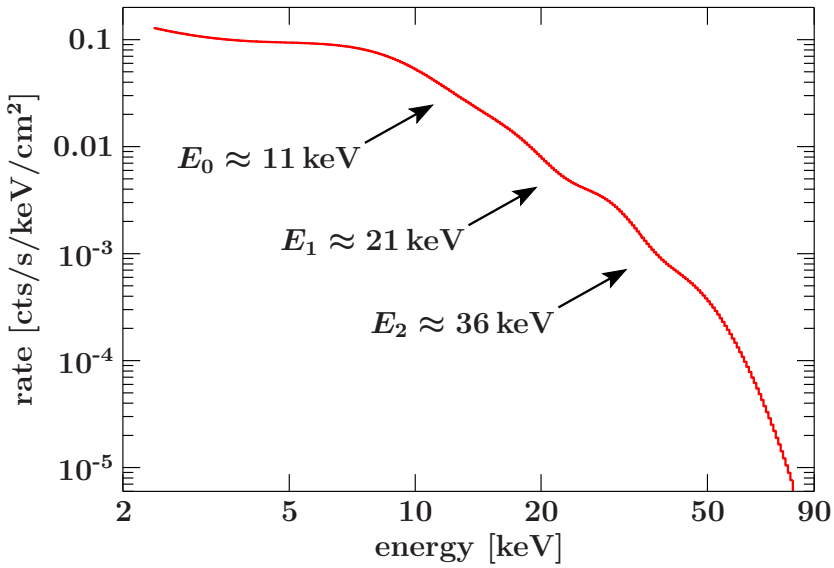

Figure 1.10: The modelled flux spectrum from 4U 0115+63 as observed in an outburst in 2008 (S. Müller, priv. comm.). The fundamental line as well as two higher harmonics are visible.

Chapter 2
X-ray Detectors

In order to detect of X-ray radiation several problems have to be solved: due to Earth's atmosphere, where X-rays are absorbed, detectors must be assembled on satellites. Restrictions in weight and costs are the result. A further problem in outer space is the cosmic radiation, whose flux can be as large as the source flux in some cases. Hence knowing the background for each source is mandatory. Most of the cosmic radiation is composed of high energetic particles and photons. The solar wind originating from Sun consist mainly of energetic protons and electrons and is also affecting the detector. The wind near Earth is interacting with its magnetic field and the particles are, for example, redirected to the magnetic poles, resulting in auroras. Another possibility is that particles are trapped around Earth in the so-called *van Allen belts* by the magnetic field of Earth at a height of approximately 1000 km (van Allen, 1958; van Allen et al., 1959). The magnetic field, however, has a dent in the south Atlantic, which allows the particles to penetrate the atmosphere down to 500 km. In consequence a much higher particle background is measured in this area, which is named *South Atlantic Anomaly* (SAA, see Figure 2.1). The science instruments passing the SAA are usually shut off to protect the electronics. Further on, any meassured X-ray flux is useless due to the high background.

Besides the background, the technology of detecting X-rays is challenging due to the low cross-section with matter. Since the radiation is ionizing, the detector material usually gets activated, leading to additional line features in the detected spectrum. The ionizing nature of X-rays, however, can be used to detect them. The corresponding detectors are, besides others, *proportional counters* and *scintillators*, which are described by the example of the X-ray satellite *RXTE* (see Section 2.2). A further problem detecting X-rays is that they cannot be focused by mirrors as, e.g., for optical radiation. Instead of simple reflection, however, total reflection is a possibility to focus X-rays, which is used in *Wolter type telescopes*. The NASA satellite *Swift* (see Section 2.3), takes images of X-ray sources using this method.

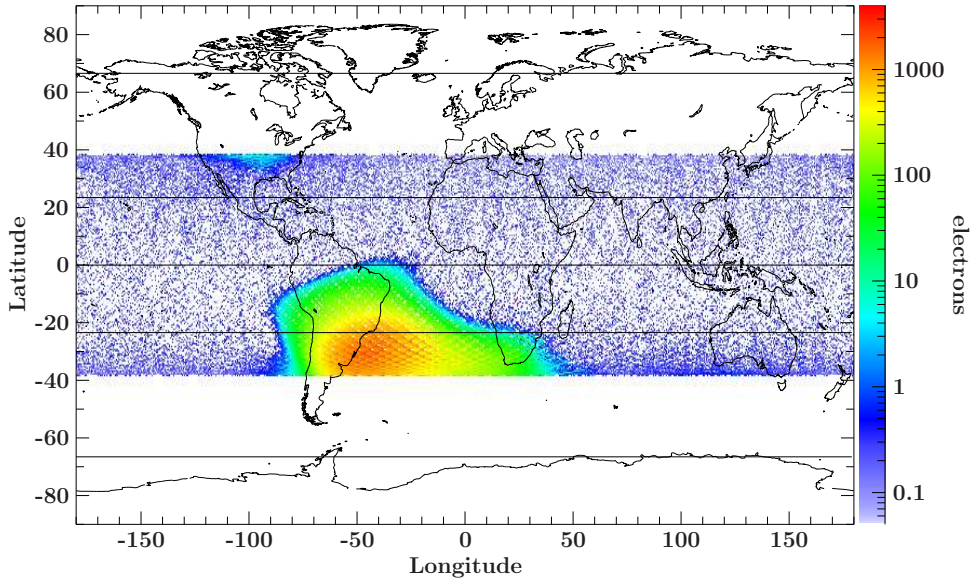

Figure 2.1: The South Atlantic Anomaly as meassured by *RHESSI* (N. Hell, priv. comm.). The electron rate is strongly enhanced above the South Atlantic ocean.

2.1 Response

Any detector cannot measure radiation of any energy with the same precision and efficiency. The incident X-ray flux therefore is not detected directly, though it is transformed into *detector space*. This transformation basically depends on two independent properties of the detector:

1. Due to the finite energy resolution of the detector an X-ray photon of the energy E is not always detected at the same energy. In fact there is a probability distribution to detect this photon at a certain energy E'. The corresponding function $R(E', E)$ is called *redistribution matrix function* (RMF). The detected photons are collected in energy bins B_i, which are defined as a certain energy interval between E_i and E_{i+1}. Therefore, the RMF is given as $R(i, E)$.
2. The efficiency to detect a photon of the energy E is based on the detailed detection mechanism. This in turn depends on the effective area of the detector and contamination effects, produced by the activated detector material. The effective area is comparable with the size of the mirrors used in optical telescopes: the larger the area the more photons can be detected. Other energy dependent effects, like the quantum efficiency of a *Charged Coupled Device* (CCD, see Section 2.3 for details), are also included in this *ancillary response function* $A(E)$ (ARF), whose unit is cm^2.

To transform an incident photon flux $S_\mathrm{E}(E)$ given as photons $\mathrm{s}^{-1}\,\mathrm{cm}^{-2}\,\mathrm{keV}^{-1}$ (see Section 1.2.5) into detector space, the above functions have to be multiplied in the first step. Because the information of the number of photons is lost by applying this transformation, the notion "photons" is misleading and replaced by "counts". Hence, the product $R(i, E) \cdot A(E)$, named *response function* (RSP), results in the detected counts in the energy bin B_i per incident photon flux. The next step is to fold the incident flux $S_\mathrm{E}(E)$ with the RSP. The result is the transformation[1] of this flux into the number of counts

[1] see also Arnaud et al. (2007):
http://heasarc.gsfc.nasa.gov/docs/xanadu/xspec/

$C(i)$ in each energy bin i after an exposure time t_{exp}:

$$C(i) = C_{\mathrm{back}}(i) + t_{\mathrm{exp}} \cdot \int \mathrm{d}E \; R(i,E) \cdot A(E) \cdot S_{\mathrm{E}}(E) \tag{2.1}$$

Here $C_{\mathrm{back}}(i)$ are the counts caused by the background flux. The unit of $C(i)$ is given as counts bin^{-1}. Unfortunately the incident photon flux $S_{\mathrm{S}}(E)$ cannot be obtained from the measured counts, since Equation 2.1 is not invertible. If the RMF $R(i,E)$ is assumed to be a unity matrix, the photon flux could be calculated, which is called *flux-corrected spectrum* $\tilde{S}_{\mathrm{E}}(i)$ (Nowak, 2004):

$$\tilde{S}_{\mathrm{E}}(i) = \frac{C(i) - C_{\mathrm{back}}(i)}{t_{\mathrm{exp}} \cdot \int_{E_i}^{E_{i+1}} \mathrm{d}E \; R(i,E) \cdot A(E)} \tag{2.2}$$

This spectrum, however, should not be used for analysis due to the required approximation. But flux-corrected spectra are not depending on the detector anymore. Hence they can be used, for example, to simulate the spectrum of a source as measured by other detectors.

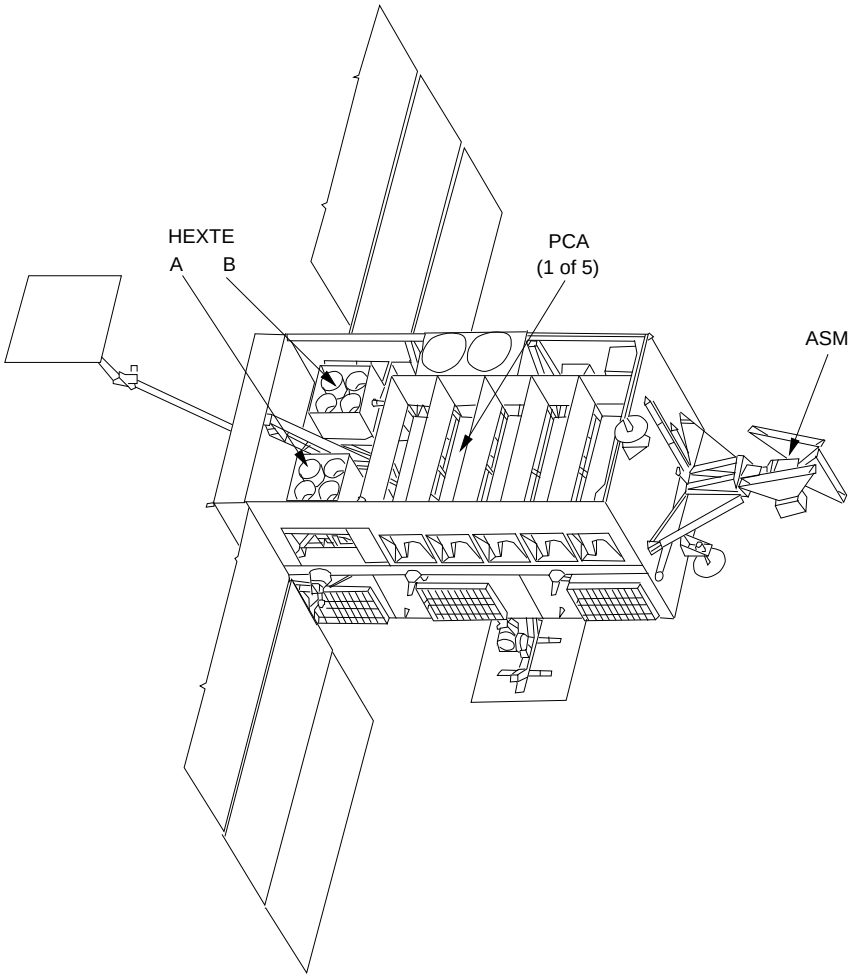

Figure 2.2: The Rossi X-ray Timing Explorer (Wilms, 1998, Fig. 4.1).

2.2 Rossi X-ray Timing Explorer

The *Rossi X-ray Timing Explorer* (*RXTE*) was launched in 1995 into an orbit about 580 km above Earth. Therefore one orbit will take nearly 90 minutes. Because of the satellite's altitude it is affected by the SAA (see Section 2). The voltage of the proportional counters is lowered or shut off during the SAA passage. The energy of X-ray radiation detected by the instruments onboard *RXTE* ranges from 2 keV up to 250 keV. This wide energy coverage is achieved by two different instruments:

1. The *Proportional Counter Array* (PCA) is sensitive for radiation between 2 and 60 keV and was built at the Goddard Space Flight Center (GSFC) (Jahoda et al., 1996). The PCA itself consists of 5 identical detectors, the *Proportional Counter Units* (PCUs). By combining the measurements of each unit a higher signal to noise ratio is achieved.
2. For high energies between 15 and 250 keV the *High Energy X-ray Timing Experiment* (HEXTE; Rothschild et al., 1998) is used on *RXTE*. This instrument was built at the Center for Astrophysics and Space Sciences (CASS) and consists of two identical detectors. But contrary to PCA, the signal of both detectors cannot be summed up, because the detectors alternate between measuring the background and the source flux.

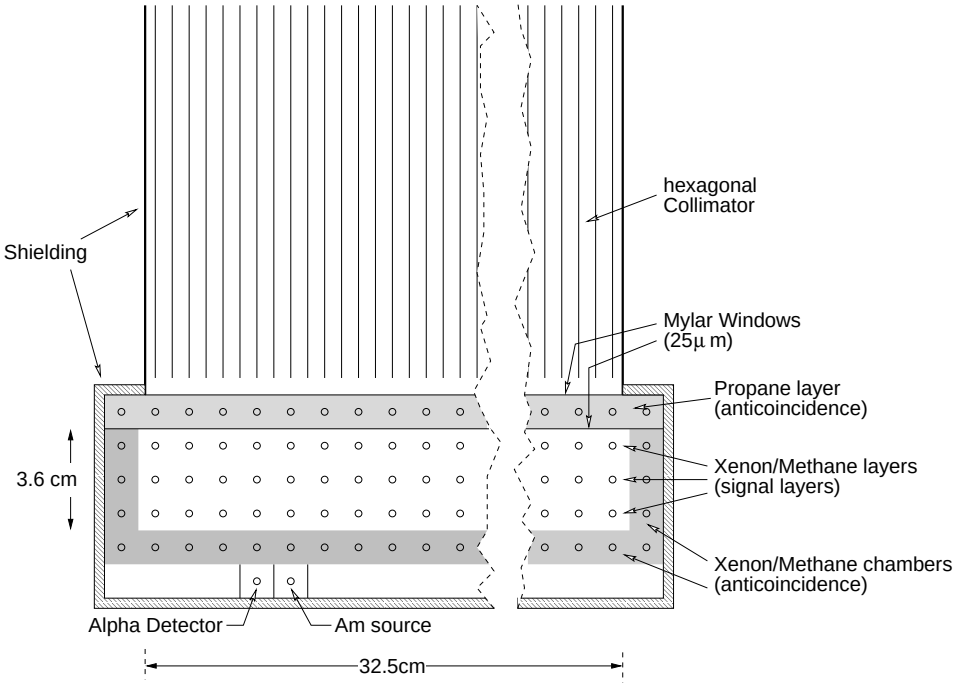

Figure 2.3: Scematic overview of one of the PCUs, which five of them make the PCA (Wilms, 1998, Fig. 4.2). A detailed description is given in the text.

Both detectors are described in detail later on, based on the technical appendix F[2]. A third instrument, the *All Sky Monitor* (ASM; Levine et al., 1996) built at the Massachusetts Institute of Technology (MIT), is assembled to *RXTE*. Its purpose is to detect any changes on the X-ray sky, for example the outburst of a previously unknown transient X-ray binary. Three cameras with a field of view of $90° \times 6°$ point in three different directions. After ninety seconds the position of each camera changes, thus most part of the sky, besides the regions near Sun, are covered over one day. If something important is found, the spacecraft can be moved to start observing the point of interest with PCA and HEXTE. The slewing speed of *RXTE* of about 6° per minute is high enough to point to any direction on the sky within one hour. Due to the large field of view, the determination of the position of a detected source is quite complicated: a coded mask is assembled on top of each camera. From the resulting shadowgram the position of the source is calculated, which is not discussed here any further. For details about the mathematics of coded masks see Willmore et al. (1992) and references therein.

2.2.1 Proportional Counter Array

The PCA detector consists of five identical subdetectors, the PCUs, which are labeled PCU0 to PCU4. Each detector consists of several layers: a single propane layer on top of four xenon layers (see Figure 2.3). Each layer is a full functional proportional counter, which is described briefly in the following according to Grupen (1993).

A photon entering the gas chamber of the proportional counter ionizes some atoms of the gas, if the cross-section for ionization is high enough. This depends on the used gas as well as the photon energy. The free electrons released by the ionized atoms are accelerated to an anode. While the kinetic energy of the electrons increase, they collide with further electrons, which are still bound to atoms. If the energy is high enough, these atoms are ionized as well. These electrons may ionize further atoms, which results in

[2]see http://heasarc.gsfc.nasa.gov/docs/xte/appendix_f.html

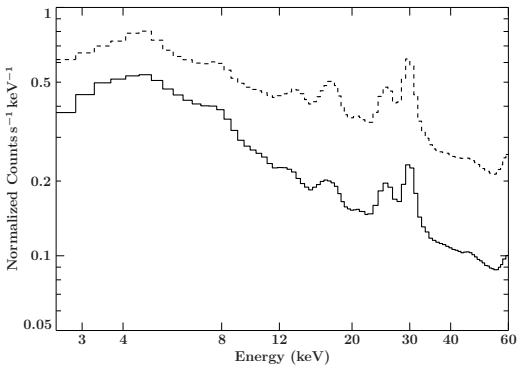

Figure 2.4: The modelled background of PCU2. The solid line shows the top xenon layer only, while the dashed line all three layers. Both backgrounds show the same features: the high count rates below 8 keV are caused by the xenon L-edge, which representes the minimum energy needed to ionize an L-shell electron and results in a fluorescence photon. The xenon K-edge is also visible around 34 keV as well as further line features due to activated detector material. The background of the top xenon layer is, however, relatively lower above 8 keV.

an avalanche of electrons. They are then detected as electric current at the anode. Due to the fact that the current is nearly proportional to the incident photon energy, these detectors are called proportional counters.

In each layer of a PCU, a net of anodes is used instead of a single anode. The introduction of further anodes leads to a reduced acceleration path of the free electrons. Hence the maximum kinetic energy of the electrons is restriced. In the case that the energy gets too high, electrons of lower shells are ionized, which results in fluorescence photons. Those photons influence the free electrons of the signal, which finally leads to an uncorrelation of the incident X-ray photon and the measured electronic current: the energy information is lost.

The top and bottom layers of a PCU are used as veto layers as well as the outer part of the anode net of each layer. This enables a distinction between source and background photons entering the detector from side or bottom. To further exclude photons from above, which do not originate from the source, a collimator on top of each PCU is used. This limits the field of view (FOV) to 1 degree, which is sufficient for most X-ray sources. There are sources near the galactic center, however, which are separated by some arc minutes only.

Despite of the limited FOV and the veto layers, the background signal is still present in the data. The background is caused by cosmic radiation and particles, mostly electrons and protons, and the detector material itself. This material is activated by high energy photons and particles, especially during the SAA passage (see Figure 2.1). Measuring the background of the PCUs is not possible during an observation as the detector is pointing on the source. Therefore the background has to be modelled and is shown in Figure 2.4.

The energy calibration of the PCU is done by an ^{241}Am source located below the last xenon layer. This radioactive isotope is an α-emitter with a characteristic line at 59.6 keV. In combination with an α-detector a measured photon of this energy can be assigned to the Americium source. The energy gain is therefore corrected automatically.

The combined effective area of all PCUs results in $\sim$6000 cm^2, if all PCUs are used, and the energy resolution is around 18% at 6 keV. The effective area of PCU2, as shown in the left panel of Figure 2.5, is highest at low energies around 10 keV and decreases quite fast. Hence the usable energy range for the PCA is between 2 and more or less 30 keV.

Since the first light of *RXTE* in 1996 the detectors are operating for 15 years now. During this time several technical problems arised: due to sparks in the xenon layers (Jahoda et al., 1996) of PCU3 and 4, all PCUs have to be shut down periodically to prevent further damage. In consequence there are only two of five PCUs available on average during observations. Further on, the high voltage had to be reduced, leading to a slightly higher energy coverage, but also to a worse energy resolution. In May 2000 the

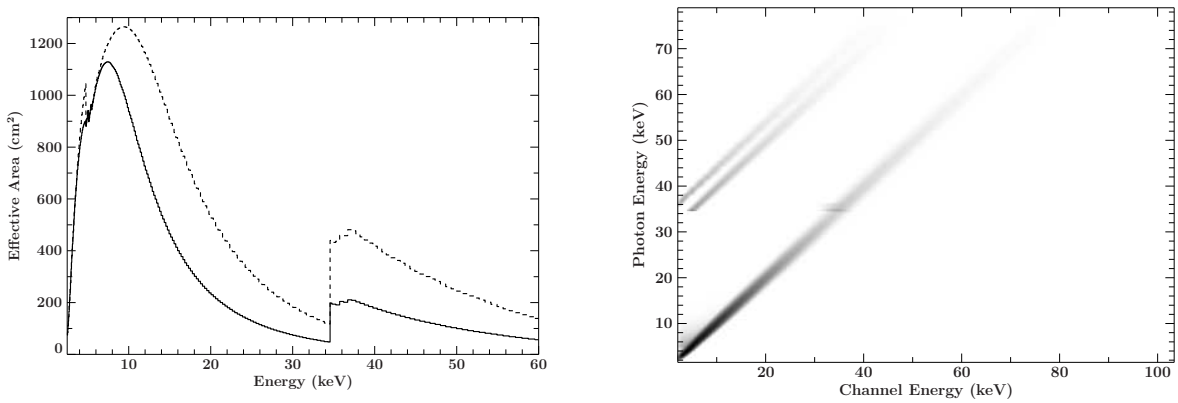

Figure 2.5: Left: the effective area of the top xenon layer of PCU2, shown as solid line, is highest at ∼8.5 keV. The maximum is shifted by 1 keV to higher energies using all five layers, which is shown as dashed line. Due to the Xenon L-edge at 34 keV, which leads to additional measurable electrons, the sensitivity jumps by a factor of 4. The top layer only is relatively more sensitive at energies below 20 keV. Right: the RMF of the top layer of PCU2 shows the nearly linear correlation between the incident photon energy and the channel energy. The two upper lines are caused by fluorescence photons, which result from electron Kα or Kβ transitions excited by and X-ray photon. The cross-section of these fluorescence photons is strongly decreasesed, hence they leave the detector without interaction. The energies of the corresponding peaks in the RMF are therefore called escape peaks.

propane layer of PCU0 emptied due to a hit by a micro meteorite, and the same happened with PCU1 in December 2006.[3] Thus the background for these PCUs is larger than for the remaining PCUs. All in all these events caused the background model and response function to be updated. The shown background in Figure 2.4 and the effective area and redistribution matrix in Figure 2.5 include all these corrections.

2.2.2 High Energy X-ray Timing Experiment

The second instrument onboard *RXTE* consists of two clusters labeled A and B, which itself are four scintillator detectors. Such a detector is basically made of a scintillator crystal and a photomultiplier tube (see Figure 2.6). A more detailed description of the following detection principle can be found in Gerthsen & Vogel (1993).

As for each PCU a collimator is mounted on top of each HEXTE cluster and limits the FOV to one degree. An X-ray photon entering the scintillator crystal, which is made of NaI(Ti), excites a certain number of electrons of the crystal. This number is correlated with the energy of the incident photon. The excited electrons itself re-emit fluorescence photons, which enter the quartz window, where they produce free electrons. The electrons are then multiplied by a photomultiplier, which results in a measurable electron current. The current is proportional to the incident photon and hence its energy can be determined. The energy calibration of HEXTE is similar to PCA done by an ^{241}Am source, but in contrast it is mounted inside the FOV.

The CsI(Na) crystal is used for background detection of photons entering the detector from the side or bottom. They can be distinguished from source events by a different decay time of the emitted light in the two crystals. An event is accepted only, if its decay time is equal to the one for the NaI(Ti) crystal of around 0.25 μs. The decay time for the CsI(Na) crystal is four times longer (Grupen, 1993). The total background of a HEXTE cluster, however, is much larger than in PCA. As shown in Figure 2.7 the

[3] see http://heasarc.gsfc.nasa.gov/docs/xte/whatsnew/big.html for details

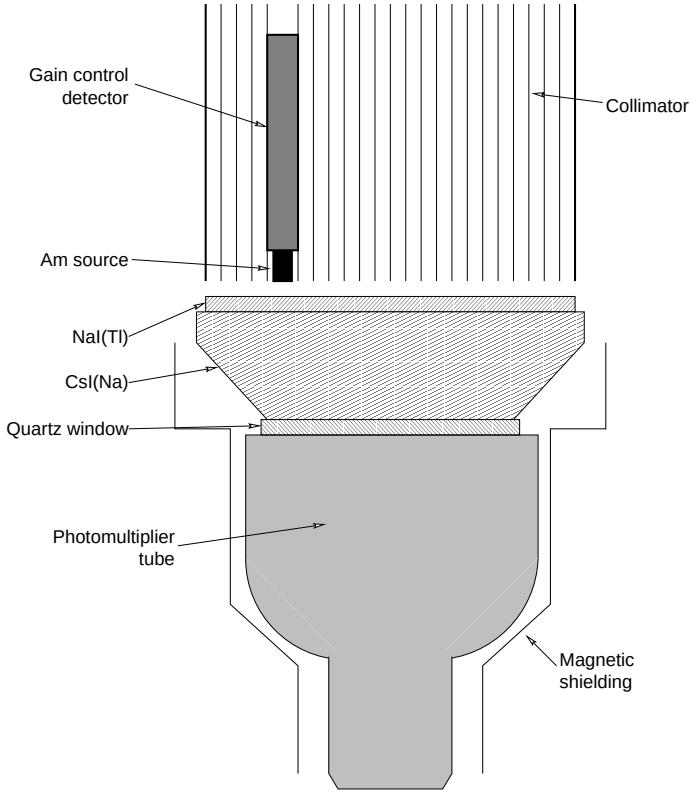

Figure 2.6: One of the HEXTE clusters as assembled onboard *RXTE* (Wilms, 1998, Fig. 4.7). For a detailed description see text.

background is dominanted by several iodine lines. In fact, the background flux is usually much higher than the source flux. To get a good signal, however, the background for a source is measured directly in contrast to PCA. Both clusters can be moved to point to three different positions: on-source, below and above the source position. The two off source positions are used to measure the background and are called plus and minus positions. The positions of both detectors are changed every 32 s in that way, that one detector is on-source while the other one is off source. Hence the background for the source is known at any time of the observation. This behavior is called "rocking".

The effective area of both HEXTE clusters combined is around $\sim$1500 cm^2 at 50 keV, as seen from Figure 2.8. Due to absorption on iodine the ARF shows a dip at 35 keV.

In the beginning of march 1996, two month after launch, the pulse height analyzer of scintillator #3 of cluster B failed. Since then only three of four scintillators can be used in scientific analyses. In January 2006 the rocking of cluster A failed due to a problem in the software controlling the cluster motion. After rebooting the software rocking resumed, but the problem arises again nearly every couple of days. The prevent the cluster to be

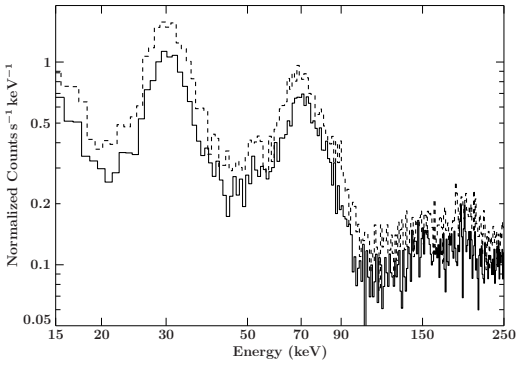

Figure 2.7: The background of HEXTE A (dashed) and HEXTE B (solid). Although the detectors are identical, the background of cluster A is slightly higher than for cluster B, which has only three instead of four scintillators working. Both backgrounds show strong emission lines around 30, 60 and 190 keV, which are all caused by iodine isotopes.

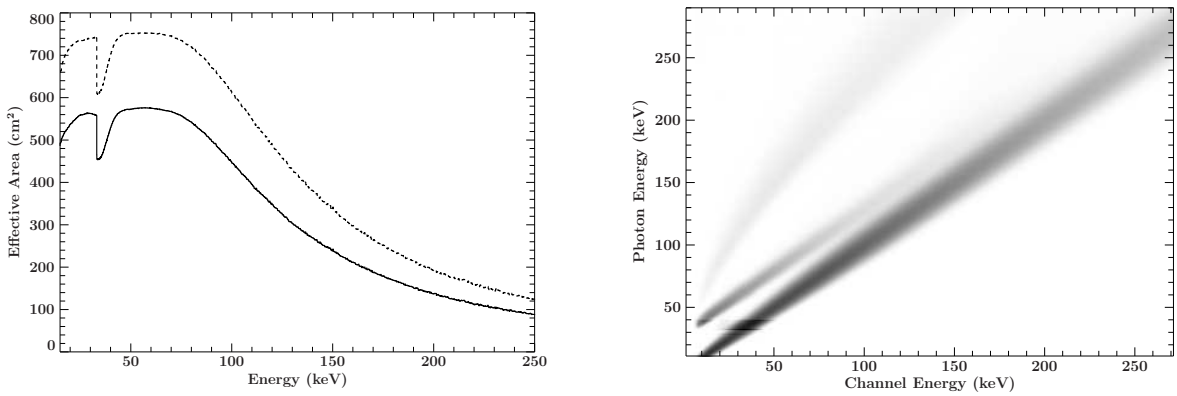

Figure 2.8: Left: the effective area of HEXTE cluster A and B shown as dashed and solid line, respectively. The ARF of cluster A is 4/3 higher than of cluster B due to four compared to three working scintillators. Besides a gap around 35 keV caused by absorption on iodine, the area is nearly constant between 25 and 70 ekV. It then drops to by a factor of 5-6 at 250 keV. Right: The RMF of HEXTE B shows a nearly linear correlation as well as two escape peaks. The absorption on iodine leads to the structure at ∼35 keV incident photon energy.

unrecoverable in one of the background positions the decision was made to fix this cluster in on-source position. In consequence no background for Cluster exists since October 2006.

2.3 Swift

The *Swift* satellite, launched in November 2004, is a multi-wavelength observatory. It consists of the X-ray telescope (XRT), the *UV/Optical Telescope* (UVOT) and the *Burst Alert Telescope* (BAT). The UVOT and the BAT are not discussed here any further, because they are not used within this thesis. An overview and more informations about the instruments can be found in the *Swift* documentation.[4]

The XRT creates an image of an observed X-ray source. That means the X-rays have to be focused. To focus an incident X-ray beam, several cone shaped gold foils are aligned concentrically around the line of sight of the telescope. An X-ray photon entering the telescope at a small angle to the line of sight is total reflected on the gold foils and redirected onto the CCD, where it gets detected. Such a telescope is called *Wolter telescope*.

A CCD is made of a two dimensional array of photo diodes. Each diode is a photon detector made of a pn-endowed silicon crystal, called *pixel*. An incident photon induces free electrons, which are collected in a potential well. After some collecting time Δt each pixel in a row is shifted step by step to the read out electronics, which is located at the edge of the CCD. There the electron current is detected, which is proportional to the incident photon energy. It might happen that more than one photon induce electrons in a pixel if the collecting time Δt is long enough relative to the actual count rate $r(t)$:

$$\Delta t \cdot r(t) > 1 \tag{2.3}$$

In that case the detected energy is the sum of the photons. Since the number of photons cannot be counted by a CCD, the energy is associated to a single photon. This so-called *pile-up* yields to incorrect measured spectra and count rates. This effect has to be taken into account during the data extraction and analysis.

[4] see http://swift.gsfc.nasa.gov/docs/swift/about_swift/

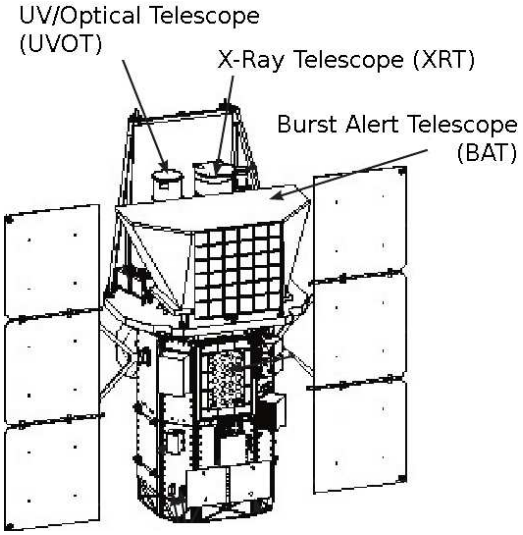

Figure 2.9: A schematic overview of the *Swift* satellite. The three different detecors XRT, UVOT and BAT are labeled (taken and modified from the *Swift* Press kit[4]).

The advantage of using CCDs to observe X-ray sources is the imaging capability. The background spectrum for an observed source is measured simultaneously to the source spectrum on a different region of the CCD. By selecting these regions during the extraction process a better signal to noise ratio can be achieved than, e.g., by using scintillators or proportional counters.

The sensitive energy range of the XRT mounted on *Swift* is between 0.3 and 10 keV. Due to the focal length of the telescope of 3.5 m the field of view of the XRT is 23.6 arcmin. The CCD consists of 600x600 pixels and its effective area is 110 cm^2 at 1.5 keV.

2.4 Suzaku

Suzaku is a Japanese satellite built in association with the NASA and launched in July 2005. Due to four different X-ray detectors onboard, the sensitive energy range of all instruments combined is 0.3 to 600 keV. Because the detection principles of these instruments are similar to the ones discussed in the previous Sections 2.2 and 2.3, only a short description is given in the following. Details can be found in the *Suzaku* technical description[5].

Four *X-ray Telescopes* (XRTs) focus incident X-rays onto a single CCD each. Due to the imaging capability these four instruments are named *X-ray Imaging Spectrometer* and labeled XIS0 to XIS3. The effective area of each CCD is about 400 cm^{-2} at 1.5 keV and the sensitive energy range is 0.3 to 12 keV. The field of view of 19 arcmin is smaller than that of the *Swift*-XRT. The XIS2 and XIS0 were damaged by micro meteorites in 2006 and 2009, respectively. Hence data from these instruments are no longer available. The XIS1 has a higher background compared to the other XISs.

The fifth XRT is focused on the *X-Ray Spectrometer* (XRS). This is a high resolution microcalorimeter with an energy range of 0.2 to 10 keV. Unfortunately, this instrument failed shortly after launch and is therefore not discussed here.

The last detector onboard *Suzaku* was designed to detect hard X-rays between 10 and 600 keV. This *Hard X-ray detector* (HXD) is in principle a scintillator with a collimator, which limits the field of view to 0.56 degrees, on top. Below the scintillator crystal, photo multipliers are used to amplify and detect the signal. The scintillator detector is called GSO and is sensitive to energies above 50 keV and up to 600 keV. Between the crystal and the collimator two arrays of PIN diodes are placed, which detect X-rays between 10

[5]see http://heasarc.nasa.gov/docs/suzaku/prop_tools/suzaku_td/suzaku_td.html

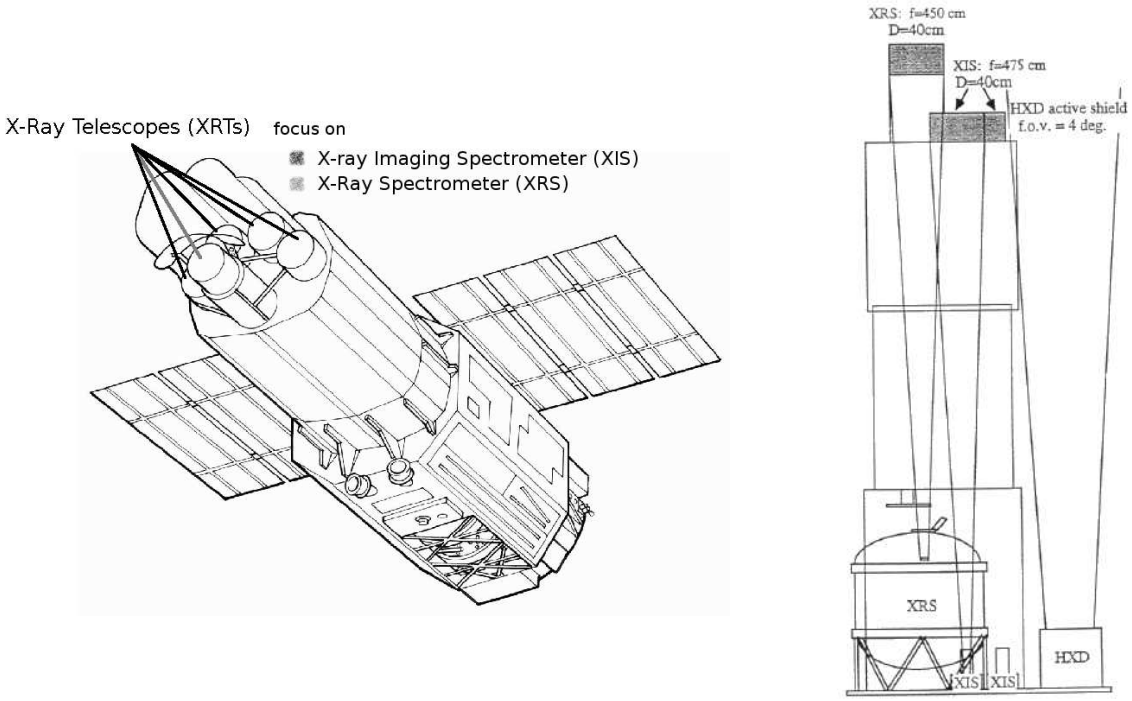

Figure 2.10: Left: The *Suzaku* satellite as schematic overview. The five X-ray telescopes (XRTs) focus the incident X-rays onto the four X-ray Imaging Spectrometer (XISs, black line) and the X-Ray Spectrometer (XRS, gray line). Right: A schematic sideview of the satellite with the three instruments XIS (four times), the XRS and the Hard X-ray Detector (HXD). The XRTs are implied. Both images are taken and modified from the *Suzaku* technical description[5].

and 50 keV. The effective areas of the PIN diodes and the GSO are 160 cm^{-2} at 15 keV and 300 cm^{-2} at 120 keV, respectively.

Chapter 3
X-ray Pulsar Orbit Determination

Knowing the orbital parameters of an X-ray binary is essential for studying the accretion mechanism. For example, as discussed in Section 1.2.3, the change of the spin period of the neutron star is connected to the mass accretion rate. Furthermore, knowing the pulse profile is important to study the emission geometry, which might change during the mass transfer. To analyze these properties, the pulse period, P, of the neutron star in its frame of rest has to be known. Due to the orbital motion of the binary system and the motion of the used satellite in the Solar system, however, the observer measures a Doppler shifted period,

$$P_{\mathrm{obs}} = P \cdot (1 - v/c) \tag{3.1}$$

where v is the velocity in direction to the observer and c the speed of light. As a consequence the measured periods must be corrected for these effects. The orbits of the satellite and the Earth are usually well known, but the orbital parameters of the binary have to be determined by analyzing the pulse period of the neutron star. Since $v/c \ll 1$ the measurement of the pulse period has to be accurate enough to detect any changes. The corresponding analysis methods are described in this Chapter.

3.1 Epoch Folding

An often used method for determining the pulse period of an X-ray pulsar is called *epoch folding* (Leahy et al., 1983; Schwarzenberg-Czerny, 1989). It is based on folding the data on an assumed test period P_{test} and distribute the events into phase bins. First, the time is converted into pulse phase by

$$\phi = \frac{t \bmod P_{\mathrm{test}}}{P_{\mathrm{test}}} \tag{3.2}$$

Then a histogram H of the events or count rates R is created according to the pulse phases. For a given number of pulse phase bins, n, the histogram is calculated such that

$$H_i = \frac{P_{\mathrm{test}}}{T} \sum R(i/n \leq \phi < (i+1)/n) \tag{3.3}$$

where T is the length of the lightcurve and i is the index of the pulse phase bin, ranging from 0 to $n-1$. The normalization factor T/P_{test} is simply the number of pulses covered by the observation. The result is the mean count rate per phase bin. If the test period P_{test} equals to the pulse period of the pulsar at the time of the observation the histogram equals to the *pulse profile* (see Section 1.2.3). If the periods are not equal, however, the profile gets "washed" out as during the histogram calculation different real phase bins are summed up due to the wrong assumed phase bins. If the difference of the periods or the length of the observation is large, the falsely added phase bins average to a constant count rate as illustrated in Figure 3.1.

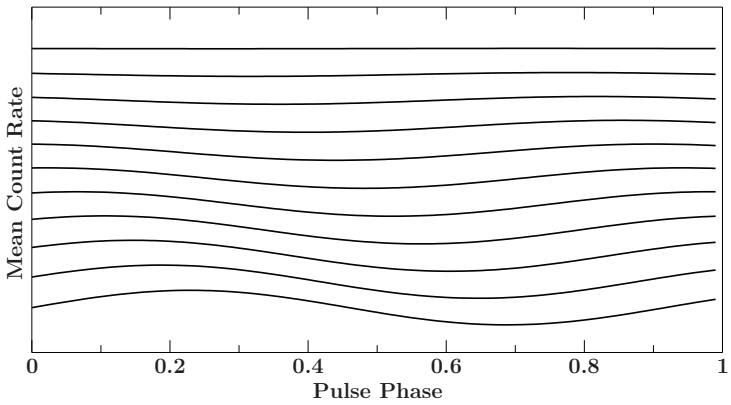

Figure 3.1: Folding of a sinusoidal pulse on a test period, which is shifted by 9% to the correct one. The result after each additional pulse is shown with 1 pulse at the bottom and 11 at the top. The upward shift is for display only.

To search for a period in the data the resulting average count rate per bin is tested against a constant using χ^2 statistics:

$$\chi^2 = \sum_{i=1}^{n} \frac{(R_i - \langle R \rangle)^2}{\sigma_i^2} \tag{3.4}$$

Here, if poission statistics are assumed, $\langle R \rangle$ is the mean count rate of the profile and $\sigma_i^2 = \langle R \rangle / T_i$ with T_i the integration time of the actual phase bin. To find the correct pulse period a wide range of test periods P_{test} is used, resulting in a distribution of χ^2-values. Its maximum is located at $P_{\text{test}} = P$, where the folded count rate per bin is equal to the pulse profile and therefore, of course, not constant. On the other hand, the χ^2-value is near zero if the test period significantly differs from the pulse period. However, test periods near the pulse period also lead to a high χ^2-value due to the finite observation time T and the noise. The distribution is therefore broadened and can have a quite complicated form. If a clear pulsation is present and the signal to noise ratio is high, the general form will however be like a gaussian. Besides the main peak additional maxima occur due to the finite length of the lightcurve. If the length of the lightcurve increases, these maxima move closer to the main peak (see left panel of Figure 3.2). For an infinite lightcurve the distribution converges to a delta distribution.

An advantage of the epoch folding technique is its ability tho handle gaps in the lightcurve. These gaps can, for example, be caused by the occultation of the source by the Earth. Nevertheless, it is not required to split the lightcurve at these gaps and to analyze each part seperately. These gaps might increase the additional smaller maxima around the main peak, however, if the test period is a multiple of the gap length, which is called windowing.In that case, one or more pulses are missing in the data, while the observed ones are folded on approximately the same period, leading to a non-constant profile. In other words, the additional phase shifts of the missing pulses are not added to the average profile. In consequence, if the test period leads to one additional or rather one missing pulse in the gap, a higher maximum occurs on each side of the main peak (see right panel of Figure 3.2).

The difference between two statistically independent periods P and P' is a measure for the accuracy of epoch folding. It is calculated by the change of the pulse period, if the number of pulses n in a lightcurve of length T differs by one:

$$\Delta P = |P - P'| = \frac{T}{n} - \frac{T}{n+1} = \frac{T}{n(n+1)} \tag{3.5}$$

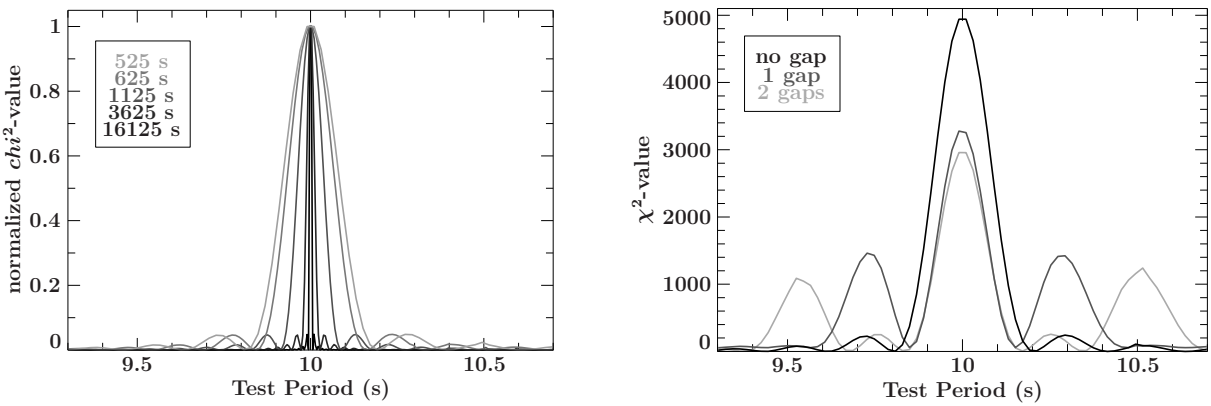

Figure 3.2: Dependence of the result of epoch folding from the length of the lightcurve (left panel) and gaps (right panel). If the number of gaps increases, the secondary maxima increase while the main peak decreases. In addition, the distances of the maxima to the main peak increase. If the length of the observation grows, the secondary maxima get closer to the main peak, which itself gets sharper.

The number of pulses is approximately $n = T/P$, which finally leads to

$$\Delta P \approx \frac{P^2}{T} \tag{3.6}$$

Hence the accuracy does not depend on the binning of the lightcurve as in Fourier techniques and can be increased by simply merging several lightcurves or using longer observations. However, if the pulse period changes during an observation, the pulse period derived by epoch folding might be uncertain. In general, the above uncertainty might be overestimated for sinusodial pulse shapes as shown by Leahy (1987).

For complex profiles, which are the common case in astrophysics, the uncertainty has to be estimated by Monte Carlo simulations: many synthetic lightcurves are created using the determined pulse profile and randomized according to the measured noise. In the next step the pulse period is determined by epoch folding in each synthetic lightcurve individually. For thousands of synthetic lightcurves this approach leads to normal distributed pulse periods. The resulting standard deviation of the distribution can be used as the uncertainty of the found pulse period.

3.2 Phase Connection

Determining any changes of the pulse period by epoch folding might fail if the change is below the accuracy, e.g., $\dot{P} \sim 10^{-8}\,\mathrm{s\,s^{-1}}$, as described by equation 3.6. Nevertheless a more sophisticated way exists, which uses the phase shifts between pulse profiles to resolve the pulse ephemeris, called the *phase connection* method (Manchester & Taylor, 1977; Deeter et al., 1981). This approach requires at least two observations, whose seperation is much larger than the pulse period. In the case that the pulse period change is much smaller than the separation of the lightcurves, the pulse period of both lightcurves is equal within the uncertainties. However, the pulse phase of the profiles might be shifted relative to a reference time t_0 in presence of non-zero time derivatives of the pulse period. The phase shift of two pulse profiles f and g of length n can be determined using the so called normalized discrete *cross-correlation*:

$$(f \star g)(\Delta x) = \sum_{x=1}^{n} \frac{f(x) - \bar{f}}{\sigma_f} \cdot \frac{g(x - \Delta x) - \bar{g}}{\sigma_g} \tag{3.7}$$

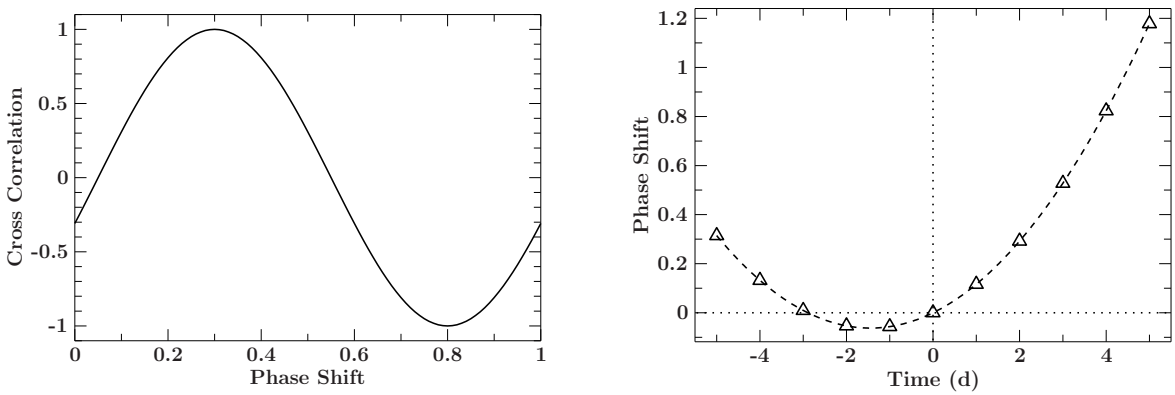

Figure 3.3: Left: determining the phase shift of two profiles by cross-correlation (see equation 3.7) results usually in one maximum and minimum respectively. Here two sinusoidal profiles with a phase shift of 0.3 are simulated. If the phase shifts between all observations are found, a fit of their time dependence to equation 3.8 reveals a more accurate pulse period and its derivatives. Right: the phase shifts of the pulse profile over time. Here the pulse period is affected by $\dot{P}_0 \neq 0$, which results in a parabola shape, and P_{obs} is not equal to P_0, leading to a shift of the turning point of this parabola.

Here Δx is the assumed phase shift between the two profiles, $\bar{f}$ and $\bar{g}$ the mean values and σ_f and σ_g the standard deviations, respectively. By definition the values of the cross-correlation function range between -1 and $+1$ and the larger the value the better both profiles match. As a consequence, the cross-correlation has a maximum where both profiles match best and the corresponding phase shift is equal to the real phase shift between both profiles (see left panel of Figure 3.3). However, further maxima might occur, for example, if the profile is double peaked.

Once all phase shifts between each observation and the reference one are determined, their time dependence can be described by a Taylor expansion of the pulse phase $\phi(t)$, leading to (Hilditch, 2001)

$$\Delta\phi(t) = (f_0 - f_{\mathrm{obs}})(t - t_0) + \frac{1}{2}\dot{f}_0(t - t_0)^2 + \mathcal{O}(t^3) \tag{3.8}$$

Here $f_0 = 1/P_0$ is the pulse frequency and its first derivative $\dot{f}_0$ is $-\dot{P}_0/P_0$, both taken at the reference time t_0. The same t_0 was used as a reference time for each profile and should be choosen near the middle of all observations. The observed frequency $f_{\mathrm{obs}} = 1/P_{\mathrm{obs}}$ is connected to the period used to fold each lightcurve on. Hence, P_0 and its derivatives can be determined by a fit to Equation 3.8.

Phase connection leads to a higher accuracy of the determined pulse period than using only epoch folding. The reason is that the phase shift between the observations is used in addition. It is possible that the accuracy of the observed pulse period P_{obs} might be too low to cancel the first term of equation 3.8, i.e., a wrong f_{obs} is measured. As a result, the turning point of the time dependence of $\Delta\phi(t)$, which is in first order approximation a parabola, gets shifted along both axes (see right panel of Figure 3.3). Additionally it might be necessary to expand the equation to higher orders, if a non-parabolic shape of the phase shifts is observed and higher orders of the expansion of f become important.

3.3 Pulse Arrival Times

If the orbital parameter of an X-ray binary are uncertain or unknown, a measured change of the pulse period might partly result from the Doppler shift due to the orbital motion. Hence, the change might be by mistake interpreted as angular momentum transfer onto the neutron star. As described in the previous section the time derivatives of the pulse period, the pulse ephemeris, can be determined by phase connection. Unfortunately the lightcurves used in this method have to be corrected for orbital motion of the binary first. Therefore one cannot distinguish between a transfer of angular momentum and orbital effects. Determining the orbital parameters is more difficult in transient X-ray binaries, where the luminosity is above the detection limit only near the periastron. Therefore observations only cover a certain fraction of the orbital period, which in most cases ranges from 10 to 500 days. The observable outburst, on the other hand, only lasts hours to days.

In order to solve this problem a method, that allows a simultaneous determination of orbital parameters and the pulse ephemeris, is implemented within this thesis. This is done by analyzing individual pulse arrival times, which are defined as the times of the occurrence of a specific pattern in the lightcurve, e.g., the detected pulse profile (see, e.g., Kelley et al., 1980; Nagase, 1989; Staubert et al., 2009). If the lightcurves are not binary corrected, the measured times include both the orbital motion and the changes of the pulse period of the neutron star.

To determine the arrival times in a lightcurve a search pattern has to be created in the first step. An algorithm then uses this pattern to identify the individual pulses by cross-correlation (see Equation 3.7) and transforms the resulting phase shifts into time. The arrival times determined in this way are modelled by taking the pulse ephemeris and the Doppler shift, caused by the orbital motion, into account. The resulting solution, however, has to be used to again determine and model the arrival times. The reason is the transformation of the phase shift into time, where the actual pulse period is needed, and the complex superposition of both effects, the angular momentum transfer and the orbital motion. This iterative approach is successful if the solution does not change anymore, as illustrated in Figure 3.4. The determination and modeling of the pulse arrival times are described in detail in the following Section. The functions to solve these two basic problems are implemented for use in the *Interactive Spectral Interpretation System* (Houck & Denicola, 2000, *ISIS*). This software is also used to analyze the spectra of the X-ray source GRO J1008–57 presented in Chapter 4.

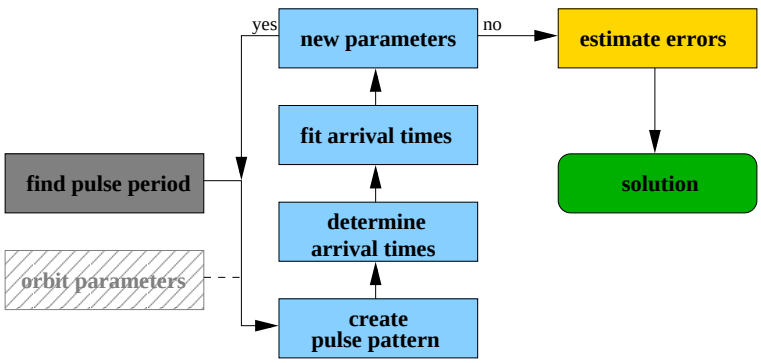

Figure 3.4: To obtain the correct solution of the arrival times analysis the determination and modeling must proceed iteratively. Starting from a constant pulse period, which is found, for example, by epoch folding, the pulse ephemeris and orbit parameter might change after each successful fit. In that case the determination of the arrival times and their analysis must be repeated and so on.

3.3.1 Determination

In order to detect the individual pulses in a lightcurve a pulse pattern has to be created. For example, this may be done by folding the lightcurve on the pulse period, which is found by a pulse period search using epoch folding. However, one has to assume that the change of the pulse period caused by the Doppler shift and angular momentum transfer during the observation is negligible. If this is not fulfilled a time shift arises caused by the change of the pulse period. The phase bins used to distribute the count rates in (see Section 3.1) get shifted as well. If this is not handled the distribution would be wrong and the profile would be smeared. Hence the resulting search pattern would be incorrect and incorrect phase shifts would be calculated.

The lightcurve near the middle should be used to create the pulse pattern for determining the arrival times of several lightcurves. In that case the errors due to the approximations of the arrival times function, which calculates the pulse arrival time of each pulse, are minimized. Additionally the reference time t_0 of the reference pulse number $n = 0$ is set (see Section 3.3.2).

To determine the arrival time of each pulse in a lightcurve, it is divided into segments of the length of the actual pulse period $P(t)$. From the maximum of a cross-correlation of a segment and the pulse pattern one obtains the phase shift $\Delta\varphi$ of each pulse to this pattern, which is then transformed into time by

$$t = t_i + \Delta\varphi \cdot P(t_0) \tag{3.9}$$

where t_i is the first time bin of the actual analyzed segment i of the lightcurve. In principle the determination of the pulse arrival times is based on phase connection. Nevertheless the transformation into time allows a simultaneous analysis of the orbital motion and the pulse ephemeris. However, the actual observed pulse period $P(t_0)$ used by this transformation is the aim of the following analysis and, in general, not known before. Hence the determination and analysis of pulse arrival times is an iterative method, which will be discussed later on. As a first approximation the pulse period can be assumed to be constant and may be set to the one used to create the pulse pattern.

The accuracy of the pulse arrival times is restricted to the binning of the lightcurve and therefore the binning of the pulse pattern. If the signal to noise ratio of the lightcurve is too low to determine the arrival times of individual pulses, it is possible to fold over a certain number k of pulses before computing the cross-correlation. Hence only every k^{th} arrival time is determined, but with a higher signal to noise ratio than for each individual pulse. It is also possible to average over all pulses of a lightcurve, which yields the arrival time of the pulse profile itself. In this case, it is assumed that any changes of the pulse period are small compared to the length of the lightcurve. In order to further increase the time resolution of the arrival times the binning of the cross-correlation of the pulse pattern and a certain pulse, which is equal to the binning of the pattern, can be increased by interpolation. This might fail, however, if the signal of the actual pulse is too low, resulting in a cross-correlation with more than one match.

If lightcurves from multiple detectors are recorded, the pulse pattern must be determined for each detector separately due to a different detector response (see Section 2.1). To ensure that the arrival times are comparable between the detectors a reference detector have to be choosen. It is recommend to use the detector with the longest time coverage to be able to choose the reference time t_0 adequately. The other pulse patterns then have to match the reference pattern to get the same phase shift during the determination of the arrival times. The alignment can be done by cross-correlation, for example (see Equation 3.7). However, the accuracy of this match is restricted to the binning of the

pattern. To handle this problem a further parameter of the fit routine, which is described later on (see Equation 3.17), allows to add a constant phase shift to the arrival times of each detector.

The uncertainty of an arrival time is related to the number of bins n of the pulse pattern and the actual pulse period $P(t)$:

$$\delta t = P(t)/n \tag{3.10}$$

However, this value might be overestimated if the signal quality is high enough to get unambiguous results from the cross-correlation. One way to estimate the uncertainty in a more accurate way is to perform Monte Carlo simulations. In those simulations random noise, which is based on Poisson statistics, is added to the lightcurve. A cross-correlation with the pulse pattern then yields a slightly different result. By repeating this simulation the standard deviation $S_{\Delta\varphi}$ of the resulting phase connection distribution converges after a certain number of simulations. The uncertainty of the arrival times then is

$$\delta t = S_{\Delta\varphi} \cdot P(t) \tag{3.11}$$

It turned out during the analysis of pulse arrival times (see Chapter 4) that the uncertainties are slightly underestimated by Monte Carlo simulations if individual pulse arrival times are determined. The simulations work well for arrival times of entirely folded lightcurves only. Therefore a third way of estimating the uncertainties of individual pulse arrival times is to used: the local standard deviation of the determined arrival times. If the change of the pulse period $P(t)$ during k pulses is small, the time difference between each pulse should be exactly the pulse period. Due to measurement and statistical errors these differences scatter around the pulse period and their standard deviation $S_{\Delta t}$ can be used to describe the uncertainties of k pulse arrival times by

$$\delta t = S_{\Delta t} \tag{3.12}$$

The number of pulses k depends on the observed X-ray source and can be estimated, e.g., by simulations.

3.3.2 Simulation

After determining the arrival times of one or more lightcurves they can be analyzed with a model which includes the Doppler shift due to orbital motion of the binary and the pulse ephemeris of the neutron star. The pulse pattern used to determine the arrival times defines the reference pulse number $n = 0$ at time t_0, which is used to fold the lightcurve on. The observed arrival time $t_{\mathrm{obs}}(n)$ of the n^{th} pulse is given by

$$t_{\mathrm{obs}}(n) = t_{\mathrm{emit}}(n) + \frac{z(t_{\mathrm{emit}}(n))}{c} \tag{3.13}$$

Here $t_{\mathrm{emit}}(n)$ is the time when the pulse of number n is emitted in the barycenter of the binary. This time is shifted by orbital motion, which depends on the position z of the neutron star. This position is calculated by the projection of the position vector $\vec{r}(t)$ of the neutron star in the barycenter of the binary and the unity vector $\vec{e}_{\mathrm{los}}$ in direction of the line of sight. For $z < 0$ the neutron star is closer to Earth by definition. To perform this calculation the position of the neutron star in the binary system has to be known at each time. The mathematical description of the orbit requires the definition of the following orbital parameters (compare Figure 3.5):

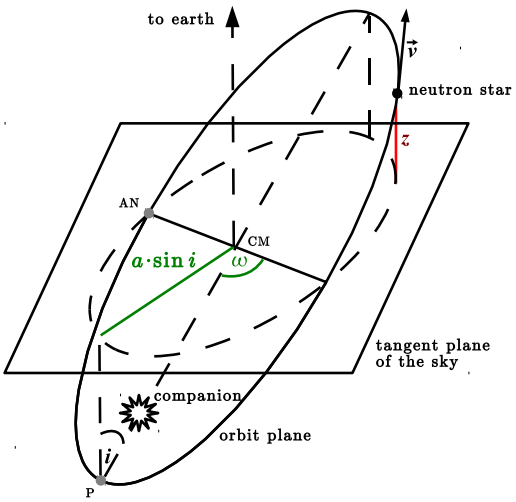

Figure 3.5: The elliptical orbit of a neutron star around the center of mass (CM) in a transient X-ray binary. If the neutron star is close the periastron (P), usually an outburst in X-rays occurs. The orbital parameters $a \sin i$ and ω are shown as well as the z-position of the neutron star, which is needed to calculate the Doppler shift contribution to the arrival times. At the ascending node (AN) the projected velocity away from Earth is at its maximum.

P_{orb}	orbital period of the neutron star
$a \sin i$	projected semi major axis, the largest distance between the neutron star and the center of mass of the binary as seen from Earth
e	eccentricity of the orbit, where $e = 0$ means a perfect circle and $e = 1$ a parabola
ω	angle between the periastron and the ascending node, where the velocity away from Earth is maximal
τ	time of a periastron passage

These parameters are used to obtain the angular position E of the neutron star, which is called eccentric anomaly. It is calculated by solving Kepler's equation

$$\frac{2\pi(t-\tau)}{P_{\text{orb}}} = E - e \cdot \sin E \tag{3.14}$$

The identity on the left of Equation 3.14 is also known as the mean anomaly M. Once the eccentric anomaly E is found, the projection of the position vector of the neutron star is finally calculated by (Hilditch, 2001)

$$z = a \sin i \cdot \left(\sin\omega \cdot (\cos E - e) + \cos\omega \sin E \cdot \sqrt{(1-e)\cdot(1+e)} \right) \tag{3.15}$$

Details about Kepler's equation and its numerical solution can be found in, e.g., Hilditch (2001) or Mikkola (1987).

The emitting time $t_{\text{emit}}(n)$ of the pulse of number n up to the fourth order in n is given by

$$t_{\text{emit}}(n) = t_0 + Pn + \frac{1}{2}P\dot{P}n^2 + \frac{1}{6}(P^2\ddot{P} + P\dot{P}^2)n^3 + \frac{1}{24}(P^3\dddot{P} + 4P^2\dot{P}\ddot{P} + P\dot{P}^3)n^4 \tag{3.16}$$

and can be calculated by a Taylor expansion of the emitting times $t_{\text{emit}}(n)$ and the pulse phase $\phi(t)$, which is used to substitute the pulse number n. The detailed calculation is given in Appendix A.

As mentioned in section 3.3.1 if multiple patterns are used, e.g., because of different detectors, their alignment might not be accurate enough. In that case a constant phase shift $\Delta\phi$ may be added, modifying equation 3.13 to

$$t_{\text{obs}}(n) = t_{\text{emit}}(n) + \frac{z(t_{\text{emit}}(n))}{c} + \Delta\phi \cdot P(t) \tag{3.17}$$

Table 3.1: Parameter of the arrival times fit function. The list is divided into the parameters of the approximated pulse ephemeris (see equation 3.18) and the orbit.

	Parameter	Unit	Description
ephemeris	P	s	pulse period in the neutron star rest frame at t_0
	$\dot{P}$	s/s	first derivative of the pulse period at t_0
	$\ddot{P}$	s/s^2	second derivative of the pulse period at t_0
	$\dddot{P}$	s/s^3	third derivative of the pulse period at t_0
	$\Delta\phi$		constant phase shift, used to handle different pulse patterns
orbit	P_{orb}	d	orbital period
	$a \sin i$	l-ts	projected semi major axis
	e		eccentricity
	ω	degrees	angle of ascending node
	τ	MJD	time of periastron passage

According to the order of equation 3.16 the pulse period here is (compare to Equation 1.16)

$$P(t) = P + \dot{P}t + \frac{1}{2}\ddot{P}t^2 + \frac{1}{6}\dddot{P}t^3 \tag{3.18}$$

Usually the additional phase shift in Equation 3.17 should be less than the binsize of the pattern. If this is not the case several possible reasons have to be considered: the alignment could already have failed during the determination of the arrival times or the phase shift could be highly correlated with one of the other fit parameters. These parameters are summarized in Table 3.1.

The χ^2 minimization algorithm calls a fit function, which calculates the arrival times according to equation 3.17 and the given parameters for the orbit and the pulse ephemeris. Therefore the pulse number n is needed, which cannot be measured. Hence the fit function has to determine the pulse number by solving equation 3.17 for the given observed arrival times first. The only known pulse number is by definition $n = 0$ at the reference pulse t_0. Because of the fourth order polynomial for the emitting time $t_{\mathrm{emit}}(n)$ and the Doppler shift, which is calculated using trigonometric functions, the solution has to be found numerically. The position of the neutron star $z(t_{\mathrm{emit}}(n))$ on its orbit must be considered as well. Unfortunately it depends on the unknown emission time $t_{\mathrm{emit}}(n)$, which itself depends on the pulse number that has to be found. Hence the pulse number must be found iteratively by assuming $t_{\mathrm{emit}}(n) = t_{\mathrm{obs}}(n)$ for the orbital position first. Subsequently the found pulse number n, at this point a floating point number, is used to calculate a new emission time and in the following an updated z position. This iterative calculation converges usually after a few steps, since the neutron star's change in position is small compared to the pulse period:

$$\frac{1}{c}\left|z(t_{\mathrm{emit}}(n+1)) - z(t_{\mathrm{emit}}(n))\right| \ll t_{\mathrm{emit}}(n+1) - t_{\mathrm{emit}}(n) \approx P(t)$$

The found pulse number is then transformed into an integer number and used to simulate the corresponing arrival time using equation 3.17. This time is returned to the χ^2 minimization algorithm and compared with the observed arrival time. However, the numerical determination of the pulse number might result in a wrong value. This happens basically in two cases:

1. First uncertain orbital or pulse ephemeris parameters might result in an additional time shift in the order of the pulse period. In consequence the pulse number is shifted by several pulses. This problem can be fixed by a detailed analysis of the χ^2-distribution of the uncertain parameter. Near the correct value the pulse numbers

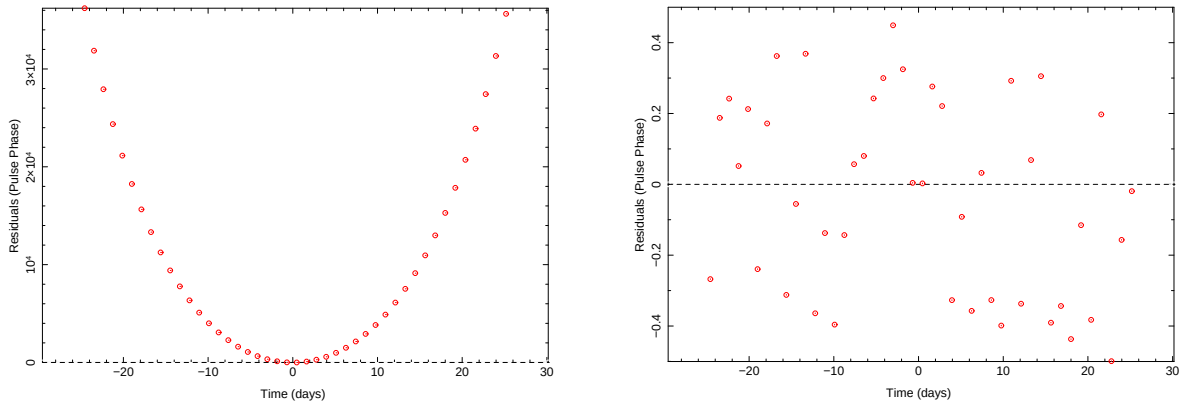

Figure 3.6: Impact of the relative pulse numbers on the residuals. Pulse arrival times are simulated with a changing pulse period of $\dot{P}/P = 10^{-6}\mathrm{s/s}^2$ over several days. The model, however, only uses a constant pulse period. Relative pulse numbers are used in the fit shown on the left panel and a clear parabola shape can be seen as expected due to the fact that the arrival times scale like n^2 with $\dot{P} \neq 0$. If relative pulse numbers are not used, the residuals on the right panel seems to be randomly scatterd. This results from a wrongly calculated pulse number caused by the large value of $\dot{P}/P$, which is not fitted

are no longer misleadingly shifted, which can be recognized as a sudden jump in the χ^2-distribution. Another possibility to avoid this problem for pulses near the reference time t_0 is to calculate the pulse numbers in a more proper way, which is described in the next paragraph.

2. The second case occurs if the contribution of the neglected higher order terms in equation 3.16 is in the order of the pulse period. This happens usually if the time difference between the pulses and the reference time t_0 is in the same order as the higher order coefficients. Then the function is no longer able to describe the arrival times. The two solutions of this problem are either to include higher order terms or to decrease the time difference by moving the reference time t_0. Therefore, it might be necessary to determine the arrival times with two or more reference times, that means to divide the dataset into several parts with an own pulse pattern each. This would lead to two different pulse ephemerides but the same orbital parameters.

To increase the calculation speed relative pulse numbers are used. Based on the first measured pulse in a lightcurve the pulse number of the next k^{th} detected one is

$$n_k = n_0 + k$$

where n_0 is the pulse number of the first pulse, which has to be found numerically. If this pulse number is found, the numbers of the following pulses are set as well. For example, the runtime of determining the pulse numbers of 100 simulated pulses decreases by a factor of 20 using relative pulse numbers. This approach solves the second kind of wrong pulse number calculation introduced above. If the pulses are near the reference time t_0 and one or more model parameter are uncertain, the pulse numbers are no longer shifted if the first pulse number of the lightcurve is found correctly. In most cases the first pulse number is equal or near zero if the lightcurve is used for defining the pulse pattern. The impact of different pulse numbers on the residuals is shown in Figure 3.6. The relative pulse numbers do not work for lightcurves, which are separated by several days, however. In that case many pulses are not observed and, if the pulse period is affected by a strong Doppler shift or change in pulse period, the relative pulse number k can be only guessed.

As mentioned in the introduction section to pulse arrival times (see section 3.3), the

determination and analysis have to be repeated if the arrival times are modelled successfully. The reason therefore lies in the transformation of the phase shift between the pulse pattern and each found pulse into time (see equation 3.9). There the pulse period depends on time, of course, and therefore on the pulse ephemeris, which is taken from the first fit of the arrival times. Hence, the determined arrival times will change after determining the ephemeris again. The difference is stronger with increasing distance to the reference time t_0 since higher order terms contribute more. Furthermore, the pulse profile is affected by the pulse ephemeris and has to be considered. The same applies for the orbital solution. Therefore, the lightcurves must be corrected for orbital motion to create the pulse pattern. Of course the not corrected lightcurves must be used for the arrival times determination. All in all, this results in an iterative analysis of determining and modeling the arrival times until the found parameters do not change significantly anymore.

3.3.3 Accuracy

By simulating arrival times with randomly generated parameters for pulse ephemeris and orbit the fit function can be checked for errors. If the parameters during a fit are fixed to the ones used to simulate the data, the resulting model should perfectly match the arrival times. The resulting reduced χ^2 value should be exactly zero, if statistical and systematic errors, which are present in a real measurement, are not simulated. However, the residuals of simulations do not vanish completely and increase dramatically for higher distances to the reference time t_0 (see left panel of Figure 3.7). This discrepancy is due to numerical restrictions: the terms of equation 3.16, which calculates the arrival time depending on the pulse number n, are arranged by orders of n. The coefficients are the derivatives of the pulse period, which cover a wide range of orders. For example the results for the pulse ephemeris parameter of the X-ray binary GRO J1008–57 (see Section 4) cover 14 orders of magnitude. By adding these terms of different orders of magnitude the numeric is not able to handle those numbers due to a restricted precision: the relative precision of *ISIS* is $\approx 2.3 \cdot 10^{-16}$ for example. In order to avoid this problem the polynomials are rearranged according to the *Horner scheme* (Horner, 1819), i.e. mathematical operations are always performed on the lower order. Accordingly, the equations for the calculation of the pulse emitting time (3.16) and the pulse period (3.18) are rearranged to

$$t_{\mathrm{emit}}(n) = \left(\left(\left(\frac{1}{24}(P^3\dddot{P} + 4P^2\dot{P}\ddot{P} + P\dot{P}^3)n + \frac{1}{6}(P^2\ddot{P} + P\dot{P}^2)\right)n + \frac{1}{2}P\dot{P}\right)n + P\right)n + t_0 \tag{3.19}$$

$$P(t) = \left(\left(\frac{1}{6}\dddot{P}t + \frac{1}{2}\ddot{P}\right)t + \dot{P}\right)t + P \tag{3.20}$$

In addition the runtime is further increased by factoring out the pulse number n, which reduces the number of operations. By performing the same simulation as above, the reduced χ^2 value drops by three orders of magnitude when using the rearranged polynomials (see right panel of Figure 3.7). After 10 days the relative accuracy of the arrival times fit function is higher than 10^{-5}. That means for a pulse period of, e.g., 1 s the simulated arrival times 10 days after the reference time t_0 are accurate within 10 μs. This is far below the resolution of any present-day detector.

To check whether the fit function leads to correct parameters, Monte Carlo simulations, which simulate arrival times of a randomly generated orbit and pulse ephemeris, are performed. To take the detector resolution into account normal distributed noise is added to the arrival times. The uncertainties of the simulated arrival times are set to the 1σ noise level. If the model parameters of the fit function are set to the initial parameters of

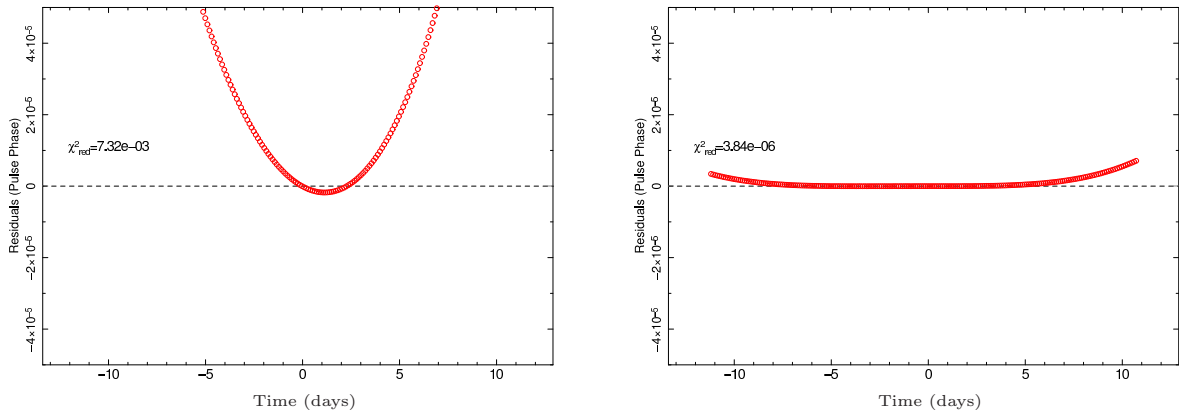

Figure 3.7: Left: using the pulse ephemeris as defined in equation 3.16 leads to discrepancies to a perfect fit due to the restriction of numerical precision. Right: by arranging the terms of the polynomial following the Horner scheme as shown in equation 3.19 the precision can be increased. The χ^2_{red} value is reduced by three orders of magnitude.

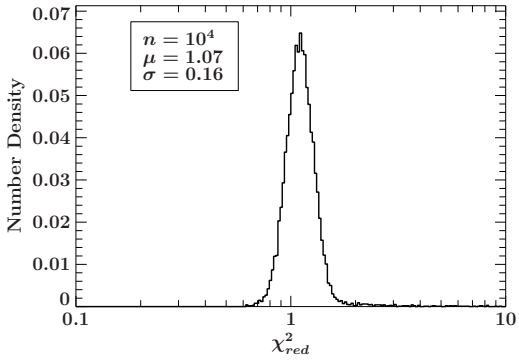

Figure 3.8: χ^2 distribution resulting from the Monte Carlo simulations of generated arrival times wih random parameters. As expected the values are Gaussian distributed. The x-axis is scaled logarithmically for clarity.

the simluation, evaluating the fit function should lead to a reduced χ^2 value of about one. On the other hand any errors in the fit function should affect the resulting χ^2 distribution. But the distribution of 10,000 simulations shown in Figure 3.8 does not show any evidence for such errors. With a mean value $\mu = 1.07$ and a width of $\sigma = 0.16$ the χ^2 values are Gaussian distributed.

Hence, judging from the analysis of the fit function's accuracy and χ^2 distribution, the function can be used to determine and model pulse arrival times. Including further supporting functions, like saving the arrival times into a FITS-file or plotting the residuals of the model, the source code provides 25 functions. They are available via a collection package and can be used on the computers at the Remeis observatory[1]. They can be used also by all users of *ISIS*, who download and include this package.

3.4 XTE J1946+274 and GX 304–1

The transient X-ray binaries XTE J1946+274 and GX 304–1 underwent outbursts in November and December 2010, respectively. Both systems contain a neutron star on an eccentric orbit around a Be type companion. For each source the arrival times algorithm was used to determine the pulse period and its change. The results are in agreement with analyses by Fermi/GBM (M. Finger et al., priv. comm.) and demonstrate the functionality of the implemented algorithms. The found pulse period ephemerides contribute to a long-term project to study accreting pulsars, conducted by a longstanding international collaboration ("Magnet" collaboration) (Müller et al., 2010; Kühnel et al.,

[1] http://www.sternwarte.uni-erlangen.de/git.public/?p=isisscripts

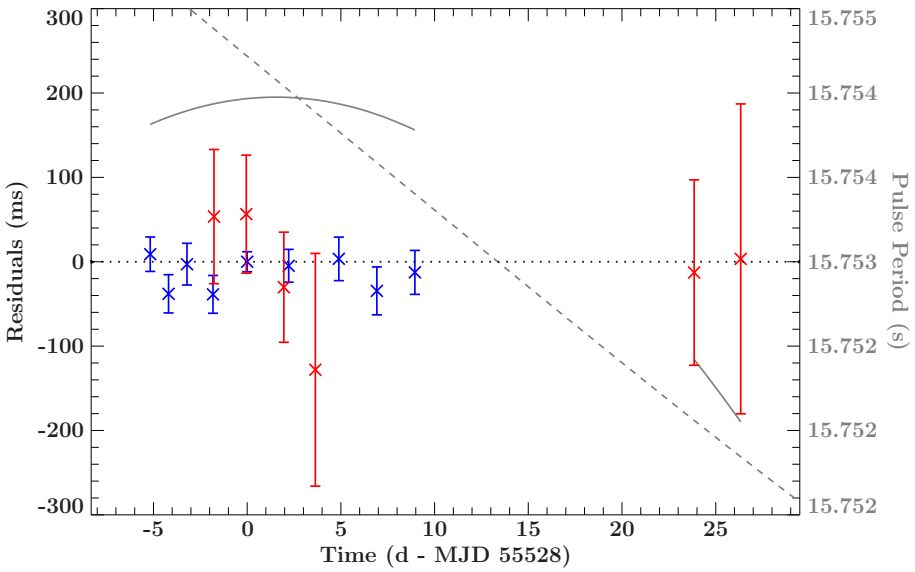

Figure 3.9: The residuals of a fit to the determined arrival times of the November 2010 outburst of XTE J1946+274. The used lightcurves were measured by *RXTE* (blue) and *Swift* (red). The data are modelled without taking any orbital effects into account. The resulting pulse ephemeris (solid gray line) hence includes the Doppler shift by orbital motion and any angular momentum transfer. The orbital Doppler shift expected from the parameters found by Wilson et al. (2003) is shown as the dashed gray line.

2010). A detailed analysis using arrival times is shown in Chapter 4 on the example of GRO J1008–57.

Since 2001 XTE J1946+274 did not show any activity, until a sequence of outbursts started in June 2010. The outbursts were separated by half of the orbital period of about 169 d (Wilson et al., 2003). In conclusion mass accretion appears at the periastron as well as at the apastron. This behavior is not fully understood yet. The 2010 November outburst was observed by *RXTE* and *Swift*. A pulse pattern for each detector is created from the lightcurves measured by *RXTE*-PCA and *Swift*-XRT assuming a constant pulse period, which is set to 15.754 s as found by the epoch folding method (see Section 3.1). Because of a low signal to noise ratio the lightcurves are folded and compared with the pulse pattern. In consequence, a single arrival time for each observation is determined instead of each pulse in the lightcurves. Due to large uncertainties, the existing orbital parameters found by Wilson et al. (2003) are not suitable to describe the observations. Therefore, the arrival times of the November outburst are fitted without taking any orbital effects into account. As a result, the pulse ephemeris includes orbital motion as well as angular momentum transfer. According to Figure 3.4 the iterative fit converged after 29 steps. However, the arrival times measured beyond 55543 MJD have to be fitted by different values of $\ddot{P}$ and $\dddot{P}$. The reason for this is that the pulse ephemeris calculated by a polynomial of third order (see Equation 1.16) cannot describe the complex Doppler shifted period due to orbital motion. The residuals of the best-fit are shown in Figure 3.9 and the fit parameters are listed in Table 3.2. The uncertainty of the determined pulse period is below 1 μs.

The second analyzed transient X-ray binary GX 304–1 underwent an outburst in December 2010, which was the seventh outburst after 28 years of quiescence. The strength of the outbursts are variable. They are separated by approximately 132.5 d, which might indicate the orbital period of the system. So far, further orbital parameters of the system are unknown. Some days before the December outburst reached its maximum, several less luminous flares were seen in the BAT lightcurve. These flares were also obsered with

Table 3.2: The fit parameters determined by a fit to the arrival times of XTE J1946+274. Orbital effects are neglected as described in the text. The last two *Swift* datapoints needed to be fitted by different values for $\ddot{P}$ and $\dddot{P}$.

	$t < 55543$	$t > 55543$
t_0	55528.36522 MJD	
P	15.7539668(6) s	
$\dot{P}$	$1.284(15) \times 10^{-10}\,\mathrm{s\,s^{-1}}$	
$\ddot{P}$	$-9.5(2) \times 10^{-16}\,\mathrm{s\,s^{-2}}$	$-8.52(2) \times 10^{-16}\,\mathrm{s\,s^{-2}}$
$\dddot{P}$	$6.3(8) \times 10^{-25}\,\mathrm{s\,s^{-3}}$	$-4.49(4) \times 10^{-25}\,\mathrm{s\,s^{-3}}$

Swift-XRT. The recorded lightcurves are analyzed by epoch folding first, resulting in a pulse period of about 275.29(6) s. Based on this value, a pulse pattern is created by folding the *Swift*-XRT lightcurves, and the arrival times for each lightcurve are determined. As in the analysis of XTE J1946+274, the single profiles are compared to the pattern resulting in one arrival time for each observation. Since no orbital parameters are known, the arrival times are fitted by the pulse ephemeris only. The pulse period is assumed to be constant to check on residuals due to orbital motion, which are supposed to dominate the observed pulse period at low luminosities (Equation 1.15). A constant pulse period does not require an iterative fit as illustrated in Figure 3.4. The fit reveals a pulse period of 275.3775(15) s for the first three arrival times between 55547.8 and 55551.1 MJD. Later arrival times are inconsistent with this pulse period and produce significant residuals as shown in Figure 3.10. The accuracy of the pulse period determined by arrival times analysis is higher by one order of magnitude.

The analysis of both sources shows that the algorithm for determining and modelling pulse arrival times is working. Further on, the results are accurate enough to study the effects of orbital motion and angular momentum transfer in greater detail than by using, e.g., epoch folding.

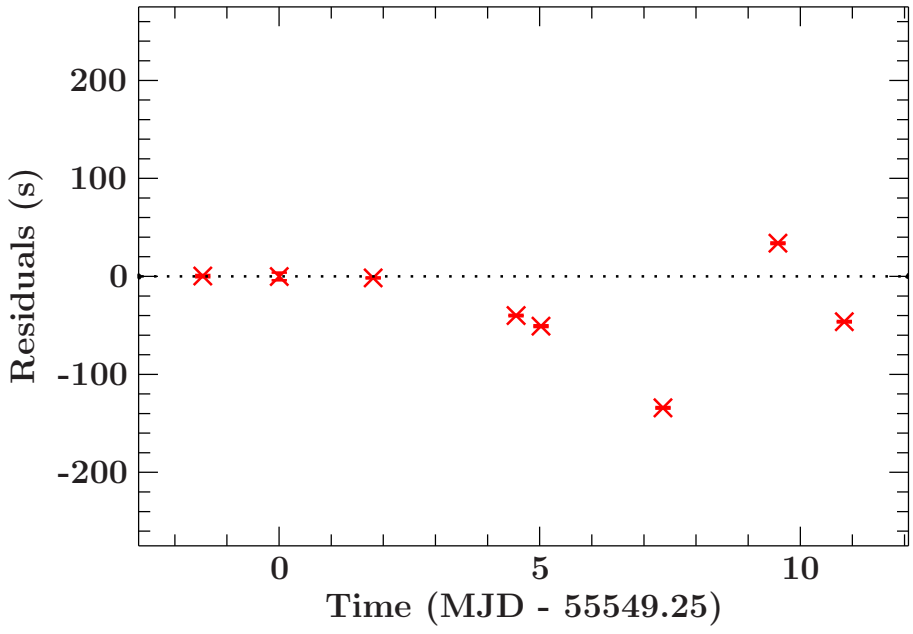

Figure 3.10: Residuals of a fit to the determined arrival times of the December 2010 outburst of GX 304–1. The arrival times are determined from lightcurves meassured by *Swift*-XRT. The residuals above 55558 MJD are shifted by one pulse period due to a wrong calculated pulse number (see Section 3.3.2).

Chapter 4

Analysis of GRO J1008–57

The transient X-ray binary GRO J1008–57 was discovered in 1993 by the BATSE detector onboard the *Compton Gamma Ray Observatory* (CGRO, Wilson et al., 1994; Stollberg et al., 1993). Similar to the ASM mounted on *RXTE* the goal of BATSE was to detect sudden changes in the X-ray map of the sky. GRO J1008–57 is considered to be a transient HMXB with a Be type companion (Coe et al., 1994). Due to the presence of X-ray pulsations with a period of 93.5 s, the compact object has to be a neutron star with a high magnetic field (Shrader et al., 1999, see also Section 1.2.3). A cyclotron line at 88 keV was claimed (Grove et al., 1995; Shrader et al., 1999), which would imply this neutron star to have one of the highest magnetic field strengths known for such systems. So far, the high energy cyclotron line could no be confirmed.

From observations of further outbursts, Coe et al. (2007) were able to determine the orbit parameters of the system, which are given in Table 4.1. The expected pulse period including the orbital Doppler shift is simulated in Figure 4.1. The so found orbital period of 247.8 d is in aggreement with the recurrence of the outbursts. The parameters are, however, not well constrained since GRO J1008–57 is only visible around the periastron for about 10 to 15 days. Hence observations of the system cover only a small fraction of the full orbit. Coe et al. (2007) also found a correlation of the luminosity of an outburst to the strength of optical Hα emission. The emission is associated with a circumstellar disc, which varies in size and defines the material available for accretion. From the optical spectra the size and mass of the companion could be determined to be $7\,R_\odot$ and $15\,M_\odot$. There is also evidence for an inclined circumstellar disc with respect to the orbital plane.

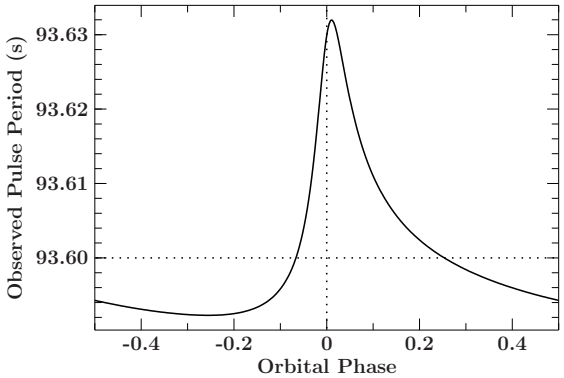

Figure 4.1: The Doppler shifted pulse period due to the binary motion as expected from the parameters found by Coe et al. (2007) (see Table 4.1). The orbital phase zero is defined as the time of the periastron passage τ. The unshifted pulse period here is 93.6 s.

Table 4.1: Orbital parameters of GRO J1008–57 as found by Coe et al. (2007). The uncertainties correspond to a 1σ confidence level.

P_{orb}	247.8(4) d
e	0.68(2)
$a \sin i$	530(60) lt-s
ω	-26(8)°
τ	49189.8(5) MJD

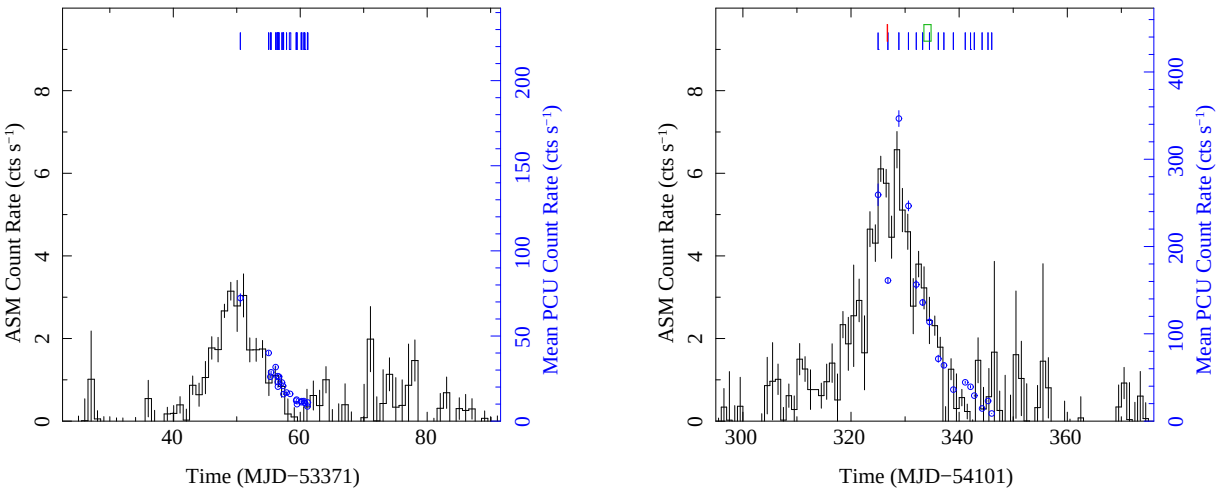

Figure 4.2: ASM lightcurves of the outbursts of GRO J1008–57 in 2005 (left) and 2007 (right). In addition the mean PCU count rate of the *RXTE* observations are overlayed for comparison. The times of pointed observations by *RXTE* (blue), *Swift* (red) and *Suzaku* (green) are indicated by boxes on top. The width of each box corresponds to the length of the observation.

4.1 Data Extraction

GRO J1008–57 was monitored by *RXTE* during two outbursts in February 2005 and December 2007. The latter outburst was also observed by *Swift* and *Suzaku*. The ASM lightcurves of GRO J1008–57 during these epoches are shown in Figure 4.2 including the times of individual observations by the satellites. A full list of the used observations and the numbering scheme can be found in Table C.1. The extraction of these observations is described in the following using the standard HEASARC software pipelines and tools.[1]

The spectra of all *RXTE* observations are extracted from the `standard2f` data mode, while for lightcurves the `GoodXenon` data mode is used. The latter allows a higher time resolution up to 1 μs. The lightcurves are transformed into the barycenter of the solar system by the pipeline and, afterwards, binned over 1 s in order to achieve a better signal to noise ratio. This time resolution is sufficient since the pulse period of GRO J1008–57 is $\sim$93.5 s is much larger. Further details about the available data modi can be found in the *RXTE* documentation, technical appendix F[2]. The data recorded from 10 minutes before to 10 minutes after SAA passages (see Section 2) are neglected to avoid any effects of high energy particles and activated detector material. Since PCU0 and PCU1 were hit by micro meteorites and PCU3 and PCU4 are affected by voltage problems (see Section 2.2.1) the data of PCU2 are used exclusively. In addition, the 2007 data of HEXTE A cannot be used for analysis since the instrument was fixed in on-source position in late 2006 (see Section 2.2.2). Hence no background for HEXTE A data exists for this time.

The data measured by *Swift*-XRT and the four *Suzaku*-XISs have to be extracted in a different way to *RXTE*. Both instruments are imaging spectrometers and the events which are to be extracted have to be selected as regions on the different CCDs. The image of GRO J1008–57 taken by *Swift*-XRT during the 2007 outburst and the extraction regions are shown in Figure 4.3. Two types of regions, drawn in different colors, are used to extract both the source (black) and background events (red). The latter are afterwards subtracted from the source spectrum. In addition, a small region around the source center is excluded to avoid pile-up (see Section 2.3). The resulting lightcurve is binned over 1 s.

[1] see http://heasarc.gsfc.nasa.gov/
[2] see http://heasarc.gsfc.nasa.gov/docs/xte/appendix_f.html

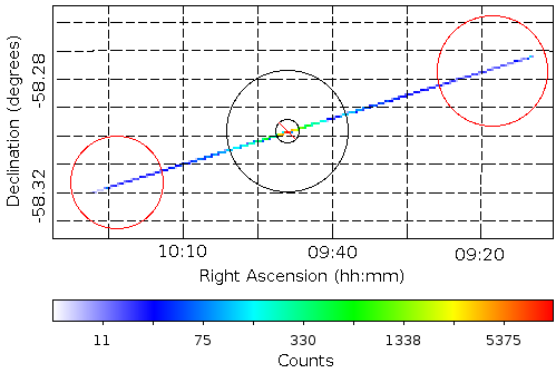

Figure 4.3: The image of GRO J1008–57 as seen by *Swift*-XRT in windowed timing mode. The rows are added by the satellite electronics, resulting in a one dimensional image. The region used to extract the source events is shown as black circle, where a smaller region around the center of the source is excluded to avoid pile-up. The red circles are the regions for the background data.

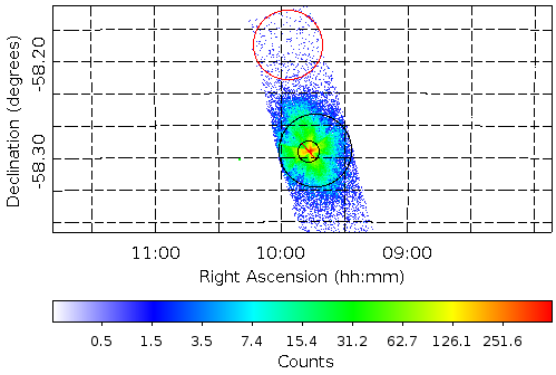

Figure 4.4: The image of GRO J1008–57 as seen by *Suzaku*-XIS3. In imaging mode, the full image of the source is visible. The region used to extract the source events is shown as black circle, where a smaller region around the center of the source is excluded to avoid pile-up. The red circle is the region for the background data.

Similar to *Swift* the events detected by the *Suzaku*-XISs in 2007 are extracted by creating source and background regions on the image. These regions for XIS3 and the corresponding image of GRO J1008–57 can be seen in Figure 4.4. A small region around the source position is excluded due to pile-up. The extracted lightcurve has a time resolution of 5 s. The data of XIS0 and XIS2 are not extracted since they are damaged by micro meteorites (see Section 2.4). Data from XIS1 is also not used due to the higher background count rate. The data recorded by the PIN diode and the HXD are extracted for spectral analysis only.

4.2 Timing Analysis

To analyze the pulse period of GRO J1008–57 nearly all available lightcurves are used. From *RXTE*, only the lightcurves of PCA are used, because of the much better signal to noise ratio of ∼10 compared to ∼2 for HEXTE, which is caused by the different effective areas of these two instruments (compare Figure 2.5 and Figure 2.8). In addition, the source flux at the energy range the PCA is sensitive to is about one order of magnitude higher. For similar reasons the lightcurves recorded by the XIS3 instrument onboad *Suzaku* are used.

4.2.1 Epoch Folding

The lightcurves are automatically corrected to the barycenter by the extraction scripts. Therefore, the lightcurves are analyzed with the epoch folding method (see Section 3.1) without further processing. Although orbit parameters were found by Coe et al. (2007), the lightcurves are not orbit corrected in order to check this orbital solution for consistency with the observations. Since the accuracy of epoch folding is proportional to P^2/T with the pulse period P and the length T of the lightcurve (see Equation 3.6), the search interval for the pulse period is set accordingly. The expected observed pulse period P should be near 93.6 s as found by Coe et al. (2007). A Gaussian is fitted to the resulting

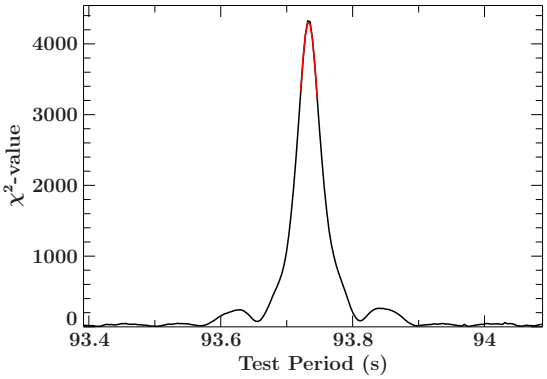

Figure 4.5: The resulting distribution of χ^2-values from epoch folding the *Suzaku* lightcurve. The best-fit of a Gaussian to the maximum (red) reveals a pulse period of 93.735 s.

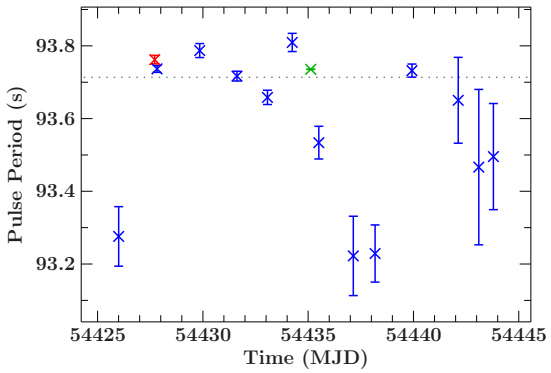

Figure 4.6: Pulse period evolution as determined by epoch folding. Periods found in lightcurves recorded by *RXTE*-PCA are shown in blue, by *Swift*-XRT in red and by *Suzaku*-XIS3 in green. The dashed line shows the Doppler shifted pulse period expected from the orbital parameters of Coe et al. (2007). The calculated 1σ uncertainties of the shown pulse periods are underestimated (for details see text).

distribution of χ^2-values to increase the accuracy of the most likely pulse period. The period interval used for this fit is restricted to a small interval around the maximum due to the fact that the distribution is only approximately Gaussian near the maximum. This also ensures that the fit is not affected by additional secondary maxima (compare Figure 3.2). The resulting pulse period evolution and an example of the result of epoch folding using the *Suzaku*-XIS3 lightcurve is shown in Figure 4.5 and Figure 4.6, respectively. The uncertainty of each pulse period is determined by Monte Carlo simulations as described in Section 3.1. The expected Doppler shifted pulse period due to the orbital parameters found by Coe et al. (2007) (compare Figure 4.1) is shown in addition. Comparing these expected periods to the measured ones shows that the measured pulse periods do not represent an orbital modulation. This is also confirmed by the fact that the relative scatter of these periods of about 6×10^{-3} is much larger than the maximum expected relative Doppler shift of $\sim 3 \times 10^{-4}$ (compare Figure 4.1). An additional spin-up or -down effect can also be ruled out, since the absolute change expected of the pulse period $\dot{P}$ is on the order of $10^{-9}\,\mathrm{s\,s^{-1}}$ as found by Coe et al. (2007). Hence the uncertainties of the pulse periods determined by Monte Carlo simulations are underestimated. The reason might be that systematic errors such as pulse to pulse variations are not taken into account in the Monte Carlo simulation. Hence, by increasing the uncertainties by a factor of ~ 4 the pulse periods are more or less constant over the observations and are in agreement with the pulse period of $P = 93.735\,\mathrm{s}$ found in the *Suzaku*-XIS3 lightcurve.

4.2.2 Phase Connection

The pulse period determined from epoch folding is still shifted by the orbital motion of the neutron star. By using the orbital parameters found by Coe et al. (2007) (see Table 4.1) the lightcurves are binary corrected and the phase connection method (see Section 3.2) is used to determine the pulse period more accurately. Here the pulse profile of *RXTE*-PCA observation #7.9 (see Table C.1) is used as the reference profile required by the method. It is displayed in Figure 4.7. The profile shows two peaks separated by approximately

0.4 in phase. Such a double structure is seen in several transient X-ray binaries, e.g., XTE J1946+274 (Müller et al., in prep.) and 4U 0115+634 (Müller et al., 2010). The pulse profiles are discussed in detail in Scetion 4.2.4. The resulting phase shifts over time, derived by applying the phase connection method, show a parabola shaped correlation (see Figure 4.8). Due to the difficulty of estimating the error of phase shifts with phase connection, the errors are set to the width of the bins used to fold the lightcurves on (compare Equation 3.10). Here the pulse profiles consist of 48 phase bins, which results in an uncertainty of $\sim$0.021 in phase for each measured shift.

Following Equation 3.8, a polynomial of first order, i.e., the frequency f and an $\dot{f}$ is fitted to these phase shifts. The phase shift of the *Swift*-XRT observation is, however, not in agreement with the fit. This discrepancy can be explained by a different pulse shape observed by *Swift*-XRT, since the energy range of this detector is different from *RXTE*-PCA. As a consequence a perfect match cannot be found by cross-correlation, leading to a wrong phase shift. If the *Swift*-XRT observation is excluded from the fit, a reduced χ^2 of 1.6 can be achieved. The parameters are shown in Table 4.2. The accuracy of the binary corrected pulse period found by the phase connection method of $P = 93.72949\,\mathrm{s}$ is at least two orders of magnitude higher than the periods determined by epoch folding, which demonstrates the advantage of the phase connection method over epoch folding. The detected change in pulse period, $\dot{P}$, of $-1.4 \times 10^{-8}\,\mathrm{s\,s^{-1}}$ is, however, larger than the value found by Coe et al. (2007) by a factor of three. This raises the question, whether the measured phase shifts could be caused by orbital effects. Although the lightcurves are corrected for binary motion, uncertainties in the orbital parameters might lead to such effects. For example, the relative uncertainty of the semi major axis $a \sin i$ is larger than 10%. Hence the orbital parameters have to be checked on consistency or to be determined directly from the data. Unfortunately the pulse period evolution determined by epoch folding does not allow to infer the orbital parameters as discussed before (see Figure 4.5). It was this problem which led to the development of the algorithms to analyze the time dependence of the individual arrival times discussed in Section 3.3).

4.2.3 Pulse Arrival Times

To be able to constrain any orbital parameter well the orbital coverage must be good. This is, however, not possible for most transient X-ray binaries. Hence as much data as possible have to be used in the arrival times analysis. Therefore the *RXTE*-PCA lightcurves of the outbursts in 2005 and in 2007 as well as the *Swift*-XRT and *Suzaku*-XIS3 lightcurve of the latter outburst are used. Since the arrival times method is based on the phase connection method, a reference pulse profile has to be created for each detector and outburst. For 2005, the *RXTE*-PCA lightcurve #5.9 is used to create the pattern (see left panel of Figure 4.9) and the reference time $t_{0,2005}$ is set to 53427.66091 MJD, which is the first time bin of the lightcurve. The single lightcurves of *Swift*-XRT and *Suzaku*-XIS3 are used for the 2007 outburst as well as the *RXTE*-PCA lightcurve #7.1. The reference time $t_{0,2007}$ here is set to the first time bin of the *Suzaku*-XIS3 lightcurve, 54434.48194 MJD. Therefore the patterns of *RXTE*-PCA and *Swift*-XRT have to be aligned to the *Suzaku*-XIS3 one (see right panel of Figure 4.9). For each pattern 32 phase bins are used, except for the

Table 4.2: Frequency ephemeris and corresponding pulse period ephemeris determined by a fit of the phase shifts to a first order polynomial according to Equation 3.8.

$f = 0.01066900(3)\,\mathrm{Hz}$	$P = 93.72949(27)\,\mathrm{s}$
$\dot{f} = 1.60(7) \times 10^{-12}\,\mathrm{Hz\,s^{-1}}$	$\dot{P} = -1.41(6) \times 10^{-8}\,\mathrm{s\,s^{-1}}$

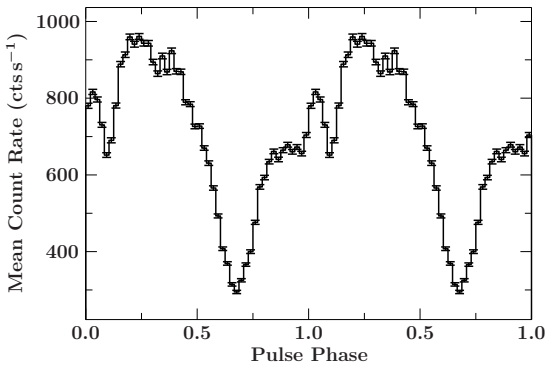

Figure 4.7: The reference profile used for the phase connection method is created by folding the lightcurve of *RXTE*-PCA observation #7.9 on the pulse period (see Table C.1). The profile shows a double peaked structure.

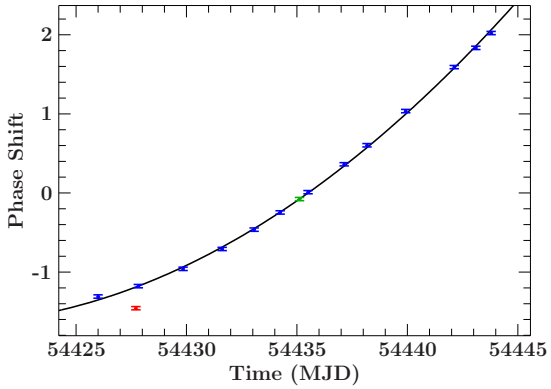

Figure 4.8: The phase shifts determined relative to the reference pulse profile are fitted according to Equation 3.8 up to the second order. The colors are the same as the ones used for Figure 4.5. The phase shift of the *Swift*-XRT lightcurve is off due to a different pulse shape as expected for the different energy range of that measurement. The 1σ uncertainties shown are inversely proportional to the number of bins used to create the pulse profiles.

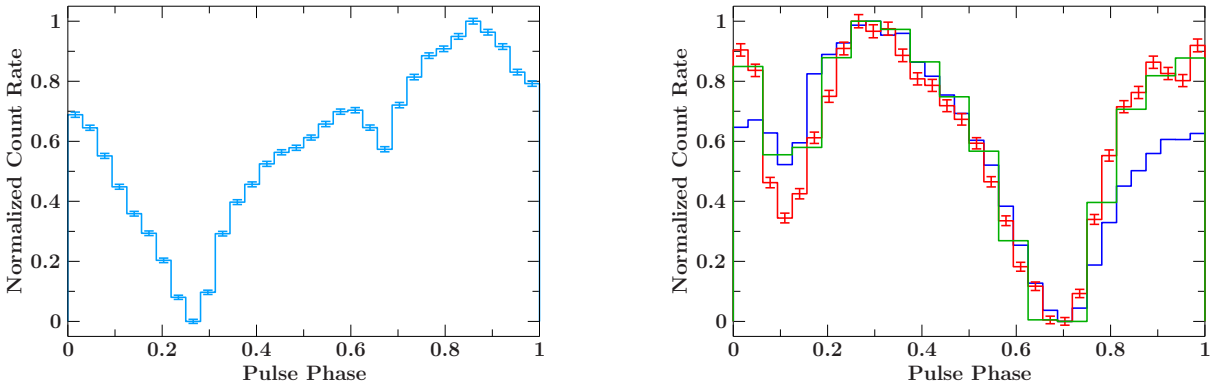

Figure 4.9: The pulse patterns used to determine the arrival times of the outburst in 2005 (left) and 2007 (right). Due to their arbitrary start times (and pulse phases), the 2007 patterns for *RXTE*-PCA (blue) and *Swift*-XRT (red) have to be aligned to the *Suzaku*-XIS3 pattern (green), which defines the reference time. The uncertainties of the *RXTE*-PCA and *Suzaku*-XIS3 pattern are too small to be seen and where therefore omitted.

data from *Suzaku*-XIS3 where only 16 bins are used to increase the signal to noise ratio. Due to gaps in the lightcurve not every single pulse is detected. In addition lightcurves, where the luminosity is too low to resolve single pulses in the lightcurve, are folded to determine the phase shift and hence the arrival time of the pulse profile only. There are in total 1121 arrival times determined and available for analysis. The uncertainties of the arrival times determined by folding the lightcurve are estimated by Monte Carlo simulations according to Equation 3.11 as described in Section 3.3.1. The uncertainties of individual pulses, which constitute most of the 1121 arrival times, are estimated by a local standard deviation of 10 subsequent pulses (see Equation 3.12).

As first step in the analysis of the arrival times, a constant pulse period is assumed and any orbital effects are neglected. The pulse period is set to the value found by the previous phase connection analysis. Because the resulting modelled arrival times are equally spaced

Table 4.3: The simulated impact of uncertain orbital parameters on the pulse ephemeris. The values are determined by varying the orbital parameters found by Coe et al. (2007) within their uncertainties and fitting the simulated arrival times by the pulse ephemeris only. Here the simulated pulse period is set to 93.7 s.

	P_0 (s)	$\dot{P}$ ($\mathrm{s\,s^{-1}}$)	$\ddot{P}$ ($\mathrm{s\,s^{-2}}$)	$\dddot{P}$ ($\mathrm{s\,s^{-3}}$)
$P_{\mathrm{orb}} = 247.80(33)\,\mathrm{d}$	88.1	1.2^{-09}	-1.5^{-33}	1.4^{-61}
$a \cdot \sin i = 530(60)\,\mathrm{lts}$	92.1	3.4^{-10}	-2.5^{-34}	2.3^{-62}
$e = 0.68(2)$	94.2	-1.1^{-10}	5.0^{-35}	-4.3^{-63}
$\omega = -26(8)^\circ$	94.3	-1.3^{-10}	-2.7^{-35}	2.6^{-63}
$\tau = 49189.8(5)\,\mathrm{MJD}$	93.4	6.6^{-11}	-7.3^{-35}	6.6^{-63}

(Equation 3.17), the residuals of the model represent the variation of the pulse period. From the shape of these residuals, which are shown in Figure 4.10, the dominant order can be recognized. The shape of the residuals of the 2007 outburst is approximately a parabola and the ones of the 2005 outburst show linear behavior. The discontinuity of the 2007 residuals before MJD 54430 is due to a phase shift ± 1 and have to be adjusted by hand. The algorithm, which models the arrival times as described in Section 3.3, calculates a wrong pulse number due to the large phase shift. The discontinuity of the residuals for the 2005 outburst around MJD 53431 has the same reason.

Due to the sparse orbital coverage a simple fit of the orbital parameters to the arrival times using a χ^2 minimization algorithm fails. Such a fit requires at least a nearly complete coverage. Therefore simulations are necessary to resolve the model parameters, both orbital parameters and pulse ephemeris (see Table 3.1), which cause the observed shape of the residuals. Two different kinds of simulations are performed:

1. A simulation of the impact of wrong orbital parameters on the resulting pulse ephemeris. Arrival times are simulated by using the orbital parameters found by Coe et al. (2007) and a constant pulse period. The orbital parameters, however, are varied within their uncertainties. The arrival times are then fitted using fixed and unmodified orbital parameters, but a free pulse ephemeris. As a result, the pulse ephemeris is used to fit the wrong orbit and the order of magnitude of the parameters is an indicator for the influence of the orbital parameters on the observed

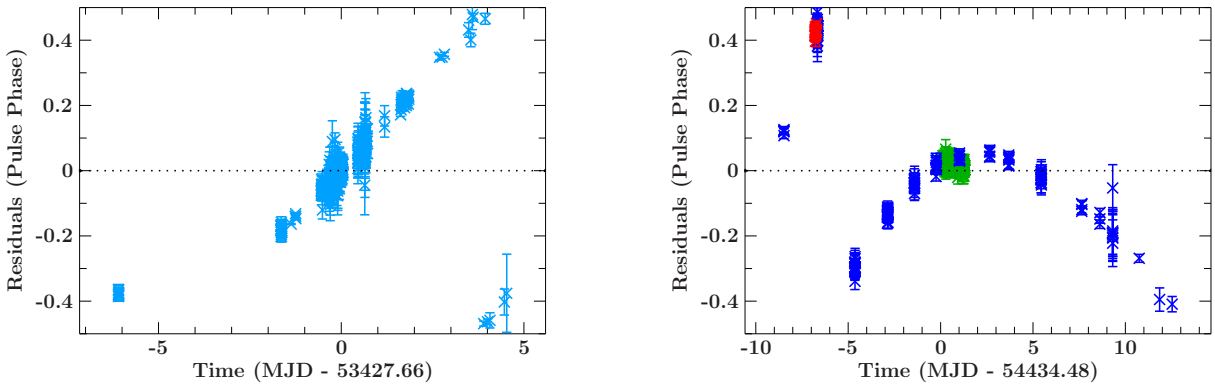

Figure 4.10: The residuals of the modelled arrival times of 2005 (left) and 2007 (right) assuming a constant pulse period. The colors represent different outbursts and detectors as in Figure 4.9. The pulse period determined using the phase connection method (see Table 4.2), leads to the characteristic arrival time residuals displayed on the vertical axes above. The error bars of the residuals represent the 1σ confidence level.

residuals. The result of such a simulation is shown in Table 4.3. The uncertainties of the orbital period P_{orb} lead to the largest change in the pulse period of about 6% and in the first derivative $\dot{P}$ of 10^{-9}. Therefore it is likely that the observed pulse period and its change, determined by phase connection (see Table 4.2), are affected by uncertainties in orbital parameters.

2. The shape of the residuals shown in Figure 4.10 might be connected to a certain parameter. Knowing the theoretical shape of residuals caused by each parameter might constrain the allowed parameter ranges during a fit. To obtain the theoretical shapes of the residuals similar simulations as before are performed. In contrast the simulated arrival times are not fitted by the pulse ephemeris. Rather each model parameter is varied and the resulting residuals are shown only. To get useful parameter ranges the parameters are varied such that the residuals do not lead to phase shifts above 0.5 or below -0.5 since values outside this range are not suitable. The simulated shapes of the residuals caused by uncertainties in each model parameter can be found in Figures 4.11 to 4.19. As expected from Equation 3.16 the residuals produced by uncertainties in the pulse ephemeris are shaped according to the order of their contribution. The residuals of a parameter are, however, influenced if the parameter of the next order is not zero. The higher order term is also visible if both terms are of the same order.

Comparing the simulated shapes of the residuals to the measured ones reveals that more parameters are not determined correctly: the residuals in 2005 are more or less linear, while the ones in 2007 show a parabola-like shape. As mentioned before the most likely parameter to produce these residuals is the orbital period P_{orb} (compare Table 4.3). The periastron passage of the discovery outburst in 1993 was 14 years before the outburst in 2007. Due to the uncertainty of the corresponding orbital parameters found by Coe et al. (2007), the error of the orbital phase in 2007 can be quite large. The orbital phase zero is defined at the time of periastron passage τ, hence the phase depends on this time and also on the orbital period P_{orb}. If the orbital phase for the 2007 outburst is calculated wrongly, the resulting effects can be artificially modelled by both parameters. Hence these parameters influence each other during a fit: they are correlated. This correlation is visualized by creating a contour map of the parameters. Here both parameters are varied in discrete steps and the remaining free parameters are fitted to the data. Finally the resulting χ^2-values for each step are plotted depending on the parameter values chosen. To check the correlation between P_{orb} and τ a contour map of simulated arrival times is calculated. The advantage of this approach instead of using measured data is that other influences, like uncertainties of additional parameters, are ruled out. The orbital parameters of the simulated arrival times are set according to Table 4.1 and a pulse period of 93.7 s is assumed. The time of periastron passage and the orbital period are varied within their uncertainties each with 100 steps of equal size. Due to the expected linear residuals (see Figure 4.15 and Figure 4.16) the pulse period is used as free parameter only (see Figure 4.11). The resulting contour map, shown in the left panel of Figure 4.20, shows, as expected, a clear correlation: the region of acceptable χ^2-values (drawn in black) is a diagonal, that means a wrong time of periastron passage τ can be mimicked by a corresponding change in orbital period P_{orb}. The time of periastron passage τ_n of orbit number n relative to the reference measurement at τ can be calculated as

$$\tau_n = \tau + nP_{\mathrm{orb}} \tag{4.1}$$

That means that the time of periastron passage can be extrapolated to the outburst in 2007. Between the 1993 outburst, where GRO J1008–57 has been discovered, and the outburst in 2007, the neutron star has orbitted its companion 21 times. Hence the time

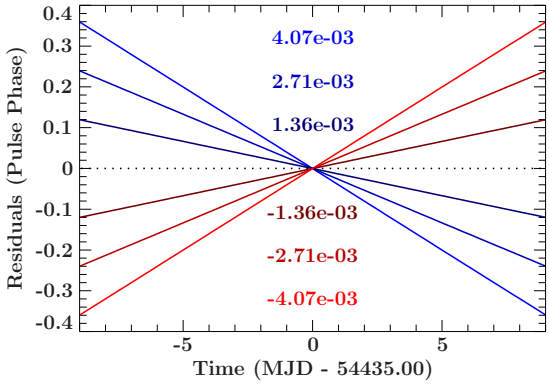

Figure 4.11: An uncertain pulse period results in linear residuals. The different values in seconds assumed for this paramter are indicated in the plot. The original pulse period is set to 93.7 s.

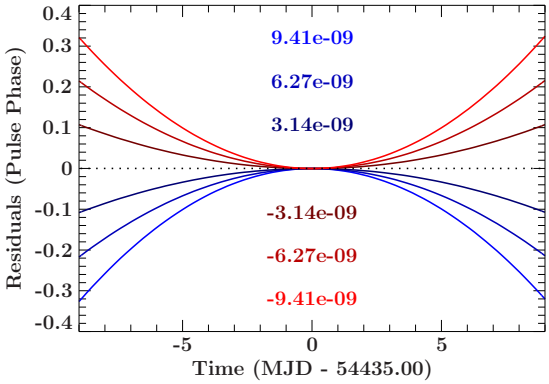

Figure 4.12: An uncertain first derivative of the pulse period results in parabolic shaped residuals. The different values in $\mathrm{s\,s^{-1}}$ assumed for this paramter are indicated in the plot. The original first derivative is zero.

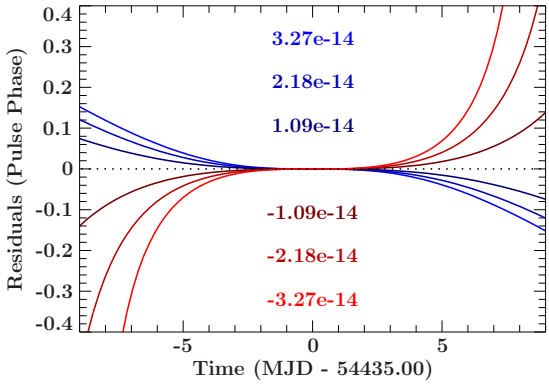

Figure 4.13: An uncertain second derivative of the pulse period results in third order shaped residuals. The different values in $\mathrm{s\,s^{-2}}$ assumed for this paramter are indicated in the plot. The original second derivative is zero.

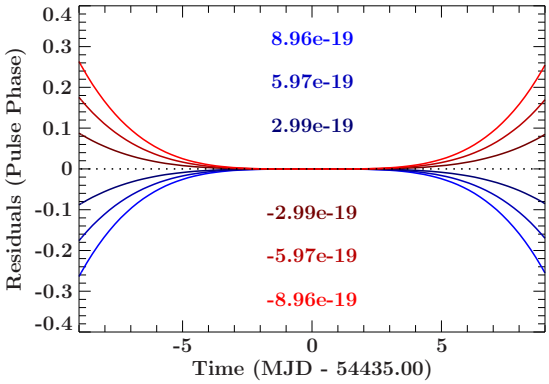

Figure 4.14: An uncertain third derivative of the pulse period results in fourth order shaped residuals. The different values in $\mathrm{s\,s^{-3}}$ assumed for this paramter are indicated in the plot. The original third derivative is zero.

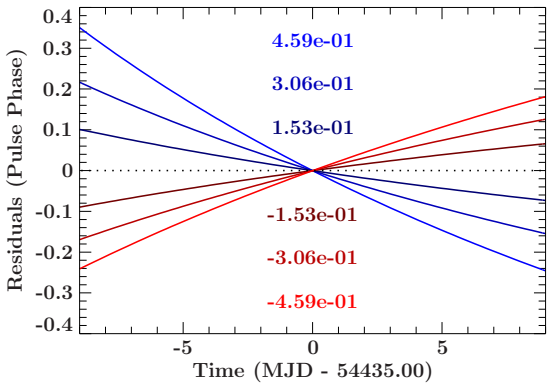

Figure 4.15: An uncertain orbital period results in nearly linear residuals. The different values in days assumed for this paramter are indicated in the plot. The original orbital period is 247.8 d.

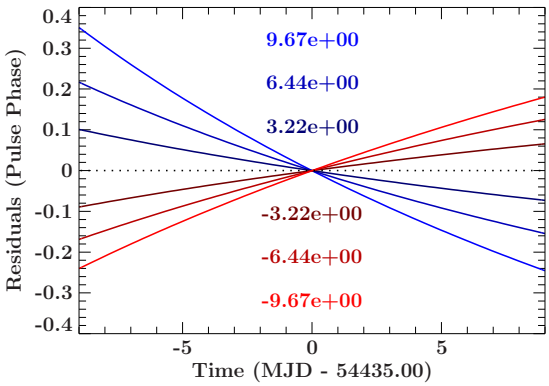

Figure 4.16: An uncertain time of periastron passage results in nearly linear residuals. The different values in days assumed for this paramter are indicated in the plot. The original time of periastron passage is MJD 49189.8.

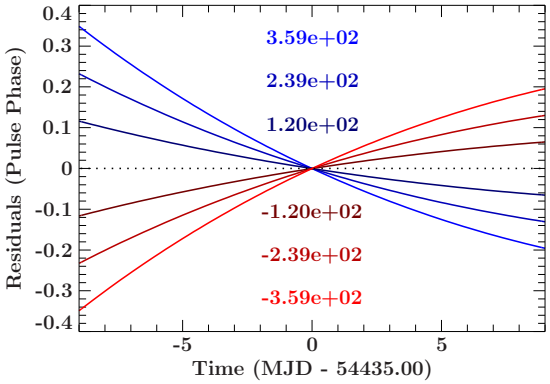

Figure 4.17: An uncertain semi major axis results in slightly curved residuals. The different values in lt-s assumed for this paramter are indicated in the plot. The original semi major axis is 530 lt-s.

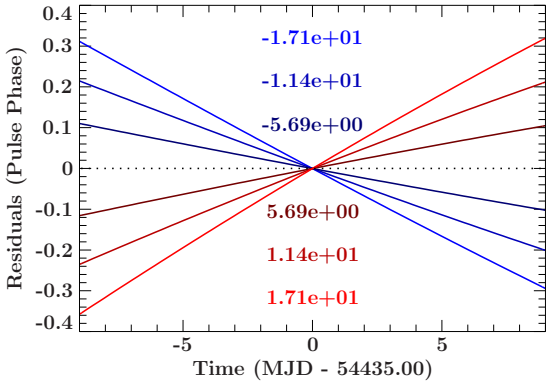

Figure 4.18: An uncertain angle between the periastron and the ascending node results in nearly linear residuals. The different values in degrees assumed for this paramter are indicated in the plot. The original angle is -28°.

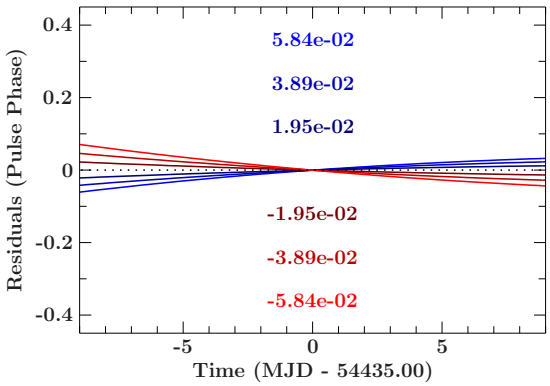

Figure 4.19: An uncertain eccentricity does not affect the residuals strongly. This is based on the fact that the observations cover only a small fraction of the full orbit. The different values assumed for this paramter are indicated in the plot. The original eccentricity is 0.68.

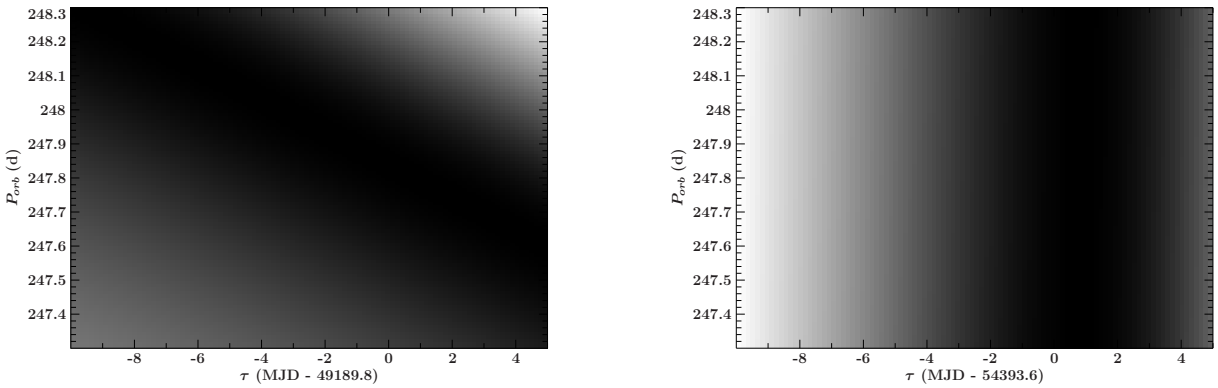

Figure 4.20: Simulated contour map of the time of periastron passage τ versus the orbital period $P_{\rm orb}$. The normalized χ^2 values are color coded from low (black) to large values (white). The map reveals a correlation between both parameters (left), which are set to the values of Table 4.1. When using a local epoch of periastron passage in 2007, the correlation is gone (right).

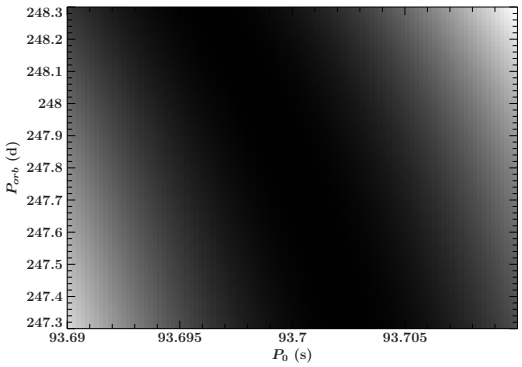

Figure 4.21: The contour map of the orbital period $P_{\rm orb}$ and the pulse period P. The normalized χ^2 values increase from black to white. The orientation of the black valley shows that both parameters are correlated.

of periastron passage in 2007 is calculated using the orbital parameters of Table 4.1 to

$$\tau_{21} = 54393 \pm 9 \text{ MJD} \tag{4.2}$$

The contour plot described above is calculated again, but this time for the new epoch of periastron passage τ_{21} calculated by Equation 4.2 against the orbital period $P_{\rm orb}$. The right panel of Figure 4.20 demonstrates that these two orbital parameters are not correlated anymore. Both parameters can now be fitted to the measured arrival times independently.

It turns out that a simple χ^2-minimization cannot be used to describe the measured arrival times shown in Figure 4.10. The reason is a strong correlation between the orbital parameters and the pulse ephemeris due to the sparse orbital coverage. As an example, a contour plot of the orbital period $P_{\rm orb}$ and the pulse period P is shown in Figure 4.21, which shows a similar correlation as Figure 4.20 (left panel). To find a reasonable solution for both the orbital parameters and the pulse ephemeris, a different approach is used: the measured arrival times are modelled without taking the orbit into account, that means the parameters of the pulse ephemeris are used to describe the Doppler shift caused by orbital motion and the angular momentum transfer simultaneously. The result represents the pulse period as measured on Earth. The fit of the arrival times in 2005 and 2007 succeeded with $\chi^2_{\rm red}$ of nearly 1.0 after 32 iterations according to the process illustrated in Figure 3.4. The residuals and the resulting pulse period evolution are shown in Figure 4.22. Considering the plotted uncertainties of the pulse ephemeris and comparing the 2007 ephemeris to Figure 4.5 demonstrates the enhanced accuracy compared to epoch folding.

To disentangle the pulse period evolution from the contribution of the Doppler shift and the angular momentum transfer, the correlation between luminosity and pulse period evolution is taken into account (see Section 1.2.3). From Equation 1.15 the first

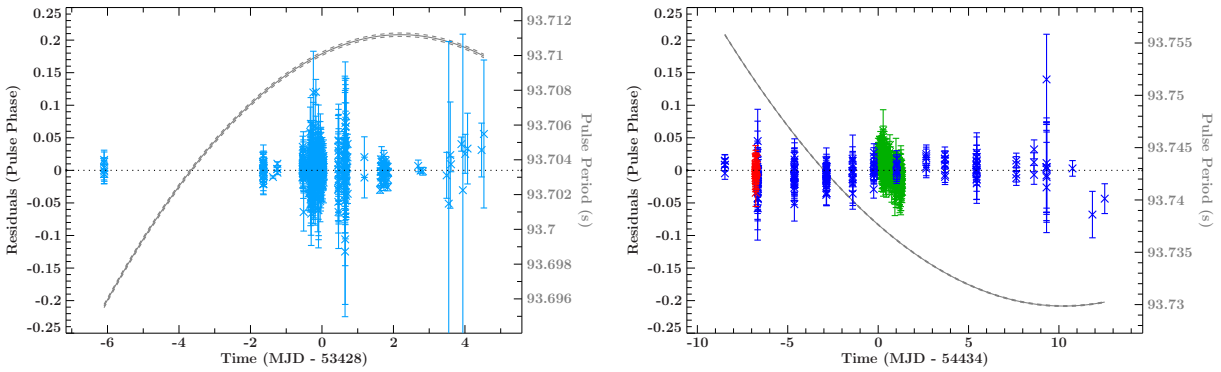

Figure 4.22: Residuals of the arrival times analysis for the outbursts in 2005 (left) and 2007 (right). The colors are coded as in Figure 4.10 and the uncertainties are at the 1σ confidence level. Orbital effects are not taken into account. The resulting pulse period (shown as a gray line) therefore includes the Doppler shift caused by orbital motion and angular momentum transfer. Uncertainties of this pulse period are shown as dashed line and represent the 2σ confidence level.

derivative of the pulse period $\dot{P}$ is expected to be correlated with the luminosity L of the source. Due to the low luminosity the Doppler shift by orbital motion should dominate the observed pulse period evolution at the end of the observed outbursts in 2005 and 2007. The arrival times of both outbursts are, therefore, modelled simultaneously in the epochs of low luminosity including also the orbital parameters. Due to the results of the residual simulations (see Table 4.3 and Figure 4.11 to 4.19) the orbital period $P_{\rm orb}$ is fitted to describe the arrival times during these epochs. The pulse period is considered to be constant. If the uncertainties of the other orbital parameters do not affect the residuals as strongly as the orbital period, the remaining residuals at higher luminosities should be caused by angular momentum transfer. This approach to describe the observed data succeeded after 20 iterations with a reduced χ^2 of 1.4 and the residuals and the disentangled contributions to the pulse period are shown in Figure 4.23. The resulting parameters can be found in Table 4.4. To achieve a good χ^2-value the time of periastron passage τ is also fitted. Instead of fitting τ, other orbital parameters, such as ω, can be used. A fit of these parameters cannot, however, describe both outbursts simultaneously.

The residuals of the arrival times of the *Suzaku*-XIS3 lightcurve show a slight linear trend. Attempt to fit this trend, however, lead to strong residuals in the arrival times determined by the other detectors. The reason might be a problem in the barycentric correction of the *Suzaku* data pipeline (J. Wilms, priv. comm.). Further analysis of this discrepancy is on-going and outside of the scope of this thesis. It should not affect the derived parameters, since the trend is still within the uncertainties.

The updated parameters lead to a difference for the time of periastron passage compared to the extrapolated one according to Equation 4.1. Using $\tau = 49189.8$ MJD found by Coe et al. (2007) and the updated orbital period $P_{\rm orb} = 249.46$ d, the time of periastron passage is predicted to be on 54428.5±2.6 MJD, while it is fitted to 54424.6±0.5 MJD. Hence, the discrepancy is 3.8±2.6 d, which is significant within the given 90% confidence level. Additional parameter uncertainties might be the reason for this difference. Due to the fact that most of the arrival times can be described by orbital effects only (the pulse period is constant within the errors), this reason is unlikely, but not ruled out. To check the updated parameters, more observations are needed. Until such are available, the lightcurve of the *RXTE* ASM (see Section 2.2) can be analyzed for periodicities. This was done by Levine & Corbet (2006) for many transient X-ray sources, including GRO J1008–57. They found an orbital period of 248.9(5) d, which is consistent with the period found by the arrival times analysis. An analysis of the ASM-lightcurve is also performed within

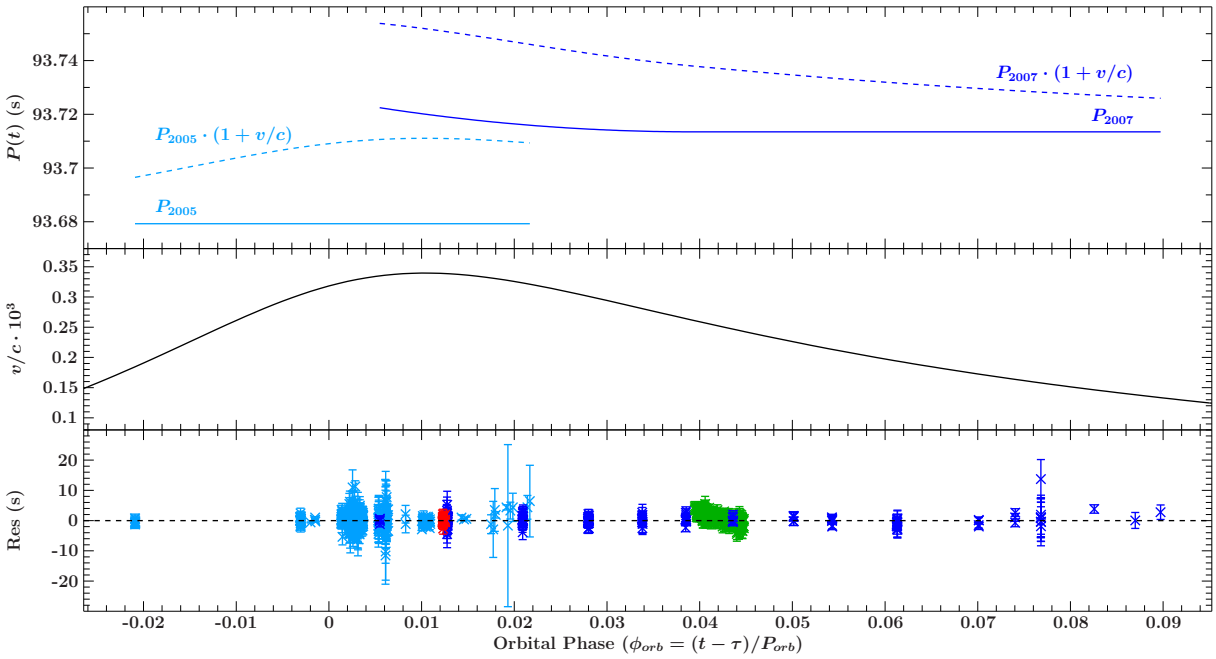

Figure 4.23: The disentangled contributions to the observed pulse period are shown as the function of the orbital phase $\phi_{\rm orb}$: the top panel represents the pulse ephemeris of both outbursts (solid line) and the observed pulse period (dashed line), which is Doppler shifted by orbital motion as shown in the middle panel. The uncertainties of the ephemeris are too small to be displayed properly. The residuals of the best-fit are shown in the lower panel and the colors are the same as in Figures 4.10 and 4.22.

Table 4.4: Updated orbital parameters and pulse ephemeris of GRO J1008–57 as found by the final fit of the arrival times. For comparison the previous orbital parameters are shown (see Table 4.1). The uncertainties of the updated parameters are calculated at the 90% confidence level. To describe the contribution of angular momentum transfer, the pulse ephemeris is splitted at 54434.48194 MJD and both parts are analyzed separately. As a result a $\ddot{P}$ is found for arrival times before the given date.

	Coe et al. (2007)	this work
$P_{\rm orb}$	247.8(4) d	249.46(11) d
e	0.68(2)	(not fitted)
$a \sin i$	530(60) lt-s	(not fitted)
ω	-26(8)°	(not fitted)
τ	49189.8(5) MJD	54424.6(5) MJD

	2005	2007
t_0	53427.66091 MJD	54434.48194 MJD
P	93.67926(10)	93.7135(4) s
$\dot{P}$	0	0
$\ddot{P}$	0	$3.4(1) \times 10^{-14}$ s s^{-1} only for $t < t_0$

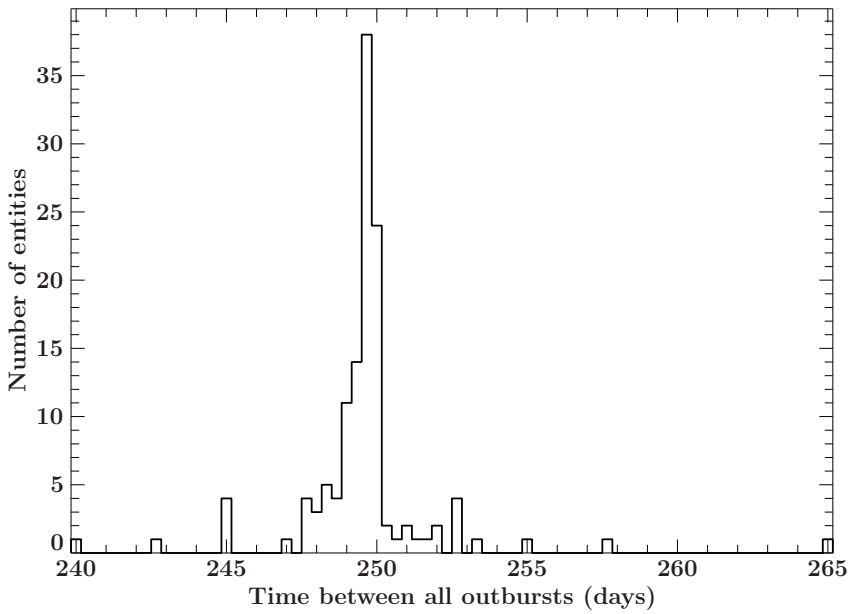

Figure 4.24: Histogram of the differences between the times of the outbursts maxima divided by the number of orbits. The result shows a peak at the orbital period of around 249.7 d.

this thesis.

Since the beginning of the ASM monitoring in 1996 until December 2010 the neutron star has passed its companion 22 times. As a result of the variability of the source not every outburst is visible in the data. From the remaining ones the time of maximum luminosity is determined, resulting in 15 datapoints. Under the assumption that all maxima are located at the same orbital phase, the differences of the time of maximum luminosity for one outburst and times of maximum luminosity for all other outbursts should be exact multiples of the orbital period. The histogram of these time differences divided by the related number of orbits should therefore show a peak at the orbital period. As seen in Figure 4.24, such a peak is located at a time difference of 249.7(3) d, which is in excellent agreement with the value of 249.46(11) d found by the arrival times analysis. The updated orbital period is therefore confirmed by two independent analyses of ASM data.

The successful fit of the arrival times is based on the assumption that the angular momentum transfer onto the neutron star is correlated with the luminosity (see Equation 1.15). As a consistency check, the observed source luminosity L between 15 and 50 keV is plotted against the determined first derivative $\dot{P}$ of the pulse period in Figure 4.25. The change of the pulse period is calculated by the derivative of Equation 3.18 and using the values given in Table 4.4. The plot reveals a correlation between both parameters, which seems to be non-linear. The linear correlation is theoretically derived, however, assuming a spherical and steady mass accretion (see Section 1.2.3). This assumption is not fulfilled if the accreted matter is redirected to the magnetic poles. This has to be the case for GRO J1008–57 due to the presence of pulsations and therefore a strong magnetic field.

Comparing the pulse period of the outburst in 2005 to the 2007 one sees a spin down of the neutron star. This spin down is confirmed by further measurements of the pulse period over the decades, which is shown in Figure 4.26. The observed spin up during the outburst in 2007 is, however, in contradiction to the long term spin down. An explanation might be that the sign of $\dot{P}$ changes between the outbursts. Hence also a spin down during an outburst should be detectable. Unfortunately, no further observations exist to check this hypothesis. The presence of a long term spin down, which is independent

from mass accretion, might also explain the observations. This is also observed in, e.g., OAO 1657−415 (Barnstedt et al., 2008) and several further sources (Bildsten et al., 1997). The physical process, which leads to long term deceleration, is yet not understood. This might be due to inner friction of the neutron star, but since the inner structure is not observable only theoretical models can be considered.

4.2.4 Pulse Profile Evolution

The updated orbital parameters and the determined pulse ephemeris are used to create the pulse profiles in the rest frame of the neutron star. During the outburst the profile might evolve due to changes in the mass accretion. Since *RXTE* monitored the 2005 and 2007 outbursts starting at maximum luminosity the evolution of the pulse profile during the decay of an outburst can be studied. The lightcurves of the PCA are used because of the higher count rates than in HEXTE data. In addition to the already mentioned lightcurves, PCA-lightcurves for certain energy ranges are extracted from the raw data to resolve possible energy dependence. The lightcurves are corrected for orbital motion and are afterwards folded on the time dependent pulse period using Equation 3.18. As an example for the evolution during the decay, the pulse profiles of the observations #7.1, #7.7 and #7.12 are shown in Figure 4.28. The profile at high luminosity clearly reveals a double peaked structure as found before with the phase connection analysis (see Figure 4.7). The peaks are seperated by two gaps, whose minimum count rate relative to each other is different. In this thesis, the peak directly after the deeper gap is refered to as the *first* peak and the other one as the *second*. A double peaked pulse profile can be produced by a contribution from the second pole on the neutron star which is visible due to lightbending (Blum & Kraus, 2000). As an example the pulse profile of Her X-1 can be explained by this model (Kuster, 2004). The two peaks in the pulse profile of GRO J1008–57 are of comparable strength and width, which is, however, unlikely to be a result of light blending. This double peaked pulse profile is also observed during the decay

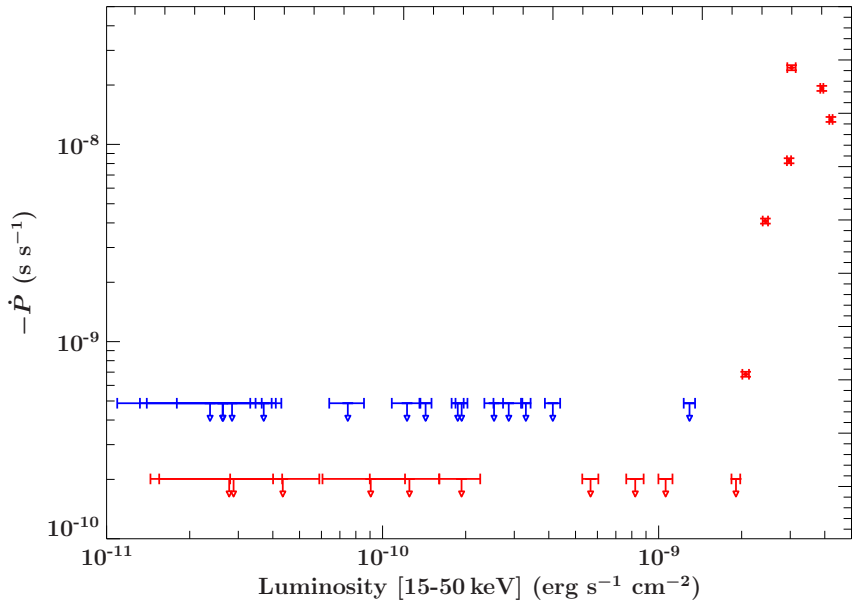

Figure 4.25: The source luminosity L between 15 and 50 keV measured in the 2005 (blue) and 2007 outburst (red) is shown versus the determined change $\dot{P}$ of the pulse period. Theory predicts a nearly linear correlation (compare Equation 1.15), which cannot be confirmed so far since no pulse period change is detected for most of the data. Where only upper limits are calculated, they are indicated by arrows.

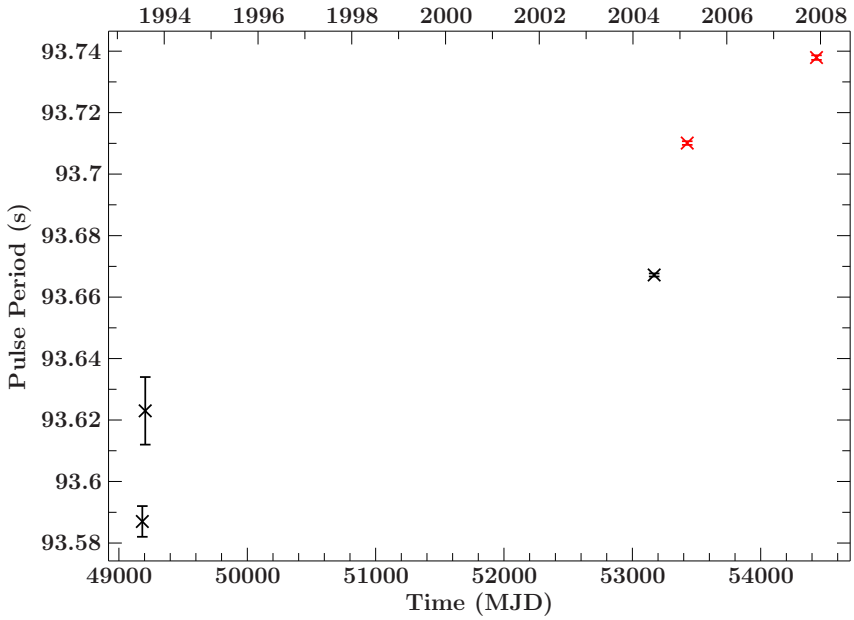

Figure 4.26: The pulse periods over the decades measured by Stollberg et al. (1993), Shrader et al. (1999) and Coe et al. (2007) are shown in black. The red periods are determined in this work. The general pulse period evolution shows a spin down, while a spin up is measured during the outburst in 2007 (see Figure 4.23 and Table 4.4). The periods are not corrected for binary motion, which does not affect the spin-down trend since the outbursts take place at approximately the same orbital phase.

of the outburst and is more or less stable until the luminosity is near the background level. The first peak shows, however, some variability in strength and shape.

The energy dependent pulse profiles, shown also in Figure 4.28, reveal that the first peak decreases with increasing energy, while the second peak does not change significantely. The relative strength between both peaks depends on the energy and is indicating either a powerlaw or an exponential decay (see Figure 4.27). For energies above ∼21 keV the first peak nearly vanishes, hence a single-peaked pulse profile is detected. Although a similar energy dependence is found in other transient X-ray binaries, e.g. XTE J1946+274 (Müller et al., in prep.), 4U 0115+634 (Müller et al., 2010) and A 0535+26 (Caballero et al., 2007), the physical explanation is still lacking. Analyzing the X-ray spectrum of the binary might help to clarify this question.

4.3 Spectral Modelling

The spectrum of GRO J1008–57 was described successfully by Shrader et al. (1999) using a thermal bremsstrahlung model with a plasma temperature of 32 keV. To check whether the spectrum of the source changed since its discovery in 1993 the spectrum of the 2007 outburst observed by *RXTE* is fitted with the same model and characteristic temperature. However, the model is extended by photoelectric absorption (see Equation 1.22), which is expected to contribute for energies below ∼10 keV:

$$S_{\mathrm{model}}(E) = \texttt{tbnew} \times \texttt{bremss} \tag{4.3}$$

Since both detectors, PCA and HEXTE, are different in their response (see Sections 2.2.1 and 2.2.2) a factor S_{HEXTE} has to be used to scale the count rates measured by HEXTE relative to PCA. In addition a factor B_{PCA} is used to adjust the background substraction of the PCA spectrum due to the fact that the background has to be estimated. The measured count rate spectrum of observation #7.3 and the fitted model is shown in Figure 4.29. The corresponding parameter values can be found in Table 4.5. The large reduced χ^2 of 5.4 results from an unmodelled strong emission feature between 6 and 10 keV. Also an absorption feature is present between 70 and 90 keV, which might correspond to the claimed cyclotron line at 88 keV (Shrader et al., 1999). Hence the bremsstrahlung model cannot describe the spectrum of the 2007 outburst well.

The observed broad emission feature might originate from blackbody radiation of a hot spot on the neutron star or in the accretion column. Including the corresponding model `bbody` (see Equation 1.18) leads to a better fit at energies below 10 keV, but the overall continuum modelled by `bremss` does not not properly describe the spectrum at high energies anymore. Therefore, the continuum is modelled by a cutoff powerlaw. A first fit leads to an accetable reduced χ^2 value of about 1.7, but the fit can be improved further by including an iron Kα line modelled by a Gaussian (see Section 1.2.6):

$$S_{\mathrm{model}}(E) = \texttt{tbnew} \times (\texttt{bbody} + \texttt{cutoffpl} + \texttt{gauss}) \tag{4.4}$$

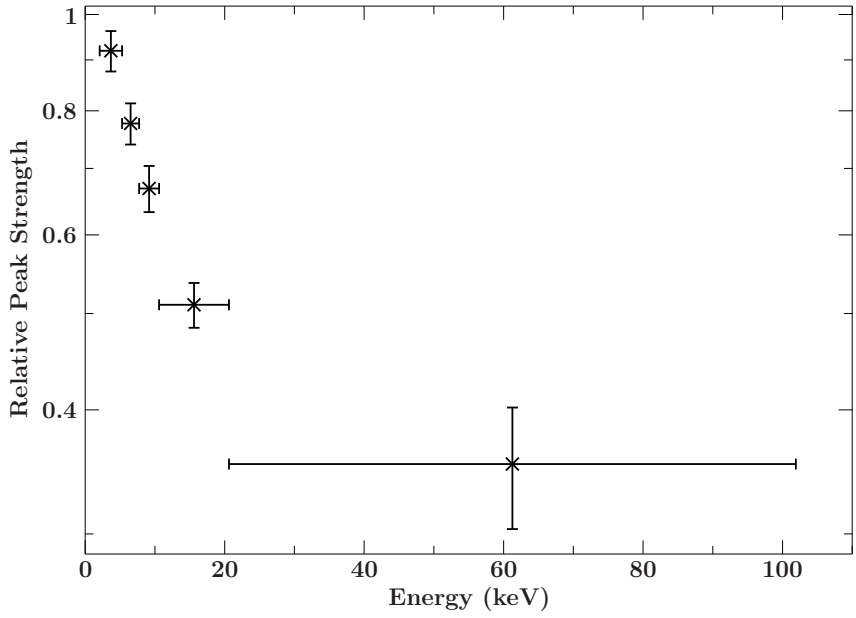

Figure 4.27: Relative strength of both peaks of the pulse profile depending on the energy. The strength is determined from observation #7.1 by dividing the detected counts in the first peak by the counts in the second one. The total counts in each peak is the sum of the count rate in a certain pulse phase interval, which is shown in the left upper panel of Figure 4.28.

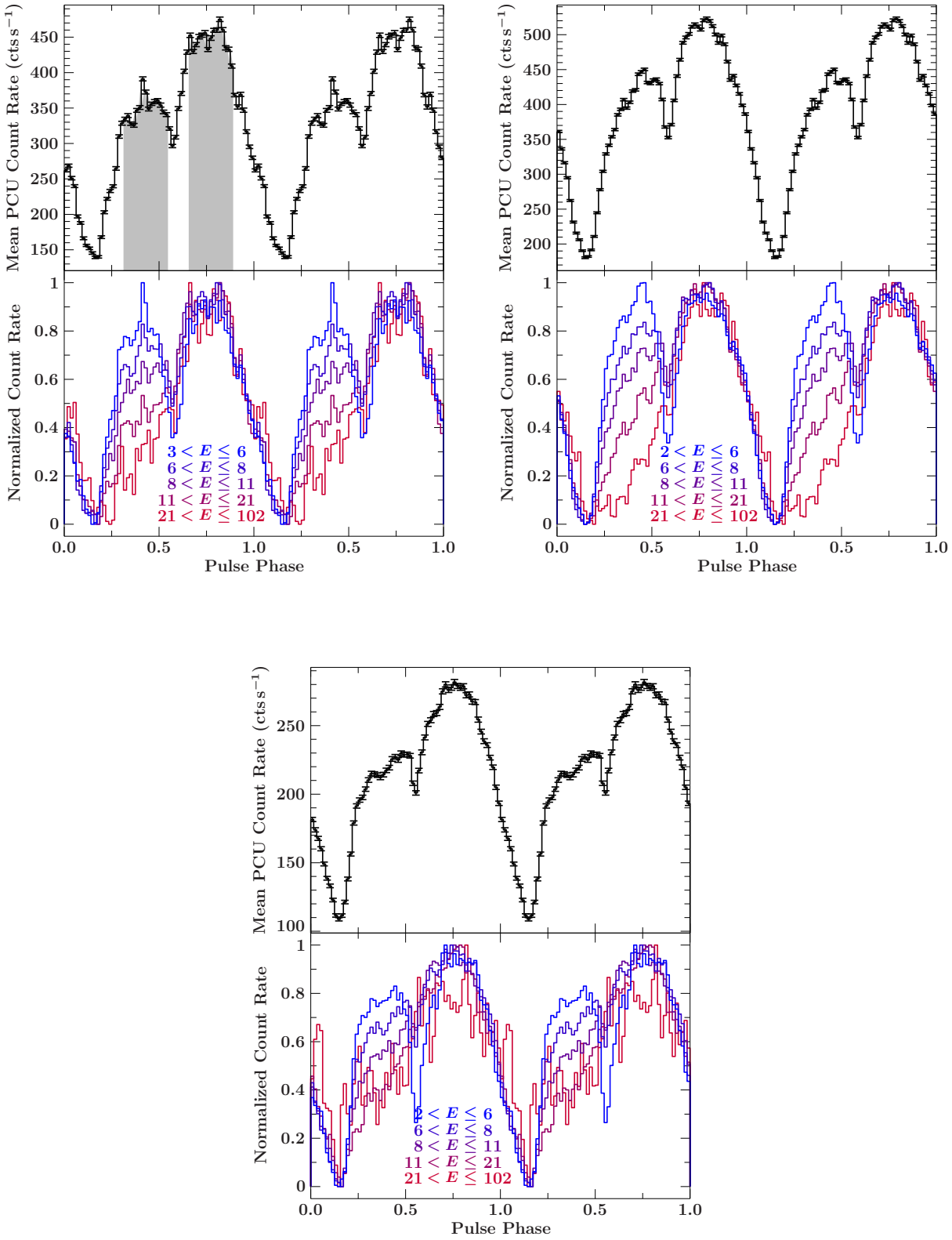

Figure 4.28: The pulse profiles of observations #7.1 (left top), #7.7 (right top) and #7.12 (bottom). A double peaked structure is observed for the full energy range (black profiles), while the first peak decreases with increasing energy (blue to red profiles). The shown energy ranges are given in keV. The second peak is stable during the outburst, while the first one shows some variability in strength and shape. This is also visible in the energy resolved pulse profiles. The gray regions of observation #7.1 are used to determine the relative peak strength as shown in Figure 4.27.

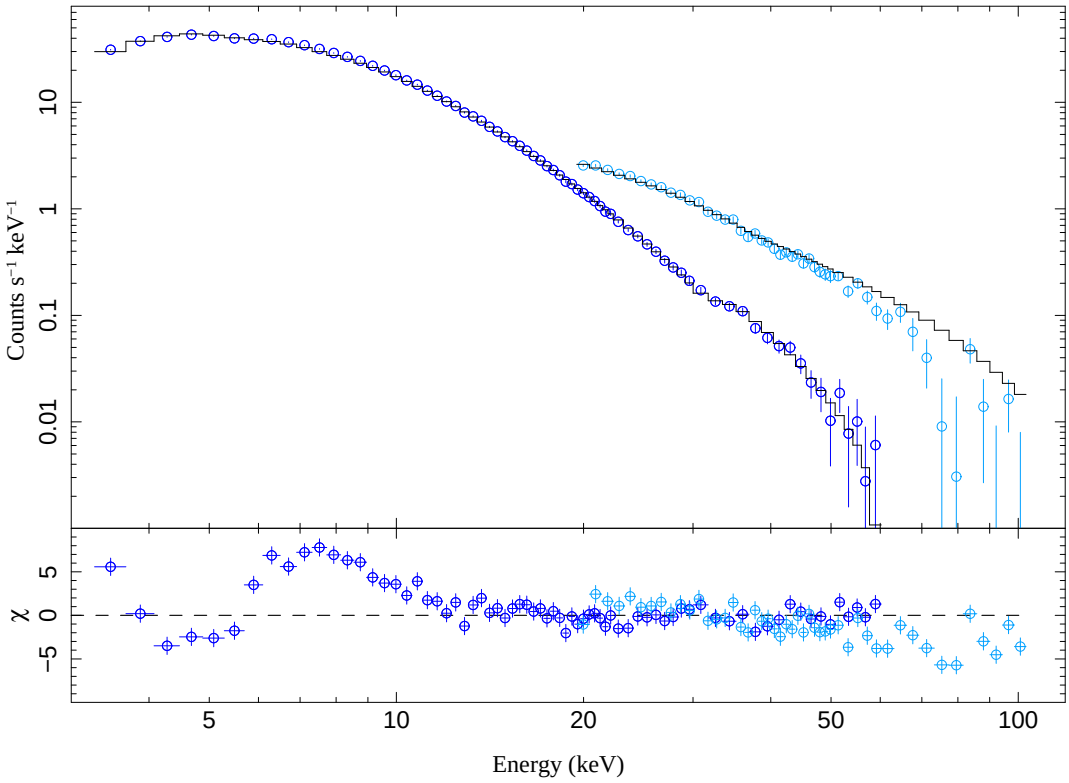

Figure 4.29: The count rate spectrum of observation #7.3 measured by PCA (dark blue) and HEXTE (light blue). A strong emission feature between 6 and 10 keV is visible, which leads to a large reduced χ^2 of 5.4.

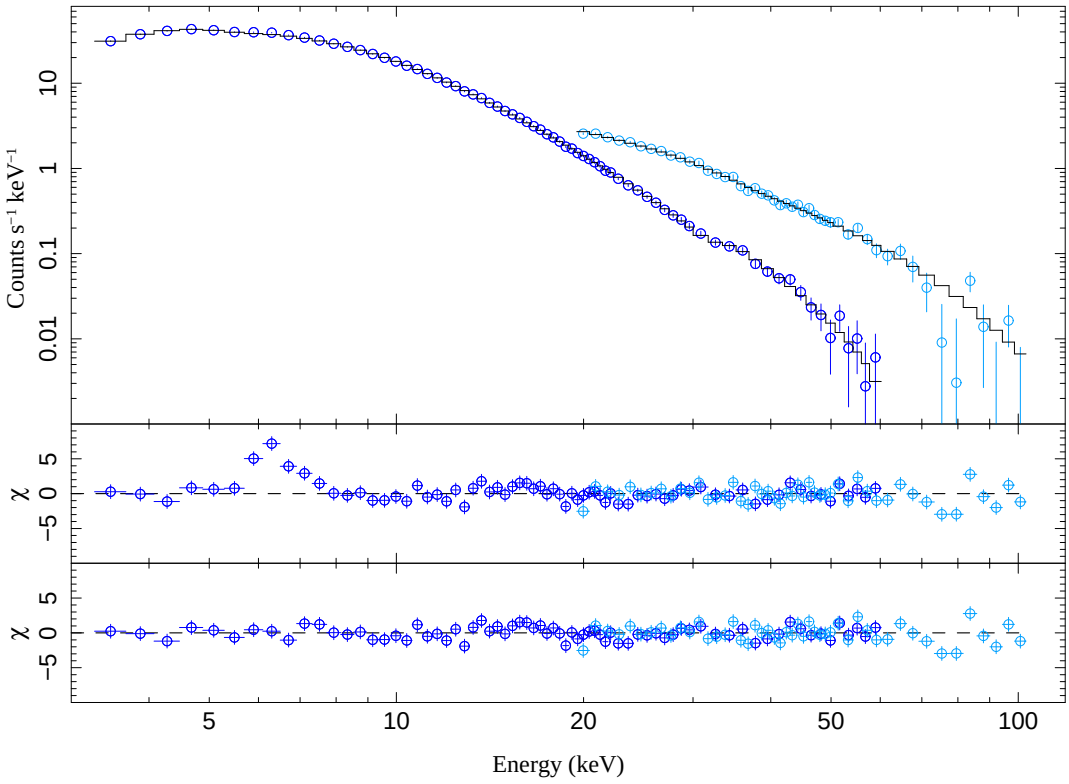

Figure 4.30: The count rate spectrum of observation #7.3 modelled by an absorbed cutoff powerlaw in combination with a black body. In the corresponding residuals (upper residuals) a slight emission feature between 6 and 7 keV is visible, which is successfully modelled as an iron Kα emission line (lower residuals). The spectrum is described well with an reduced χ^2 of 0.8. The colors are coded as in Figure 4.29.

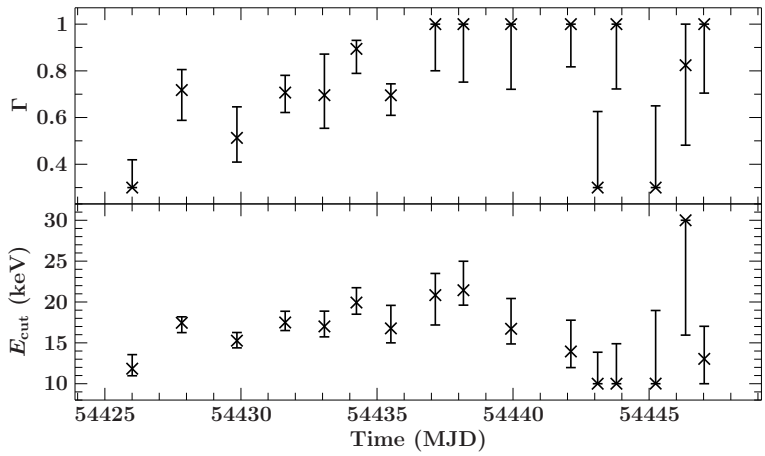

Figure 4.31: Evolution of the cutoff powerlaw parameters E_{cut} and Γ over the outburst in 2007. The curves show similar features, in consequence the parameters might be correlated. The uncertainties at the end of the outburst are quite large due to the low signal to noise ratio.

Here the centroid energy is fixed to 6.4 keV and the width to 1 μeV. Due to the PCA energy resolution (see Section 2.2.1) the line gets broadened. The spectrum of observation #7.3 can be described well with a reduced χ^2 of 0.8. The model residuals are shown in Figure 4.30 and the parameter values can be found in Table 4.5. In comparison to the model using thermal bremsstrahlung, the absorption like feature between 70 and 90 keV (see Figure 4.30) is much weaker and narrower. Again, this absorption might be caused by the proposed cylctron line at 88 keV. Including a cyclotron model `cyclabs` cannot, however, improve the fit and due to the low signal to noise ratio, the uncertainties of all the parameter values are as large as the allowed parameter ranges. The column density N_{H} of the photometric absorption is different between both models by more than a factor of two. This change is explained by the presence of the black body, which influences the count rates in the same energy range where the absorption takes place. The blackbody and absorption contributions cannot be disentangled due to the fact that PCA does not cover the soft energy range below 3 keV. Due to the good χ^2_{red} of the fit by the cutoff powerlaw and black body model, the N_{H} of this model is more trustworthy.

4.3.1 Spectral Evolution

Once the spectrum of GRO J1008–57 is described successfully using the model defined in Equation 4.4, the evolution of the spectral parameters over the outburst can be studied. The spectra of all *RXTE* observations listed in Table C.1 are fitted and the resulting parameters are compared. The first fits show evidence for a correlation between the cutoff energy E_{cut} and the powerlaw index Γ (see Figure 4.31). To check on this correlation, a contour map of these parameters is created for high and low luminosities. The result shown in Figure 4.32 confirmed the correlation between the cutoff energy E_{cut} and the photon index Γ. In consequence, one parameter has to be fixed to determine a reasonable evolution. The χ^2-valley in the contour map is shifted by $\sim 1\sigma$ to a higher photon index during the outburst, while the cutoff energy stays constant within its 1σ confidence level. Hence, the cutoff energy is fixed to $E_{\mathrm{cut}} = 17$ keV rather than the photon index.

The resulting parameter evolutions of the outburst in 2005 and 2007 are shown in Figure 4.33. Here, the cutoff powerlaw norm is replaced by the flux $F_{15-50\,\mathrm{keV}}$ in the energy range from 15 to 50 keV. The photon index Γ seems to be constant in the 2007 outburst for luminosities above $10^{-9}\,\mathrm{erg\,s^{-1}\,cm^{-2}}$. Its mean value is fitted to $\Gamma = 0.72(3)$, although it might increase at lower luminosities. This would imply that the source gets softer at

lower luminosities, which is expected since the mass accretion rate $\dot{M}$ is correlated with the luminosity. A lower mass accretion rate leads to less inverse Compton scattering in the accretion column and hence the flux at high X-ray energies decreases. The photon index at the 2005 outburst is not constant, rather it increases from 0.93(10) up to 1.61(10). Besides the first value the luminosity is, however, below $10^{-9}\,\mathrm{erg\,s^{-1}\,cm^{-2}}$, which is in agreement with the increasing photon index in the evolution of the 2007 outburst.

The equivalent column density N_H in the 2007 outburst is consistent with a mean value of $3.5(5) \times 10^{22}\,\mathrm{cm^{-2}}$. At low luminosities, where the signal to noise ratio is low, the uncertainties become as large as the value itself. The same holds true for the 2005 outburst and in addition the value reaches the upper parameter range of $10 \times 10^{22}\,\mathrm{cm^{-2}}$. Considering these facts the remaining values of N_H in the 2005 outburst are only slightly higher than the one in the 2007 outburst. At lower luminosities, which is the case for the 2005 outburst compared to 2007, the ionization of neutral hydrogen decreases, leading to a higher column density N_H. This effect is able to explain the higher values in the 2005 outburst, but is not significant at lower luminosities in the 2007 evolution due to large uncertainties.

The uncertainties of the black body temperature kT during both outbursts are, except for some values in the 2005 outburst, low enough to be able to determine its evolution well. The mean value during the 2007 evolution is determined to 1.82(4) keV, which is stable until the luminosity falls below $\sim 0.5 \times 10^{-9}\,\mathrm{erg\,s^{-1}\,cm^{-2}}$. Below this value the temperature decreases by a factor of four within approximately 7 days. Further on, the last measured value is consistent with zero within its uncertainties. The black body temperature in the 2005 outburst also decreases significantely at low luminosities. The large uncertainties of some values and the jumps to low temperatures are caused by a low signal to noise ratio and hence poorly constrained fits. This can be seen in the uncertainties and jumps of other spectral parameter at the same time. A physical interpretation of the decreasing temperature might be a cooling of the acretion column or the hot spot on the neutron star. Due to a lower mass accretion rate $\dot{M}$ these regions are no longer heated up and cool down emitting black body radiation.

The normalizations of the black body N_bbody and the iron line A_Fe do not show a significant trend over the outbursts. A correlation with the luminosity is expected, but since the contribution of the black body and the iron line to the total flux $F_{15-50\,\mathrm{keV}}$ is low (compare Figure 4.34), the uncertainties are larger than those of the cutoff powerlaw, which dominates the spectrum.

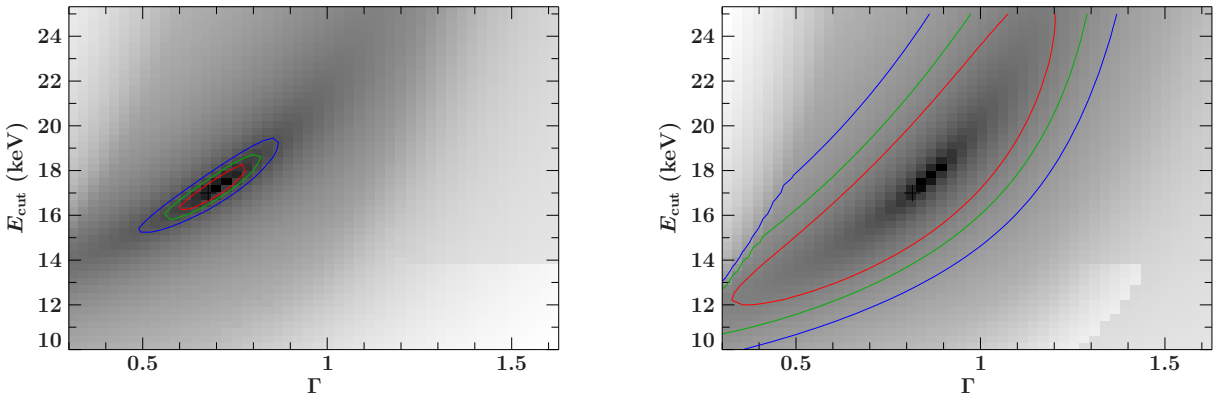

Figure 4.32: The contour map between the cutoff energy E_cut and the powerlaw index Γ at using observation #7.3 (left) and #7.12 (right). The contour lines for the 1σ (red), 90% (green) and 99% (blue) confidence levels indicate a correlation between both parameters at high as well as at low luminosities.

Table 4.5: The parameters of different models fitted to the spectrum of observation #7.3 are shown for comparison. As described in the text a bremsstrahlung model (see Equation 4.3) is used as well as a cutoff powerlaw model with an additional black body component (see Equation 4.4), both affected by photoelectric absorption.

Parameter	Bremsstrahlung	Cutoff powerlaw	Unit
N_{H}	9.94(19)	3.4(8)	$10^{22}\,\mathrm{cm}^{-2}$
kT_{bremss}	32 (fixed)		keV
N_{bremss}	0.887(4)		?
Γ		0.70(11)	
E_{cut}		17(1)	keV
N_{cutoff}		0.14(4)	photons $\mathrm{s}^{-1}\,\mathrm{cm}^{-2}\,\mathrm{keV}^{-1}$
kT_{bbody}		1.90(7)	keV
N_{bbody}		1.1(3)	$10^{-8}\,\mathrm{erg}\,\mathrm{s}^{-1}\,\mathrm{cm}^{-2}$
E_{Fe}		6.4 (fixed)	keV
σ_{Fe}		10^{-6} (fixed)	keV
A_{Fe}		0.21(6)	10^{-2} photons $\mathrm{s}^{-1}\,\mathrm{cm}^{-2}$
S_{HEXTE}	0.829(12)	0.86(3)	
B_{PCA}	0.931(25)	0.98(4)	

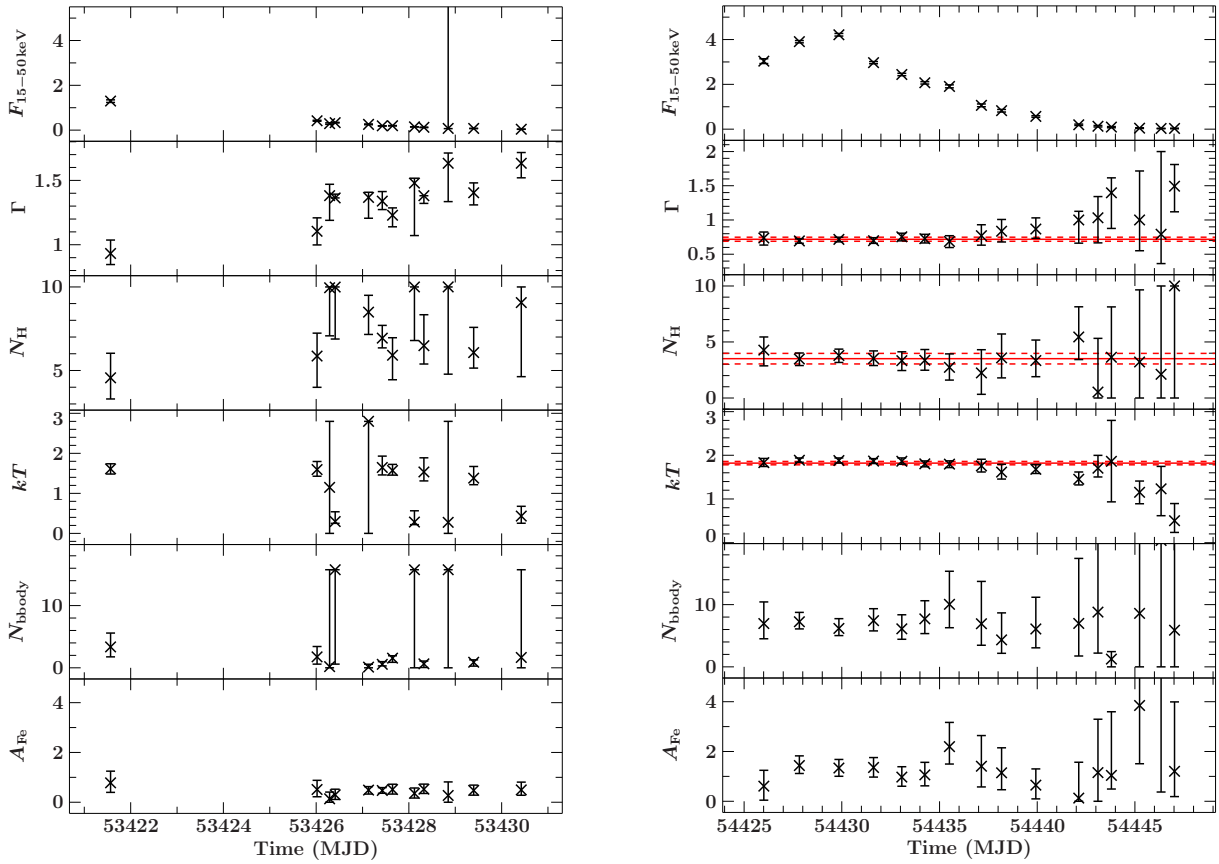

Figure 4.33: Parameter evolution of GRO J1008–57 during the outbursts in 2005 (left) and 2007 (right) is shown. The used model is defined in Equation 4.4, whose cutoff energy E_{cut} is fixed to 17 keV. The background factor B_{PCA} and HEXTE scaling factor S_{HEXTE} are not shown here since they stay, as expected, constant over time. The mean values for parameters, which seem to be constant in at least the main part of one outburst, and the corresponding uncertainties are shown in red. The units of the shown values are equal to those in Table 4.5, and the flux $F_{15-50\,\mathrm{keV}}$ in the accordant energy range is given in $10^{-9}\,\mathrm{erg}\,\mathrm{s}^{-1}\,\mathrm{cm}^{-2}$.

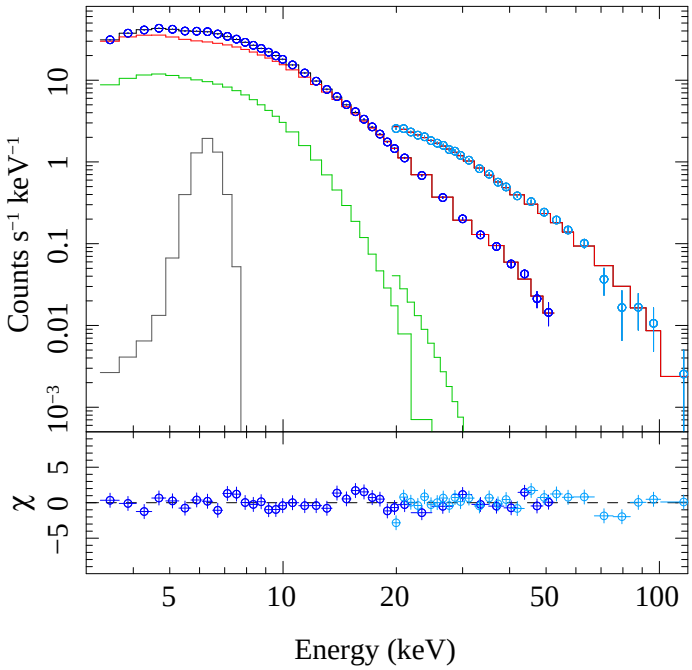

Figure 4.34: Spectrum of observation #7.3 and the best-fit model. The data recorded by PCA (dark blue) and HEXTE (light blue) are in excellent agreement with the model (black line). The model is separated into the cutoff powerlaw (red), the black body (green) and the iron line (gray).

4.3.2 Cyclotron Lines

So far no cyclotron resonant scattering features (see Section 1.2.6) have been detected in the spectra of the 2005 and 2007 outburst of GRO J1008–57. There are indications for an absorption like feature between 70 and 90 keV (see Figure 4.30). The signal to noise ratio is, however, too low to describe this absorption by the cyclotron line model `cyclabs` (see Equation 1.30). In order to increase the signal in this energy range several spectra are summed up. The spectral parameters of the used spectra have to be equal within the uncertainties. If this is not fulfilled the resulting spectrum shows features caused by differences between original spectra rather than by real physical processes. Taking the parameter evolution shown in Figure 4.33 into account the spectra of the following *RXTE* obervations are combined:

#7.A = #7.3 + #7.4 + #7.5
#7.B = #7.4 + #7.5 + #7.6
#7.C = #7.5 + #7.6 + #7.7
#7.D = #7.6 + #7.7 + #7.9
#7.E = #7.7 + #7.9 + #7.10

Although the summed spectra overlap and are not statistically independent, the evolution of a possibly detected cyclotron line can be analyzed.

Since the *Swift* observation #7.2 is located near the summed observation #7.A, the spectra are fitted simultaneously using the model of Equation 4.4. The combined spectra and the corresponding model shown in Figure 4.35 reveal an absorption like feature between 15 and 25 keV. It can be successfully described by the `cyclabs` model using the parameter values shown in Table 4.6. If interpreted as the fundamental line of a cyclotron absorption feature, the claimed cyclotron line at 88 keV, which can still not be confirmed by the summed spectra, would be the third harmonic (k=4). An absorption like feature

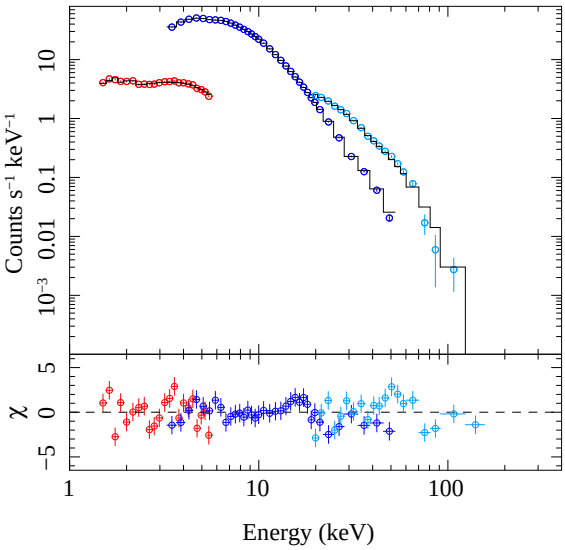

Figure 4.35: The summed *RXTE* spectrum #7.A (PCA in dark blue, HEXTE in light blue) and the *Swift* spectrum (red) including the model defined in Equation 4.4. An absorption like feature between 20 and 25 keV is visible in the residuals (lower panel).

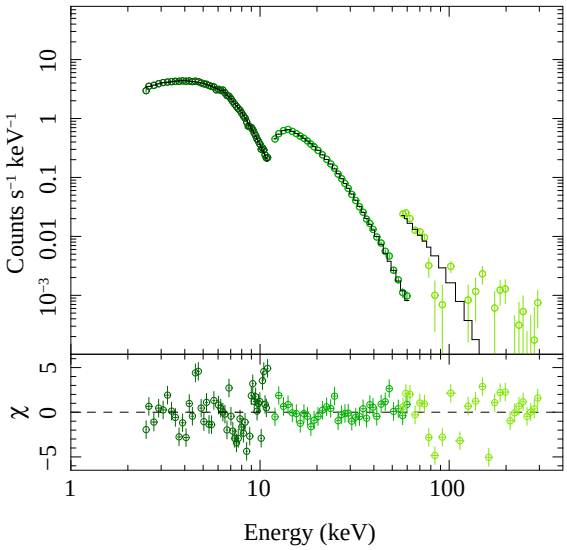

Figure 4.36: The *Suzaku* spectrum of GRO J1008–57 can be described by the model defined in Equation 4.4 (XIS3 in dark green, PIN in light green and GSO in lime). The residuals shown in the lower panel do not show an absorption feature around 23 keV as seen in *RXTE*-PCA (see Figure 4.35 on the left).

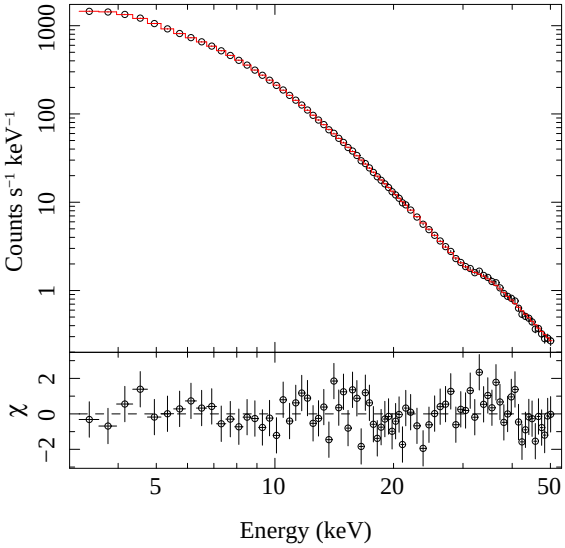

Figure 4.37: The PCA-spectrum of the Crab pulsar of observation 93802-02-04-00 near the observation of GRO J1008–57 is modelled by an absorbed powerlaw. No significant absorption feature is seen in the residuals.

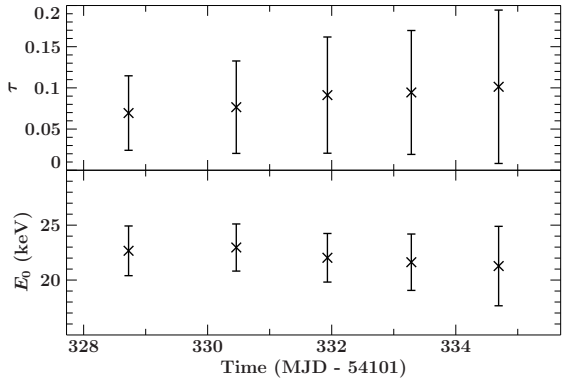

Figure 4.38: Evolution of the fit parameters of the absorption feature at 23 keV. The width W is fixed to the value given in Table 4.6. The uncertainties of τ and E_0 increases with time, i.e. with decreasing luminosity.

Table 4.6: Fit parameters of the absorption feature at 23 keV detected in summed spectrum #7.A recorded by *RXTE*-PCA. To describe this feature the `cyclabs` model is used (see Equation 1.30). The uncertainties are at the 90% confidence level. The signal to noise ratio does, however, not allow for proper error estimation of the width W.

E_0	=	$22.6 \pm 2.3\,\mathrm{keV}$
τ	=	0.07 ± 0.05
W	=	$3.58\,\mathrm{keV}$

around 45 and 66 keV, where the lower harmonics are expected, is, however, not visible in the residuals. The addition of an absorption feature around 23 keV is also able to slightly improve the fits of the other summed up spectra. The evolution of the line parameters (see Figure 4.38) shows that the uncertainty of the line depth τ increases with time. This indicates a luminosity dependence of the line depth, which is consistent with zero at lower luminosities. The uncertainties of the line energy E_0 are also slightly increasing with time, while the best-fit value decreases. The line depth W is fixed to the value shown in Table 4.6.

The detected absorption feature is, however, not confirmed by the *Suzaku* spectrum (see Figure 4.36). The reason is either that the absorption feature is an unmodelled detector feature or that the line depth, which might be luminosity dependent, is too low to be seen in *Suzaku*, since the luminosity during this observation is smaller by a factor of $\sim$2 compared to the summed up observation #7.A. To check on a detector feature *RXTE* observations of the Crab pulsar (ObsIDs 93802-02-04-00 to 93802-02-07-00) are extracted. The Crab pulsar is an isolated neutron star with well known spectrum. Any unknown detector feature should, therefore, be visible in the residuals. The Crab PCA-spectra are modelled by an absorbed powerlaw, which results in the parameters $N_\mathrm{H} = 0.4 \times 10^{22}\,\mathrm{cm}^{-2}$ and $\Gamma = 2.1$. No absorption like features are present in the residuals (see Figure 4.37). Hence a detector feature does not explain the observed absorption feature around 23 keV in the spectrum of GRO J1008–57.

This absorption feature is, like in the *Suzaku* spectrum, not present in the 2005 outburst. There the luminosity is, however, even lower than at the time of the *Suzaku* observation in 2007. A luminosity dependence of the line depth might explain the lack of this absorption line in both cases. Further observations are necessary to confirm the excistence of this absorption feature, which might be a cyclotron resonant scattering feature.

Chapter 5
Summary and Outlook

The observed pulse period of neutron stars is affected by the Doppler shift of orbital motion and the angular momentum transfer due to mass accretion. The orbital parameters and the pulse ephemeris are obtained by analyzing the pulse period evolution. For this purpose, algorithms have been implemented, which allow the determination and modelling of pulse arrival times (see Chapter 3.3). As an advantage compared to, e.g, epoch folding, the orbital parameters and pulse ephemeris can be analyzed simultaneously. Since the arrival times method is based on phase connection (see Section 3.2), the algorithms are able to determine the arrival times with an accuracy in the order of 10^{-5} pulse phases up to 10 days relative to a reference time. This makes this method an excellent tool to analyze transient X-ray binaries, where observations are limited to a short time period around the periastron compared to the orbital period. The algorithms were implemented into a software package to allow other scientific community to do arrival times analyses with this method.

The implemented arrival times method was used to analyze the transient X-ray binaries XTE J1946+274 and GX 304–1 (see Section 3.4) and particularly GRO J1008–57. As a result, the pulse periods of the first two systems were determined to 15.7539668(6) s and 275.3775(15) s, respectively. Although it was not possible to determine the orbital parameters of the systems, the arrival times of XTE J1946+274 were described successfully by a fourth order polynomial. The results of the arrival times analyses of both systems contribute to a long-term project to study accreting pulsars (the "Magnet" collaboration) and were published in several Astronomer's Telegrams (Müller et al., 2010; Kühnel et al., 2010). A refereed publication based on the results presented here is in preparation (Kühnel et al.).

The X-ray binary GRO J1008–57 was discussed in greater detail in Chapter 4. Arrival times analysis reveals significant differences from a constant pulse period (see Figure 4.10). Using the orbital parameters found by Coe et al. (2007) to describe the observed pulse period evolution results, however, in a non perfect fit. Therefore, Monte Carlo simulations were performed to determine the orbital parameter with the strongest influence on the measured pulse period evolution. It was found that an uncertain orbital period leads to a change of the pulse period of $\sim 10^{-9}\,\mathrm{s\,s^{-1}}$, which is of the same order as determined by phase connection before (see Section 4.2.2). Therefore, the arrival times were modelled without taking any orbital effects into account. Assuming that the effect of angular momentum transfer is negligible during epoches of low luminosity and by simulating the shape of the residuals depending on uncertain model parameters, a statistically almost perfect fit was possible. This results in an updated orbital period of $P_{\mathrm{orb}} = 249.46(11)\,\mathrm{d}$ and a new time of periastron passage $\tau = 54424.6(5)\,\mathrm{MJD}$. The orbital period was confirmed by the analysis of the ASM-lightcurve. In addition, a luminosity dependent spin-up of the neutron star of $\ddot{P} = 3.4(1) \times 10^{-11}\mathrm{s\,s^{-2}}$ was detected. The infered orbital parameters of GRO J1008–57 and the pulse ephemeris were used to create pulse profiles at different

times of the outburst. The profiles reveal a double peaked structure, whose first peak changing slightly in shape during the outburst. In addition, the energy resolved profiles show a strong energy dependence of this first peak. At energies above ∼20 keV the peak vanishes almost completely.

The spectra of the outburst of GRO J1008–57 in 2005 and 2007 were analyzed in Section 4.3. Following Shrader et al. (1999), a bremsstrahlung continuum was used to describe the spectra. This model results in non-satisfactory fits with a strong bump between 6 keV and 10 keV. A more reasonable description of the spectrum was achieved by using a cutoff powerlaw in combination with a black body component of a temperature kT around 1.8 keV. In addition, a narrow iron line at 6.4 keV had to be used to describe the spectra adequately. A study of the spectral parameter evolution over the outbursts shows that the black body temperature decreases at low luminosities (see Section 4.3.1). This means that the hot spot or the accretion column, which are visible by black body radiation, is cooling. There is evidence that the photon index Γ increases with decreasing luminosity, indicating that the source becomes softer. This behaviour is expected since the luminosity is connected to the upscattering of photons by the inverse Compton effect. The claimed cyclotron line at 88 keV (Shrader et al., 1999) could not be confirmed by the observations. A weak absorption feature, however, is detected at 23 keV in the PCA spectra. Although the line is not originating from the detector itself, confirmed by comparison to the Crab pulsar, the absorption feature is not visible in the spectra observed by *Suzaku*. This might be caused by a luminosity dependence of the line depth, since the line was observed at high luminosities only. Further observations are neccessary to clarify the existence of an absorption feature around 23 keV in the spectrum of GRO J1008–57.

Using the updated orbital parameters of Table 4.4, the next outburst of GRO J1008–57 since the beginning of this Master's thesis is predicted to be in April 2011. More precisely, the time of maximum luminosity is calculated to be on

$$9^{\text{th}} \text{ April } 2011$$

with an uncertainty of 6 days, which is caused by variability of the source itself. Therefore, an *RXTE* proposal was written and accepted to observe GRO J1008–57 during maximum luminosity. The goals are to check on the absorption feature at 23 keV and the updated orbital parameters. With the support of the *RXTE* team, especially Evan Smith, a monitoring strategy has been worked out to ensure the observation during the maximum. The PCA detector will observe GRO J1008–57 for around 1 ks on a daily basis starting on March 26. The latest lightcurve available at the time of submission of this thesis shown in Figure 5.1 indicates a new outburst of GRO J1008–57, as predicted.

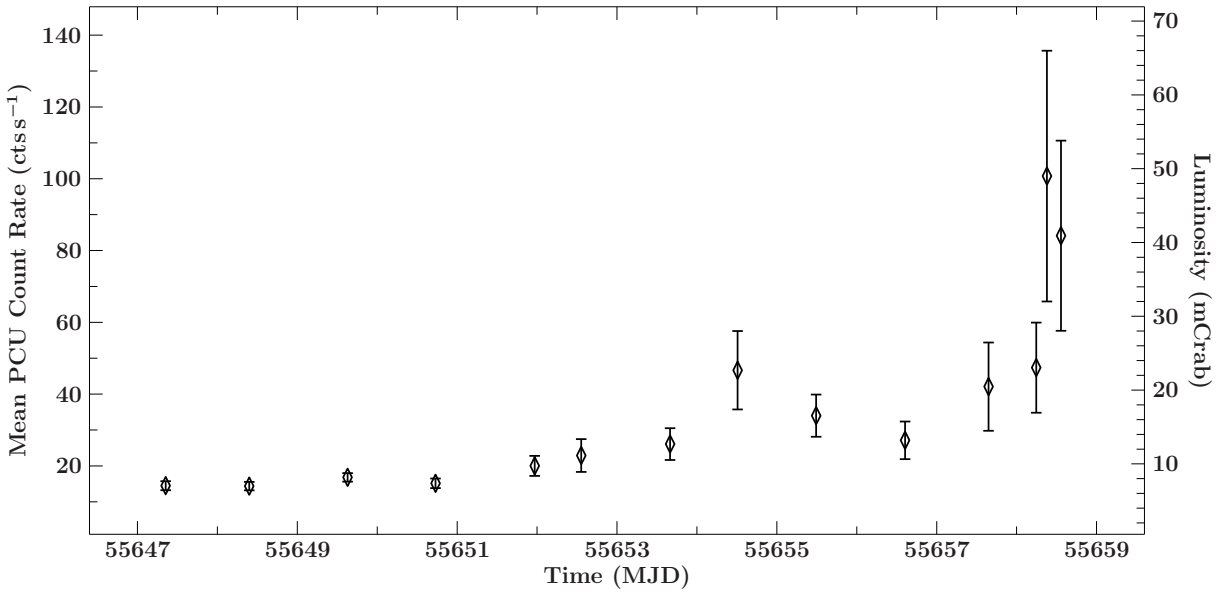

Figure 5.1: Mean PCU count rate of GRO J1008–57 starting two weeks before the predicted date of maximum luminosity of April 9. Including a short flare, the luminosity increased dramatically on April 7, indicating a new outburst.

Acknowledgments

I am grateful for the manifold support I experienced in the last year:

First of all, I would like to thank Jörn Wilms for the opportunity to write my Master's thesis in his group at the Dr. Karl Remeis-observatory. Thanks to his support and help during the last year I learned quite a lot about X-ray binaries and he encouraged my interest in working in this research field. Furthermore, I am thankful for off-topic conversations during coffee breaks, which mixed up the working atmosphere a lot. He is also always concerned about the mood of his *Schäfchen*, which, in my opinion, is the basement of a healthy working environment.

Thanks to Markus Kuster, who introduced me into X-ray binaries in the first place. Our meeting some years ago, where he have drawn a Roche lobe overflow on a paper, started a series of reactions, which finally leaded me to Bamberg.

I would like to thank Ingo Kreykenbohm, Katja Pottschmidt and the "Magnet" collaboration for their scientific knowledge and discussions. Moreover, I am grateful to Sebastian Müller and Felix Fürst for their support in understanding neutron star binaries. With the help of Moritz Böck, Thomas Dauser and, especially, Manfred Hanke I learned a lot about *ISIS* and how to do some nice plots. By now, I'm afraid to transform into Manfred$^{\text{nd}}$ about my repertoire on *ISIS* tricks and how to speed up code.

For instructions on correct scientific and TEXnical writing, I have to thank Jörn Wilms, Katja Pottschmidt and Manfred Hanke. Without the proofreading of Kerstin Bissinger, Victoria Grinberg and Manfred Hanke, this thesis would not be finished yet.

My colleagues at the Remeis-observatory are not only coworkers, but rather have become friends. I am really grateful for the joint adventures and the frequent social events. Furthermore, the observing nights in the domes and insane activities like the Messier marathon were instructive and a lot of fun.

A special part of my everyday life are the guys of the "Knigge room". Without their *support* life would be much harder and even more boring. Additionally, I have to thank them for teaching me how to drink beer without bottle openers.

Without the dedication of Uli Katz and Regine Maerker, the change from the Technische Universität Darmstadt to the Friedrich-Alexander Universität Erlangen-Nürnberg would have been impossible.

The most important person in the last year was, and will ever be, my girlfriend Kerstin. Without her warmth, encouraging words and love, I would never have survived this year. I am very thankful for her accepting me having my own crazy way and moving to Bamberg. The distance is, at least, no handicap.

Last but not least I have to dearly thank my parents. Their unrestricted support made it possible for me to study my hobby.

Thank you!

Bibliography

Abt H.A., 1983, ARA&A 21, 343

Araya R.A., Harding A.K., 1999, Astrophys. J. 517, 334

Araya-Góchez R.A., Harding A.K., 2000, Astrophys. J. 544, 1067

Barnstedt J., Staubert R., Santangelo A., et al., 2008, Astron. Astrophys. 486, 293

Becker P.A., Wolff M.T., 2005, Astrophys. J. 630, 465

Becker P.A., Wolff M.T., 2007, Astrophys. J. 654, 435

Bildsten L., Chakrabarty D., Chiu J., et al., 1997, ApJS 113, 367

Blum S., Kraus U., 2000, Astrophys. J. 529, 968

Boerner G., Hayakawa S., Nagase F., Anzer U., 1987, Astron. Astrophys. 182, 63

Bombaci I., 1996, Astron. Astrophys. 305, 871

Bondi H., Hoyle F., 1944, MNRAS 104, 273

Caballero I., Kretschmar P., Santangelo A., et al., 2007 465, L21

Camero-Arranz A., Finger M.H., Wilson-Hodge C.A., et al., 2010, In: Astrophysics of Neutron Stars 2010. American Institute of Physics Conference Series, in prep.

Chandrasekhar S., 1931, Astrophys. J. 74, 81

Coe M.J., Bird A.J., Hill A.B., et al., 2007, Mon. Not. R. Astron. Soc. 378, 1427

Coe M.J., Roche P., Everall C., et al., 1994, Mon. Not. R. Astron. Soc. 270, L57

DeCesar M.E., Boyd P.T., Markwardt C.B., et al., 2009, In: American Astronomical Society, Vol. 41. Bulletin of the American Astronomical Society, p. 299

Deeter J.E., Boynton P.E., Pravdo S.H., 1981, Astrophys. J. 247, 1003

Fewell M.P., 1995, American Journal of Physics 63, 653

Frank J., King A., Raine D., 1992, Accretion Power in Astrophysics, Cambridge University Press, Cambridge, United Kingdom

Gerthsen C., Vogel H., 1993, Physik, Springer-Verlag, Berlin, Heidelberg, New York

Ghosh P., Lamb F.K., 1979a, Astrophys. J. 232, 259

Ghosh P., Lamb F.K., 1979b, Astrophys. J. 234, 296

Ghosh P., Pethick C.J., Lamb F.K., 1977, Astrophys. J. 217, 578

Giacconi R., Gursky H., Paolini F.R., Rossi B.B., 1962, Phys. Rev. Lett. 9, 439

Grove J.E., Kurfess J.D., Phlips B.F., et al., 1995, In: International Cosmic Ray Conference, Vol. 2.

Grupen C., 1993, Teilchendetektoren, Biblographisches Institut & F.A. Brockhaus AG, Mannheim, Germany

Heindl W.A., Coburn W., Gruber D.E., et al., 1999, Astrophys. J. 521, L49

Herold H., 1979, Phys. Rev. D 19, 2868

Hilditch R.W., 2001, An Introduction to Close Binary Stars, Cambridge University Press, Cambridge, United Kingdom

Horner W.G., 1819, A new method of solving numerical equations of all orders, by continuous approximation. In: Philosophical Transactions of the Royal Society of London., p.308

Houck J.C., Denicola L.A., 2000, In: Manset N., Veillet C., Crabtree D. (eds.) Astronomical Data Analysis Software and Systems IX, Vol. 216. Astronomical Society of the Pacific Conference Series, p. 591

Jahoda K., Swank J.H., Giles A.B., et al., 1996, In: Siegmund O.H., Gummin M.A. (eds.) Society of Photo-Optical Instrumentation Engineers (SPIE) Conference Series, Vol. 2808., p.59

Janka H., Langanke K., Marek A., et al., 2007, Phys. Rep. 442, 38

Karzas W.J., Latter R., 1961, ApJS 6, 167

Kelley R., Rappaport S., Petre R., 1980, Astrophys. J. 238, 699

Kellogg E., Baldwin J.R., Koch D., 1975, Astrophys. J. 199, 299

Kippenhahn R., Weigert A., 1990, Stellar Structure and Evolution, Springer-Verlag, Berlin Heidelberg, Germany

Kretschmar P., 1996, Ph.D. thesis, Eberhard-Karls-Universität Tübingen

Kreykenbohm I., 2004, Ph.D. thesis, Eberhard-Karls-Universität Tübingen

Kühnel M., Müller S., Pottschmidt K., et al., 2010, The Astronomer's Telegram 3087
Kuster M., 2004, Ph.D. thesis, Eberhard-Karls-Universität Tübingen
Latal H.G., 1986, Astrophys. J. 309, 372
Leahy D.A., 1987, Astron. Astrophys. 180, 275
Leahy D.A., Darbro W., Elsner R.F., et al., 1983, Astrophys. J. 266, 160
Levine A.M., Bradt H., Cui W., et al., 1996, Astrophys. J., Lett. 469, L33
Levine A.M., Corbet R., 2006, The Astronomer's Telegram 940
Manchester R.N., Taylor J.H., 1977, Pulsars, W. H. Freeman & Co Ltd, San Francisco, CA (USA)
Mihara T., 1995, Ph.D. thesis, Univ. of Tokyo
Mikkola S., 1987, Celestial Mechanics 40, 329
Müller S., Kühnel M., Pottschmidt K., et al., 2010, The Astronomer's Telegram 3077
Müller S., Obst M., Kreykenbohm I., et al., 2010, In: Proceedings of Science., submitted
Nagase F., 1989, Publ. Astron. Soc. Jpn. 41, 1
Nagel W., 1981, Astrophys. J. 251, 288
Nowak M.A., 2004, In: P. Kaaret, F. K. Lamb .J.H.S. (ed.) X-ray Timing 2003: Rossi and Beyond, Vol. 714. American Institute of Physics Conference Series, p.89
Rothschild R.E., Blanco P.R., Gruber D.E., et al., 1998, Astrophys. J. 496, 538
Santangelo A., Segreto A., Giarrusso S., et al., 1999, Astrophys. J. 523, L85
Schandl S., Meyer F., 1994, Astron. Astrophys. 289, 149
Schönherr G., 2007, Ph.D. thesis, Eberhard-Karls-Universität Tübingen
Schönherr G., Wilms J., Kretschmar P., et al., 2007, Astron. Astrophys. 472, 353
Schwarm F., 2010, *Master's thesis*, Friederich-Alexander Universität Erlangen-Nürnberg
Schwarzenberg-Czerny A., 1989, MNRAS 241, 153
Shrader C.R., Sutaria F.K., Singh K.P., Macomb D.J., 1999, Astrophys. J. 512, 920
Srinivasan G., 2002 11, 67
Staubert R., Klochkov D., Wilms J., 2009, Astron. Astrophys. 500, 883
Stelzer B., 1997, *Master's thesis*, Eberhard-Karls-Universität Tübingen
Stollberg M.T., Finger M.H., Wilson R.B., et al., 1993, IAU Circ. 5836
Strobel K., Weigel M.K., 2001, Astron. Astrophys. 367, 582
Thielemann F.K., Hirschi R., Liebendörfer M., Diehl R., 2011, Astronomy with Radioactivities, Vol. 812 of *Lecture Notes in Physics*, Lecture Notes in Physics, Springer-Verlag, Heidelberg, Germany
Urpin V., Geppert U., 1995, MNRAS 275, 1117
van Allen J.A., 1958, Radiation belts around the earth, Freeman, San Francisco
van Allen J.A., McIlwain C.E., Ludwig G.H., 1959, J. Geophys. Res. 64, 271
Verbunt F., van den Heuvel E.P.J., 1995, In: Lewin W.H.G., van Paradijs J., van den Heuvel E.P.J. (eds.) X-ray binaries., p.457
Verner D.A., Verner E.M., Ferland G.J., 1996, Atomic Data and Nuclear Data Tables 64, 1
Willmore A.P., Bertram D., Watt M.P., et al., 1992, MNRAS 258, 621
Wilms J., 1998, Ph.D. thesis, Eberhard-Karls-Universität Tübingen
Wilms J., Allen A., McCray R., 2000, Astrophys. J. 542, 914
Wilson C.A., Finger M.H., Coe M.J., Negueruela I., 2003, Astrophys. J. 584, 996
Wilson J.R., 1985, In: Centrella J.M., Leblanc J.M., L. B.R. (eds.) Numerical Astrophysics., Boston, p. 422
Wilson R.B., Harmon B.A., Fishman G.J., et al., 1994, In: Holt S., Day C.S. (eds.) The Evolution of X-ray Binaries, Vol. 308. American Institute of Physics Conference Series, p. 451
Yahel R.Z., 1979, Astrophys. J. 229, L73
Zel'dovich Y.B., Guseynov O.H., 1966, Astrophys. J. 144, 840

Appendix A
Pulse Arrival Time

The following calculations are inspired by Hilditch (2001), Chapter 3.3, and lead to the description of the emitting time $t_{\mathrm{emit}}(n)$ of the n^{th} pulse in the barycenter of the binary.

Starting from a reference pulse at t_0 with a specific pulse phase ϕ_0, the pulse phase $\phi(t)$ at any time can be expanded into a Taylor series:

$$\phi(t) = \phi_0 + f(t-t_0) + \frac{1}{2}\dot{f}(t-t_0)^2 + \frac{1}{6}\ddot{f}(t-t_0)^3 + \frac{1}{24}\dddot{f}(t-t_0)^4 + \mathcal{O}(t^5) \tag{A.1}$$

The Taylor coefficients are the derivatives of the pulse frequency f. Equally the pulse emitting time $t_{\mathrm{emit}}(n)$ of pulse number n can be expanded, assuming $n = 0$ at $t = t_0$:

$$t_{\mathrm{emit}}(n) = t_0 + \left.\frac{\partial t}{\partial n}\right|_{n=0} \cdot n + \frac{1}{2}\left.\frac{\partial^2 t}{\partial n^2}\right|_{n=0} \cdot n^2 + \frac{1}{6}\left.\frac{\partial^3 t}{\partial n^3}\right|_{n=0} \cdot n^3 + \frac{1}{24}\left.\frac{\partial^4 t}{\partial n^4}\right|_{n=0} \cdot n^4 + \mathcal{O}(n^5) \tag{A.2}$$

Since the pulse number n is a proper subset of the pulse phase ϕ, the partial differential of n can be found by using equation A.1:

$$\partial n = \partial\phi = \left(f + \dot{f}(t-t_0) + \frac{1}{2}\ddot{f}(t-t_0)^2 + \frac{1}{6}\dddot{f}(t-t_0)^3\right)\partial t \tag{A.3}$$

Here terms of fifth order in t or higher are neglected. By using this substitution the derivatives of equation A.2 can be calculated:

$$\left.\frac{\partial t}{\partial n}\right|_{n=0} = \left.\frac{\partial t}{\partial t} \cdot \frac{1}{f + \dot{f}(t-t_0) + \frac{1}{2}\ddot{f}(t-t_0)^2 + \frac{1}{6}\dddot{f}(t-t_0)^3}\right|_{t=t_0} = \frac{1}{f} \tag{A.4}$$

$$\left.\frac{\partial^2 t}{\partial n^2}\right|_{n=0} = -\frac{\dot{f}}{f^3} \tag{A.5}$$

$$\left.\frac{\partial^3 t}{\partial n^3}\right|_{n=0} = \frac{3\dot{f}^2 - f\ddot{f}}{f^5} \tag{A.6}$$

$$\left.\frac{\partial^4 t}{\partial n^4}\right|_{n=0} = -\frac{15\dot{f}^3 - 10f\dot{f}\ddot{f} + f^2\dddot{f}}{f^7} \tag{A.7}$$

Expressing the pulse frequency f by the pulse period $P = \frac{1}{f}$ leads to the final result:

$$t_{\mathrm{emit}}(n) = t_0 + Pn + \frac{1}{2}P\dot{P}n^2 + \frac{1}{6}(P^2\ddot{P} + P\dot{P}^2)n^3 + \frac{1}{24}(P^3\dddot{P} + 4P^2\dot{P}\ddot{P} + \dot{P}^3P)n^4 \tag{A.8}$$

Appendix B
Cyclotron Line Sources

Table B.1: The following neutron star X-ray binaries show cyclotron resonant scattering features[1]

Source	Class	$E_{cyc}(keV)$
Swift J1626.6−5156	transient	10
4U 0115+634	transient	14, 24, 36, 48, 62
4U 1907+09	HMXB	18, 38
4U 1538−52	HMXB	22, 47
Vela X−1	HMXB	24, 52
V 0332+53	transient	27, 51, 74
Cep X−4	transient	28
Cen X-3	HMXB	29
X Per	HMXB	29
MXB 0656−072	transient	33
XTE J1946+274	transient	36
4U 1626−67	LMXB	37
GX 301−2	HMXB	37
Her X−1	LMXB	41
A0535+26	transient	45, 100+
1A1118−61	transient	55, 110?
GRO J1008−57	transient	88?

[1]For an actual list and references see
http://www.sternwarte.uni-erlangen.de/wiki/doku.php?id=cyclo:start

Appendix C

Observations

Table C.1: Used observations of GRO J1008–57. The numbering scheme #Y.n consists of the outburst (Y=5 for 2005 and Y=7 for 2007) and the number of the observation in the time-ordered sequence.

#	Satellite	Observation	Starttime (MJD)	Exposure (s)
5.1	*RXTE*	90089-03-01-00	53421.561	832
5.2	*RXTE*	90089-03-02-01	53426.006	2208
5.3	*RXTE*	90089-03-02-08	53426.286	864
5.4	*RXTE*	90089-03-02-07	53426.403	1232
5.5	*RXTE*	90089-03-02-02	53427.113	2912
5.6	*RXTE*	90089-03-02-000	53427.287	11936
5.7	*RXTE*	90089-03-02-000	53427.455	1664
5.8	*RXTE*	90089-03-02-000	53427.476	1792
5.9	*RXTE*	90089-03-02-00	53427.591	7792
5.10	*RXTE*	90089-03-02-03	53428.109	1808
5.11	*RXTE*	90089-03-02-04	53428.266	3104
5.12	*RXTE*	90089-03-02-04	53428.326	2720
5.13	*RXTE*	90089-03-02-05	53428.843	736
5.14	*RXTE*	90089-03-02-06	53429.282	9520
5.15	*RXTE*	90089-03-02-09	53430.349	2320
5.16	*RXTE*	90089-03-02-09	53430.415	2448
5.17	*RXTE*	90089-03-02-09	53430.481	2768
5.18	*RXTE*	90089-03-02-10	53431.145	1376
5.19	*RXTE*	90089-03-02-12	53431.203	2896
5.20	*RXTE*	90089-03-02-14	53431.559	1248
5.21	*RXTE*	90089-03-02-11	53431.663	1360
5.22	*RXTE*	90089-03-02-15	53431.728	624
5.23	*RXTE*	90089-03-02-16	53432.122	1616
5.24	*RXTE*	90089-03-02-13	53432.188	960
7.1	*RXTE*	93032-03-01-00	54426.002	560
7.2	*Swift*	00031030001	54427.692	2897
7.3	*RXTE*	93032-03-02-00	54427.808	2832
7.4	*RXTE*	93032-03-02-01	54429.840	2016
7.5	*RXTE*	93032-03-02-02	54431.607	2592
7.6	*RXTE*	93032-03-02-03	54433.060	1408
7.7	*RXTE*	93032-03-03-00	54434.237	1520
7.8	*Suzaku*	902003010	54434.482	47781
7.9	*RXTE*	93032-03-03-01	54435.503	864
7.10	*RXTE*	93032-03-03-02	54437.141	560
7.11	*RXTE*	93032-03-03-03	54438.173	768
7.12	*RXTE*	93032-03-03-04	54439.918	1760
7.13	*RXTE*	93032-03-04-01	54442.121	832
7.14	*RXTE*	93032-03-04-02	54443.103	592
7.15	*RXTE*	93032-03-04-00	54443.793	928
7.16	*RXTE*	93032-03-04-04	54445.234	1200
7.17	*RXTE*	93032-03-04-03	54446.335	1184
7.18	*RXTE*	93032-03-04-06	54447.017	1360